

2016-07-15

Investigation of Bond, Microstructure and Post-Fire Behavior of GFRP Reinforcement for Concrete

Omid Gooranorimi

University of Miami, omid.gooran@gmail.com

Follow this and additional works at: https://scholarlyrepository.miami.edu/oa_dissertations

Recommended Citation

Gooranorimi, Omid, "Investigation of Bond, Microstructure and Post-Fire Behavior of GFRP Reinforcement for Concrete" (2016). *Open Access Dissertations*. 1693.
https://scholarlyrepository.miami.edu/oa_dissertations/1693

This Open access is brought to you for free and open access by the Electronic Theses and Dissertations at Scholarly Repository. It has been accepted for inclusion in Open Access Dissertations by an authorized administrator of Scholarly Repository. For more information, please contact repository.library@miami.edu.

UNIVERSITY OF MIAMI

INVESTIGATION OF BOND, MICROSTRUCTURE AND POST-FIRE BEHAVIOR
OF GFRP REINFORCEMENT FOR CONCRETE

By

Omid Gooranorimi

A DISSERTATION

Submitted to the Faculty
of the University of Miami
in partial fulfillment of the requirements for
the degree of Doctor of Philosophy

Coral Gables, Florida

August 2016

©2016
Omid Gooranorimi
All Rights Reserved

UNIVERSITY OF MIAMI

A dissertation submitted in partial fulfillment of
the requirements for the degree of
Doctor of Philosophy

INVESTIGATION OF BOND, MICROSTRUCTURE AND POST-FIRE BEHAVIOR
OF GFRP REINFORCEMENT FOR CONCRETE

Omid Gooranorimi

Approved:

Wimal Suaris, Ph.D.
Associate Professor of Civil, Architectural,
and Environmental Engineering

Antonio Nanni, Ph.D.
Professor and Chair
of Civil, Architectural,
and Environmental Engineering

Francisco J. De Caso y Basalo, Ph.D.
Research Assistant Professor of Civil,
Architectural and Environmental
Engineering

Guillermo Prado, Ph.D.
Dean of the Graduate School

Stefano Mariani, Ph.D.
Associate Professor of Civil and
Environmental Engineering,
Politecnico di Milano, Italy

OMID GOORANORIMI

(Ph.D., Civil Engineering)

Investigation of Bond, Microstructure and Post-Fire Behavior of GFRP Reinforcement for Concrete (August 2016)

Abstract of a dissertation at the University of Miami.

Dissertation supervised by Professor Wimal Suaris.

No. of pages in text. (110)

Fiber reinforced polymer (FRP) composite materials are emerging as promising alternatives for traditional steel reinforcement in concrete structures. There is an increasing use of glass FRP (GFRP) bars as shear and flexural reinforcements in reinforced concrete (RC) elements especially in applications where corrosion resistance properties are required such as bridge decks and structures in coastal regions. GFRP offers additional advantages such as light weight, electromagnetic transparency, and ease of demolishing in temporary applications. Over the past twenty years, GFRP bars have been proved to be an effective solution for the dramatic and economically devastating corrosion problem of black steel reinforcements providing more durable structures with higher service life and reduced maintenance costs. Several aspects of GFRP behavior are still under investigation to enhance its acceptance in the construction industry. This dissertation focuses on bond properties, microstructure and post-fire behavior of GFRP bars.

First, the bond behavior of three GFRP bars with different surface characteristics was investigated by performing pull-out tests. The GFRP surface enhancement and embedment length were critical in determining the bond-slip relationship and final failure mode. GFRP bars with highly deformed surfaces failed by concrete cracking/splitting due to the high load transfer to concrete while GFRP bars with smoother surface exhibited the pull-through

mode of failure. Increasing the embedment length resulted in lower average bond strength due to the generation of non-uniform bond stresses. A parametric bond-slip relationship was proposed for the GFRP bar with sand coated and helically wrapped fiber that presented the pull-through mode of failure in pull-out test. The parameters were found by performing sensitivity analysis. The proposed bond-slip law was employed in an FEM model which was capable of predicting the failure mode and investigating the bond action along the embedment length. Additionally, the model was employed in a GFRP-RC slab to replace the common unrealistic perfect bond assumption in analytical solutions and led to more accurate results compared to experimental data.

In the second part of this dissertation, the microstructural patterns of four different GFRP bar were investigated using SEM analysis. Microstructural characteristics are crucial parameters in understanding and predicting GFRP behavior under different environments and states of stress. As a result of different production methods and constituents by manufacturers, each pristine bar presents different microstructure patterns including voids, defects, and fiber distribution. Considering the lack of GFRP microstructure knowledge, SEM imaging was performed on cross-sections of four different commercially available pristine GFRP bars with a nominal diameter of 12.7 mm (0.5 in.). Imaging was conducted at both low and high magnification levels and captured the i) existing defect/void patterns in the matrix; ii) fiber-matrix interface, and iii) fiber distribution in the matrix. Each bar demonstrated a unique defect/void pattern characterized by a combination of disconnected and continuous defect/voids at different locations of the cross-section. In addition, panorama images of the entire cross-section were provided to give a proper comparison between different bar types. These results can be used as a

benchmark for the microstructure of commercially available pristine GFRP bars and serve as a base for monitoring possible changes after any conditioning or testing. In order to investigate the effect of microstructure on GFRP durability, two of the bars were exposed to accelerated conditioning in an alkaline solution at 60 °C (140 °F) for 1000 hours. The horizontal shear test was performed and the results were compared with the pristine bars. The difference in microstructural patterns was found to significantly contribute to GFRP durability-related properties. SEM imaging and energy dispersive X-ray spectroscopy (EDS) analysis were performed on conditioned bars to provide additional data.

Finally in this dissertation, the post-fire behavior of two different GFRP bars with different surface characteristics was investigated. GFRP-RC slabs reinforced with two different GFRP bars were exposed to traditional standard furnace fire tests while being loaded at the service load in three-point bending configuration. After the cooling phase, the GFRP bars were extracted for investigation of their residual mechanical properties. Transverse and horizontal shear tests, transition glass temperature (T_g) and microstructural investigation using scanning electron microscopy (SEM) analysis were performed and the results were compared to the pristine bars. GFRP bars maintained the mechanical properties after two hours of exposure to a standard furnace fire. Additionally, a thermomechanical finite element model (FEM) was developed. First, the temperature distribution at different locations of the slab was determined. Next, the effect of the fire on the structural response and concrete cracking was demonstrated.

*To my parents and to the
Memory of my grandfather*

Acknowledgements

I am extremely thankful to my advisor Dr. Suaris for his support and kindness during my study in University of Miami. I also deeply thank Dr. Nanni, for his inspiring and motivating approach. I was honored to be a student of Dr. Suaris and Dr. Nanni and learn not only from their vast knowledge but also from their life experiences. I am in debt to both of them till the end of my life.

I also thank Dr. De Caso and Dr. Mariani for their help and guidance during this research.

I gratefully acknowledge the National Science Foundation (NSF) for the support provided to the Industry/University Center for Integration of Composites into Infrastructure (CICI) at the University of Miami under grant IIP-1439543 and its industrial members.

A very special thank goes to my girlfriend and best friend, Sima, with whom my journey at University of Miami was full of love and adventure.

I am greatly thankful to Dr. Claire for being not only my teammate in most of the projects but also being like a brother to me. I also thank my friends and CAE team members: Vanessa, Zahra, Dr. Arboleda, Keith and Phil for their supports and help.

Finally, my deepest appreciation and acknowledgement goes to my amazing parents, my mother for her love, my father for his passion for education, my brothers, Aref and Amirhosein for their supports, my uncle Mehdi, for his mentorship and to my late grandfather for his big dreams.

Table of Contents

Table of Contents	v
List of Figures	vii
List of Tables	xi
List of Abbreviations	xii
Chapter 1-Introduction	1
Scope of Research.....	3
GFRP Bars	4
Research Significance.....	5
Chapter 2-Bond of GFRP Bar to Concrete	7
Experimental Investigation of Bond	10
Pull out Test Results and Discussions	14
GFRP-H	14
GFRP-C.....	16
GFRP-A	19
Concrete Modeling.....	22
Concrete Damage Model	28
FEM Model.....	29
Concrete to GFRP Bond Modeling.....	30
Parametric Bond-slip Law	31
Results of FEM Analysis	32
FEM Analysis of GFRP-RC Slab	39
Perfect Bond.....	42
Incorporating the Bond-Slip Model	46
Bond Coefficient (k_b)	50
Concluding Outcomes.....	51
Future Research	53
Chapter 3-GFRP Microstructural Investigation	54
GFRP Samples	55
Sample Preparation	55
SEM Imaging	57
Results.....	57
Alkaline Conditioning.....	62

Concluding Remarks.....	69
Future Research	70
Chapter 4-GFRP Post-Fire Behavior.....	71
Important Factors in GFRP Fire Behavior.....	74
Specimen Configuration	75
Fire Exposure	76
Residual Mechanical Properties of the GFRP Bars	79
Transverse Shear Strength	79
Horizontal Shear Strength.....	80
Transition Glass Temperature (T_g).....	81
Microstructural Investigation.....	85
Thermomechanical FEM Model.....	88
Concrete Material Properties at Elevated Temperature	88
GFRP Material Properties at Elevated Temperature	92
Result of the Thermomechanical Analysis	94
Concluding Notes.....	98
Future Research	99
Chapter 5-Conclusions	100
Bond of GFRP Bar to Concrete	100
GFRP Microstructure.....	101
GFRP Post-Fire Behavior	102
Bibliography	104

List of Figures

Figure 1.1: GFRP bars in the deck of the Fate Bridge at the University of Miami's campus	5
Figure 1.2: Vibrating wire gauges installed at the deck of the Fate Bridge (a), zoomed view of the sensors used for the GFRP (b) and concrete (c)	6
Figure 1.3: Data acquisition stations installed permanently below the Fate (left) and the Innovation (right) Bridge	6
Figure 2.1: Schematic of samples, dimensions of GFRP bar for the long embedment configuration (Note: 1 in.=25.4 mm).....	11
Figure 2.2: A set of prepared samples for the pull-out test.....	12
Figure 2.3: Pull-out test set up	13
Figure 2.4: Concrete splitting (left) and peeling of the GFRP-H surface in samples with longer embedment length.....	15
Figure 2.5: Bond-slip data of GFRP-H samples with longer embedment length	15
Figure 2.6: Failure of GFRP-C samples due to separation of surface enhancement layer	17
Figure 2.7: Bond-slip results at the loaded end of GFRP-C with the short embedment length.....	18
Figure 2.8: Bond-slip results at the free end of GFRP-C with the short embedment length	18
Figure 2.9: Bond-slip results at the load end of GFRP-A with the long embedment length	20
Figure 2.10: Bond-slip results at the free end of GFRP-A with the long embedment length	20
Figure 2.11: Bond-slip results at the load end of GFRP-A with the short embedment length.....	21
Figure 2.12: Bond-slip results at the free end of GFRP-A with the short embedment length.....	21
Figure 2.13: The concrete behavior in compression implemented in Abaqus.....	24
Figure 2.14: Concrete behavior in tension.....	25
Figure 2.15: Concrete tensile strength vs. cracking strain adopted for different concrete mesh sizes	27
Figure 2.16: Tensile damage of concrete in softening region.....	28
Figure 2.17: The configuration of translator element	30
Figure 2.18: Proposed parametric bond-slip law	32
Figure 2.19: Sensitivity analysis on parameter D_1 ; pull-out load vs. slip at the free end compared to the experimental results	33
Figure 2.20: Sensitivity analysis on parameter α ; pull-out load vs. slip at free end compared to the experimental results	34

Figure 2.21: Final sensitivity analysis of parameter D_1 ; pull-out load vs. slip at the free end compared to the experimental results.....	35
Figure 2.22: Sensitivity analysis on parameter τ_1 ; Pull out load at free vs. slip at the free end compared to the experimental results.....	36
Figure 2.23: Translator elements defined at the interface.....	36
Figure 2.24: The overall force-displacement response at the free end and the response of the translators at different stages of the pull-out load.....	37
Figure 2.25: von Mises Stress (MPa) in GFRP bar and concrete	37
Figure 2.26: Cracks in the concrete due to the bond action.....	38
Figure 2.27: Splitting failure of concrete due to propagation of cracks through the entire cover.....	39
Figure 2.28: Force-displacement response of the translators at the final stage of the pull-out load for the sample with smaller concrete cover	39
Figure 2.29: Dimension of GFRP-RC slab (Note: 1 in=25.4 mm).....	40
Figure 2.30: Load-deflection results using different concrete mesh sizes and perfect bond	43
Figure 2.31: Cracks in concrete (plastic strain) in the model with the mesh size of 20 mm	43
Figure 2.32: Cracks in concrete (plastic strain) in the model with the mesh size of 15 mm	44
Figure 2.33: Cracks in concrete (plastic strain) in the model with the mesh size of 10 mm	44
Figure 2.34: Cracks in concrete (plastic strain) in the model with the mesh size of 7 mm	45
Figure 2.35: von Misses stress in the model with the concrete mesh size of 10 mm	46
Figure 2.36: Translator elements defined in the GFRP-RC slabs at the concrete interface	46
Figure 2.37: Load vs. mid-span deflection results of GFRP-RC slab using translator elements at the spacing of 75 mm.....	47
Figure 2.38: Load vs. mid-span deflection results of the GFRP-RC slabs using the translator elements with the spacing of 45 mm	48
Figure 2.39: Load-deflection at the mid–span of the GFRP-RC slab compared to experimental results	49
Figure 2.40: Concrete cracking in the model incorporating the bond-slip relationship ...	50
Figure 3.1: Final prepared GFRP samples (from left: GFRP-A, B, C, and D).....	56
Figure 3.2: A continuous defect at the edge of GFRP-A at magnification levels of 40x (left) and 110x (right).....	57
Figure 3.3: Distributed voids in the cross-section of GFRP-A: close to the edge (left), close to the center (right)	58

Figure 3.4: Connected void patterns at the edge (left) and at the center (right) of GFRP-B	58
Figure 3.5: Detailed view of a defect close to the edge of GFRP-B at magnification levels of 80x (left) and 230x (right)	59
Figure 3.6: High magnification image of a void (left) and area with no void (right) of GFRP-B.....	59
Figure 3.7: A defect at the edge of GFRP-C at magnification levels of 80x (left) and 150x (right)	60
Figure 3.8: Detailed view of a void in the center of GFRP-C at magnification levels of 55x (left) and 140 x (right).....	60
Figure 3.9: Area with no void of GFRP-C at magnification levels of 350x (left) and 1200x (right)	60
Figure 3.10: Disconnected void patterns at the edge (left) and at the center (right) of GFRP-D	61
Figure 3.11: Higher magnification image of the area with voids (left) & area with no void (right) of GFRP-D.....	61
Figure 3.12: Panorama images of GFRP-A (a), GFRP-B (b), GFRP-C (c), and GFRP-D (d).....	62
Figure 3.13: GFRP-B (left) and GFRP-C (right) samples used in the horizontal shear test	63
Figure 3.14: Horizontal shear test performed on GFRP bars.....	63
Figure 3.15: Conditioned and intact region in GFRP-C	65
Figure 3.16: A conditioned region of GFRP-B presenting an extensive damage in the resin and glass fibers.....	66
Figure 3.17: A conditioned region of GFRP-B presenting an extensive damage in the fibers at the vicinity of the existing defects	66
Figure 3.18: Result of the EDS analysis performed at the edge of GFRP-B after accelerated conditioning	67
Figure 3.19: Result of the EDS analysis performed on pristine GFRP-B bar	67
Figure 3.20: Elemental scatter of GFRP-B after exposure to alkaline solution: SEM image of GFRP-B (a) and elemental distributions of: Cl (b), Na (c), Si (d), Ca (e), Al (f), O (g), and Mg (k).....	68
Figure 4.1: Different stages of a real fire	71
Figure 4.2: Schematic temperature-time curves of the ASTM E119 standard and the real fire [58]	72
Figure 4.3: Schematic of GFRP-RC slabs (Note: 1 in.=25.4 mm)	76
Figure 4.4: GFRP-RC slabs facing the vertical furnace	77
Figure 4.5: Temperature-time profile of the furnace	78
Figure 4.6: Temperature gradient in a representative fire exposed GFRP-RC slab	78

Figure 4.7: Location of the extracted samples along the GFRP bar after fire exposure...	79
Figure 4.8: GFRP bars tested in transverse shear fixture.....	79
Figure 4.9: DMA test performed in 3-point bending configuration	82
Figure 4.10: Output of DMA test performed on a pristine GFRP-A sample.....	83
Figure 4.11: Output of DMA test performed on a fire-exposed GFRP-A sample.....	83
Figure 4.12: Output of DMA test performed on a pristine GFRP-C sample.....	84
Figure 4.13: Output of DMA test performed on a fire-exposed GFRP-C sample.....	84
Figure 4.14: GFRP samples prior to SEM imaging: GFRP-A (left) and GFRP-C (right)	85
Figure 4.15: SEM image of the GFRP-A after fire exposure at the magnification level of 200x.....	86
Figure 4.16: SEM image of GFRP-C after fire exposure at the magnification level of 140x.....	86
Figure 4.17: SEM image of the concrete to GFRP-A interface after fire exposure at the magnification level of 23x	87
Figure 4.18: SEM image of the concrete to GFRP-C interface after fire exposure at the magnification level of 20x	87
Figure 4.19: Change of the concrete strength with temperature during the fire exposure	89
Figure 4.20: Compression behavior of concrete at different temperature of °C.....	90
Figure 4.21: Tension behavior of concrete at different temperature of °C	90
Figure 4.22: Concrete conductivity variation with temperature	91
Figure 4.23: Concrete specific heat at different temperatures	92
Figure 4.24: GFRP normalized properties at different temperature	93
Figure 4.25: Change of GFRP conductivity with temperature	94
Figure 4.26: Temperature distribution in cross-section of GFRP-RC slab.....	95
Figure 4.27: Temperature distribution along the fire exposed slab	96
Figure 4.28: Cracking in the GFRP-RC slab due to applied load of 24 kN	96
Figure 4.29: Cracks in GFRP-RC slab after the fire exposure	97
Figure 4.30: Load-deflection result at mid-span of the GFRP-RC slab after fire exposure	97

List of Tables

Table 2.1: The characteristics of GFRP bars used in pull-out tests	11
Table 2.2: Results of pull-out tests performed on GFRP-H.....	16
Table 2.3: Results of pull-out tests performed on GFRP-C.....	19
Table 2.4: Results of pull-out tests performed on GFRP-A.....	22
Table 2.5: Base values of the fracture energy for different aggregate sizes	25
Table 2.6: Implemented parameters in the sensitivity analysis	33
Table 2.7: Different parameters implemented in sensitivity analysis.....	41
Table 3.1: GFRP nominal and measured cross-sectional areas	56
Table 3.2: Results of the horizontal shear test on pristine and conditioned GFRP samples	64
Table 4.1: Average results of the transverse shear tests on fire exposed GFRP bars	80
Table 4.2: Average results of the horizontal shear tests performed on the fire exposed GFRP bars	81
Table 4.3: Average T_g test results performed on fire exposed GFRP bars	82

List of Abbreviations

ACI	American Concrete Institute
ASTM	American Standards for Testing and Materials
BFRP	Basalt Fiber Reinforced Polymer
CICI	Center for the Integration of Composites into Infrastructure
COV	Coefficient of Variation
DMA	Dynamic Mechanical Analysis
EDS	Energy Dispersive X-ray Spectroscopy
FEM	Finite Element Method
FPZ	Fracture Process Zone
FRP	Fiber Reinforced Polymer
GFRP	Glass Fiber Reinforced Polymer
IAS	International Accreditation Service
ISO	International Organization for Standardization
I/UCRC	Industry/University Cooperative Research Center
LVDT	Linear Variable Differential Transducer
RC	Reinforced Concrete
SEM	Scanning Electron Microscopy
UM-SML	University of Miami - Structures and Materials Laboratory
US	United States

Chapter 1-Introduction

The deterioration of concrete structures due to corrosion of traditional black steel reinforcements has become major safety and economic concerns. Different solutions such as galvanized and epoxy coated steel have been tried to provide a protective layer for the black steel reinforcement. The coated layers could not solve the corrosion problem since any damage to the coating prior to placement compromised the corrosion protection. Replacing the steel reinforcement with glass fiber reinforced polymer (GFRP) composite bars has been proven to be the most efficient solution. GFRP bars were first commercialized in 1980's due to the need of electromagnetic transparent materials in construction [1]. The most important advantage of GFRP bars is the corrosion resistance property which makes them suitable in aggressive environments such as bridge decks. Additionally, being four times lighter than steel, GFRP reduces the labor cost of construction due to ease of handling and application. The GFRP bars' immediate cost is comparable with epoxy coated steel rebar while it reduces the long-term costs by increasing the service life of the structure. Different aspects of GFRP bars is still under further investigation to expand its application [1].

This dissertation is focused on investigating the behavior of GFRP bars and GFRP-RC structural elements through experimental studies and numerical modeling. Bond properties to concrete, microstructural patterns and post-fire behavior of GFRP bars were studied. First, bond properties of three different GFRP bars with different surface characteristics were investigated through the pull-out test. The effect of surface characteristics and embedment length on bond were investigated. A parametric bond-slip model was proposed

for the GFRP bar with sand coated surface. The parameters were found using finite element analysis (FEM). Finally, the model was employed in a FEM analysis to predict the structural response of a GFRP-RC member.

In the second part of this dissertation, microstructural patterns of four commercially available GFRP bars produced by different manufacturers were investigated using SEM imaging. Each bar presented a unique pattern of defects and voids. The effect of this pattern on GFRP durability was investigated by conditioning two bars which presented the most different microstructural patterns in alkaline solution at elevated temperature. The horizontal shear strength was determined as a proper sign of durability. Energy dispersive X-ray spectroscopy (EDS) was also performed to monitor the effect of conditioning and change of chemical composition at the vicinity of existing defects/voids.

In the final part of this study, the residual mechanical properties of two different GFRP bars with different surface characteristics extracted from GFRP-RC slabs exposed to standard furnace fire were investigated. Mechanical properties including transverse and inter-laminar shear strength, and transition glass temperature (T_g) were determined and the results were compared to the pristine bars. In addition, scanning electron microscopic (SEM) imaging was performed on GFRP bars and at the GFRP-concrete interface to monitor possible damage of the fibers and interfacial bond, respectively. A coupled thermomechanical FEM analysis was developed to monitor the temperature distribution and the effect of fire loading on concrete cracking and deflection of the RC member. By considering proper design parameters such as concrete cover, GFRP can maintain its mechanical properties for a sufficient time and can serve as suitable reinforcement in structures with a possible fire scenario.

Scope of Research

Different organizations such as American Concrete Institute (ACI) and ASTM International have provided documents, specifications, and guidelines for implementation of GFRP bars in construction such as ACI 440.1R, ACI 440. 3R, ACI 440.8, [2-4] and ASTM D7205 [5]. Additionally, ICC Evaluation Service (ICC-ES) has proposed acceptance criteria for GFRP bar as an internal reinforcement in concrete (AC 454) [6].

This study covers three aspects of GFRP behavior and leads to a better understanding of this material. The research was performed at the University of Miami-Structural and Material Laboratory (UM-SML), an accredited facility by the International Accreditation Service (IAS). Tests were performed in accordance with the ICC-ES and ISO 17027 standard (General requirements for the competence of testing and calibration laboratories).

The three studies in this dissertation start with a detail investigation of the bond-slip behavior of GFRP to concrete and developing a numerical bond-slip model to be implemented in the GFRP-RC structures.

The second study investigates the microstructural patterns of existing defects and voids in four commercially available GFRP bars produced by different manufacturers. Each bar presented a unique pattern of existing defects and voids as a signature of manufacturing process. The effect of these patterns on the durability of GFRP bars was investigated.

Finally, the third study covers the post-fire behavior of GFRP bars after exposure to standard fire tests as reinforcements in GFRP-RC slabs. The residual mechanical properties of GFRP bars were investigated. GFRP bars can be implemented in structures with possible fire scenarios by considering proper design parameters such as concrete cover to sufficiently protect the bars for a required time period.

GFRP Bars

The FRP bars are mainly made of carbon, glass, aramid or basalt fibers as load carrying constituents and the resin to protect the fibers and transfer and distribute the load among the fibers. Vinyl ester is the most commonly used resin with the glass fibers while thermosetting epoxies are usually used with carbon fibers [1]. GFRP is a balance of cost and strength in FRP family. The glass fibers are available in different types such as electrical (E-glass), high strength (S-glass) and electrical/chemical resistance (E-CR-glass) glass. E and E-CR are the most common types of glass in GFRP bars.

Different manufacturing process such as pultrusion and braiding are used to produce GFRP rebars. Pultrusion has recently become the most common process which also has the advantage of producing the irregular shape continuous cross-sections. In this method, first fibers go through a resin bath and impregnated with a liquid resin. Then, they pass through a die to shape to the desired size. In this stage, surface enhancements such as sand coating and fiber wrapping are added to the bars to provide an additional bond to concrete. Finally, the bar enters the oven to cure the resin [1].

GFRP bars demonstrate a linear elastic behavior till failure characterized by high tensile strength while the compression strength of GFRP bars is around 45% of their tensile strength. The tensile strength of GFRP bars varies with bar diameter [1]. Typically, the bars with larger diameter show a lower tensile strength due to shear lag effect. The strength and stiffness in the fiber direction are greatly affected by the fiber to resin volume ratio. Additional parameters such as the rate of resin polymerization, the manufacturing process, and the quality control also change the mechanical properties of GFRP bars.

Research Significance

The main objectives of this research are to provide a deeper understanding of GFRP behavior, enhance its implementation in the construction industry and ultimately to provide more durable and sustainable structures/infrastructures.

An immediate impact of this research has led to the implementation of GFRP reinforcements in two recently built pedestrian bridges at the University of Miami's campus. GFRP bars were used in the bridge deck of the Fate Bridge spanning on the Osceola Lake as shown in Figure 1.1 and also accompanied the basalt FRP (BFRP) bars and carbon FRP (CFRP) tendons in the Innovation Bridge at the University of Miami's campus.



Figure 1.1: GFRP bars in the deck of the Fate Bridge at the University of Miami's campus

In both bridges, vibrating wire gauges were used to monitor the strain (stress) in the concrete and FRP reinforcements (Figure 1.2) at certain time intervals after construction, using permanently installed data acquisition stations (Figure 1.3).

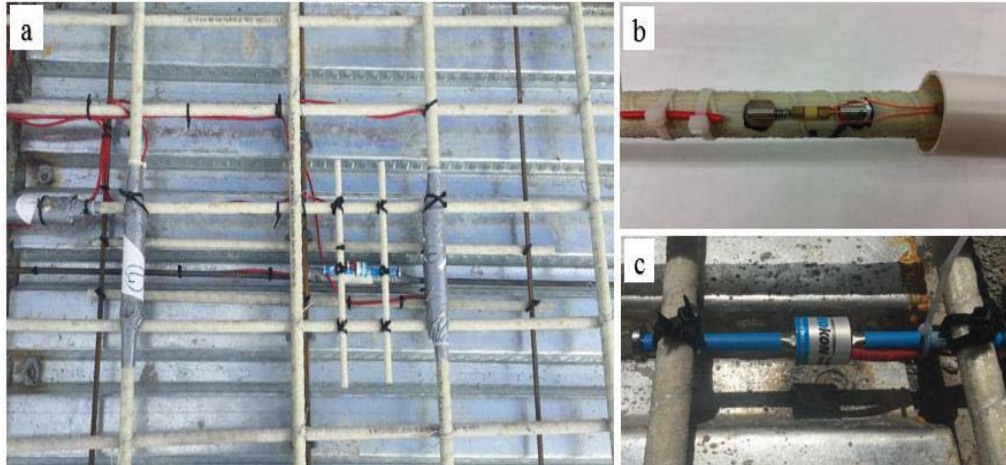


Figure 1.2: Vibrating wire gauges installed at the deck of the Fate Bridge (a), zoomed view of the sensors used for the GFRP (b) and concrete (c)



Figure 1.3: Data acquisition stations installed permanently below the Fate (left) and the Innovation (right) Bridge

This research contributes to the state-of-the-art knowledge of GFRP composite materials specifically leading to a deeper understanding of the bond properties to concrete, microstructural patterns and post-fire behavior.

Chapter 2-Bond of GFRP Bar to Concrete

Bond development is one of the most crucial aspects of GFRP structural response as the proper bond between concrete and reinforcement is essential to ensure the proper functioning of RC structures [7]. The mechanism of the bond transfer between internal FRP reinforcement and concrete has been investigated by several scholars [7-14]. GFRP bond mechanism is different from deformed steel rebars and is affected by more parameters [11] such as the bar type, surface profile, bar diameter, concrete strength, and embedment length [7]. It has been documented that larger bar diameters and embedment length lead to lower bond strength due to the generation of non-uniform bond stress [7].

In contrast to the deformed steel rebars, which have standardized ribbed surface profiles, each GFRP bar is produced with different surface characteristics such as fine or coarse sand coated, fiber wrapped and deformed ribbed surfaces (similar to steel rebars) to provide the bond to concrete. Additionally, the surface of the GFRP bar is weaker and softer than that of steel and may fracture/deform due to the bond action. The effect of the GFRP surface properties is addressed in this study by investigating bars with different surface characteristics.

Due to the complexity of the bond modeling, most of the scholars have considered a perfect bond between concrete and reinforcement while ignoring any possible slippage [15-18]. A slip mechanism accompanied with a concrete cracking model is required to provide a precise and realistic prediction of the load-deflection response and the final failure mode [19-21].

In the process of bond activation, first the initial contact between the concrete and reinforcement is maintained with the interlock between the reinforcement and the cementitious matrix. After the stress reaches a certain level, the initial bond breaks. The load transfer is maintained due to the bearing of the reinforcement surface against the concrete which causes the formation of cone-shaped cracks in the concrete starting at the reinforcement surface. This stage may lead to two different failure scenarios i) if the crack propagates through the entire concrete cover, concrete splitting failure happens which is accompanied by the sudden drop of the bond stress, and ii) when the concrete confinement is sufficient enough to prevent the splitting failure, the pull-through of the bar occurs and the load transferring mechanism changes to friction [22]. Since cracking plays a critical role in identifying the failure type, more investigations need to be conducted on the role of bond action in the crack initiation, propagation, and final failure [23].

Concrete cracking can be modeled using either the discrete or the smeared cracking model approaches. The discrete crack model treats the crack as a real discontinuity and was first proposed by Ngo and Scordelis [24]. They modeled the crack by separating the elements along the crack path. This model is useful to study the crack vicinity but it needs a high computational effort and also constraints the crack to follow a predefined path along the element edge. On the other hand, smeared crack modeling, proposed by Rashid [25] and extensively used by Hillerborg and coworkers [26] and Zimmermann [27] treats the cracked body as a continuum and captures the crack process through a constitutive relationship. Mesh sensitivity is the main problem of the smeared crack model. In this study, smeared crack modeling has been employed to investigate the crack initiation and propagation in concrete.

Several scholars tried to formulate the bond model for FRP reinforcement by modifying the bond formulation between steel and concrete by using new parameters [28-29]. Generally, analytical models are calibrated using experimental results [28] and curve fitting techniques. The same technique has been followed in this study.

The main purpose of the present study is to investigate the bond to concrete of three GFRP bars with different surface characteristics and to propose a bond-slip law validated by both experimental study and finite element modeling (FEM).

First, two sets of pull-out tests with different bonded lengths were performed on GFRP bars embedded in the concrete cylinders. The average bond-slip relationship was extracted using the experimental data and the failure mode was investigated for each bar type. Next, for sand coated GFRP bar, the experimental results were employed to propose a nodal parametric bond-slip law to be implemented in the FEM simulation. While one bar type and a specific diameter were selected for this study, the proposed methodology and numerical modeling approach may be extended to other GFRP bar types and diameters.

The FEM model was developed in Abaqus, which provides a proper implementation of crack modeling and material properties. The bond action between the concrete and reinforcement was explicitly modeled. A sensitivity analysis using FEM was performed to obtain the parameters of the bond-slip law. Different points along the embedment length of the GFRP bar were monitored by extracting the force-displacement data in order to investigate the bond behavior along the embedment length and to highlight the difference between nodal and average bond-slip relationships. Finally, simulations were performed on the samples with different concrete covers and the failure mode was predicted by monitoring the propagation of the cracks in the concrete cover. In the last part of this study,

the developed model was implemented in a GFRP-RC slab to accurately predict the load-deflection response. By incorporating the bond-slip model between the concrete and reinforcement, more accurate results were obtained compared to the model which assumed no slippage.




Experimental Investigation of Bond

In this study, the bond-slip laws of three different GFRP bars were investigated by performing pull-out tests. Each bar was characterized by different surface characteristics including a sand coated and helically wrapped fibers (GFRP-A), a ribbed surface GFRP bar similar to the steel rebar (GFRP-C) and a hollow core GFRP bar with a highly deformed surface (GFRP-H). Table 2.1 presents the mechanical properties, nominal and measured area of the bars. The nominal area is based on a circle with nominal diameter, while the average measured area was computed based on a work by Claire and coworkers [30] following a standard test method for density and specific gravity (relative density) of plastics by displacement, ASTM D792 [31].

Samples with two different bonded lengths of 203.2 mm (8 in.) and 63.5 mm (2.5 in.) were tested respectively referring to the long and short embedment lengths. For each set, five repetitions were performed.

The total length of each bar was 1524 mm (60 in.). A length of 101.6 mm (4 in.) of the bar from the side close to the loaded end was debonded using PVC tape for samples with long bonded length. A length of 241 mm (9.5 in.) was similarly debonded for samples with short embedment length. It prevented both the stress concentration and the application of a compression load on surrounding concrete. Figure 2.1 shows a schematic diagram of the pull-out samples, the characteristic dimensions of the bar and confining concrete.

Table 2.1: The characteristics of GFRP bars used in pull-out tests

Surface Texture	GFRP	Area (mm ²)		Modulus of Elasticity (GPa)	Ultimate Strain (%)	Poisson's Ratio
		Nominal	Measured			
Fine sand coated & helically wrapped fiber	A 	126.45	137.8	46.2	1.64	0.3
Ribbed surface	C 	126.45	130.5	42.0	2.00	0.3
Highly deformed surface	H 	126.45	176.77	51.3	2.18	0.3

Note: 1 mm² = 0.00155 in²; 1GPa= 145.037 ksi

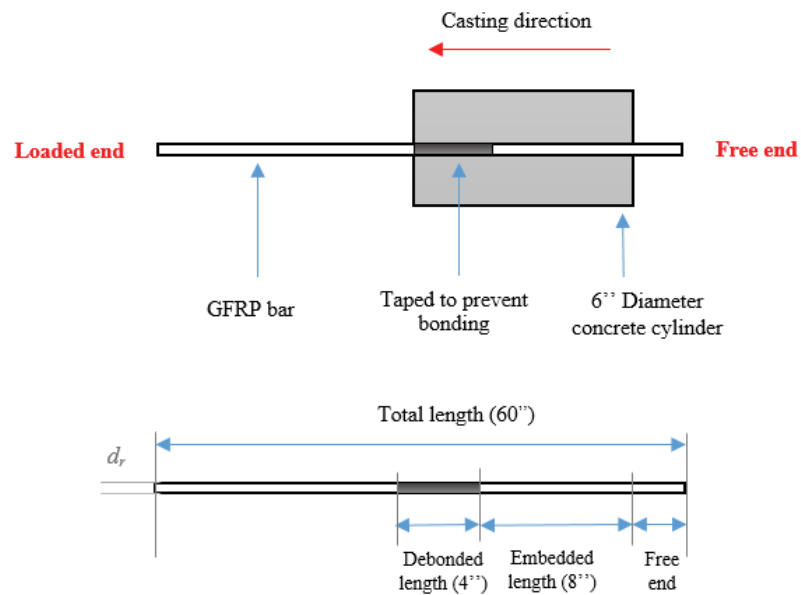


Figure 2.1: Schematic of samples, dimensions of GFRP bar for the long embedment configuration (Note: 1 in.=25.4 mm)

A steel tube filled with expansive grout was mounted at the loaded end of the bar for gripping purposes. Figure 2.2 presents a set of the prepared samples.



Figure 2.2: A set of prepared samples for the pull-out test

The tests were performed in the displacement control mode with a rate of 0.5 mm/min (0.02 in./min) using a Baldwin universal testing frame with a load capacity of 890 kN (200 Kips). Three linear variable displacement transducers (LVDT) were used to record the slip at the loaded and free ends of the bar as shown in Figure 2.3.

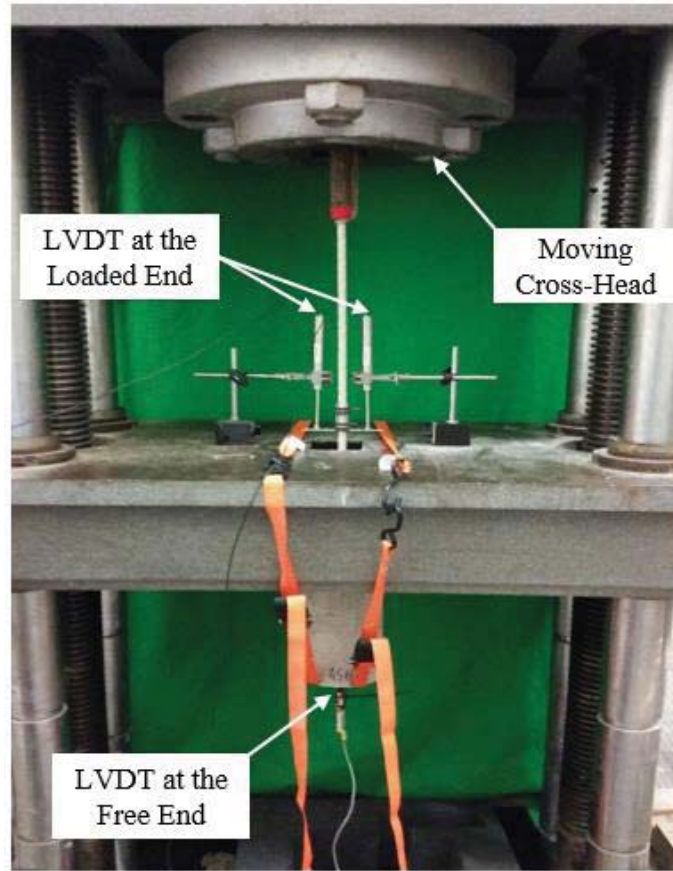


Figure 2.3: Pull out test set up

The average bond stress (τ_{ave}) was calculated using the pull-out load on the bar (F), embedment length (l), and diameter of the bar (d), as follows:

$$\tau_{ave} = \frac{F}{\pi dl} \quad (2.1)$$

Samples were named in the format of X-Y-Z, where X refers to the type of GFRP bar (A, C, and H), Y refers to the embedment length (L for 203.2 mm and S for 63.5 mm embedment length) and Z stands for the repetition of the test (1 to 5).

Due to the low elastic modulus of GFRP bars compared to steel rebars, the elongation at the loaded end needs to be corrected. The slip at the loaded end was adjusted by subtracting the elongation of the bar from the LVDT support point to the level of the bonded portion of the bar, from the measured displacement of the loaded end, given as:

$$D_{Loaded_end} = U_{Measured} - U_{Gl} = U_{Measured} - \frac{Fl_{Gl}}{EA} \quad (2.2)$$

where D_{Loaded_end} is the slip at the loaded end, $U_{Measured}$ is the measured displacement at the loaded end, U_{Gl} is the deformation of the bar, l_{Gl} is the length of the bar from the LVD support point to the level of the bonded portion, E is the modulus of the elasticity and A is the cross-sectional area of the bar.

Pull out Test Results and Discussions

GFRP-H

All the samples failed with splitting of the concrete. The highly ribbed surface profile caused this type of failure. It generated local diagonal cracks which propagated through the entire concrete cover.

In samples with longer embedment length, peeling off the bar surface was observed, as shown in Figure 2.4. The bond-slip data of GFRP-H samples with the longer embedment length is provided in Figure 2.5.

No considerable slippage was measured at the free end of the samples (less than 0.35 mm). The measuring instruments were severely damaged due to concrete splitting. The slippage of the free end of the bar was measured only for one bar and compared to the slippage of the loaded end. The measured slip at the loaded end was still different with the slip measured at the free end after subtracting the elastic deformation of the GFRP bars as mentioned in equation 2.2. The deformation of the rubber disk and steel plates which were used to distribute the load from testing frame to the loaded end of the concrete cylinders, significantly affected the measured slip at the loaded end of the GFRP. Table 2.2 shows the result of the tests performed on GFRP-H.



Figure 2.4: Concrete splitting (left) and peeling of the GFRP-H surface in samples with longer embedment length

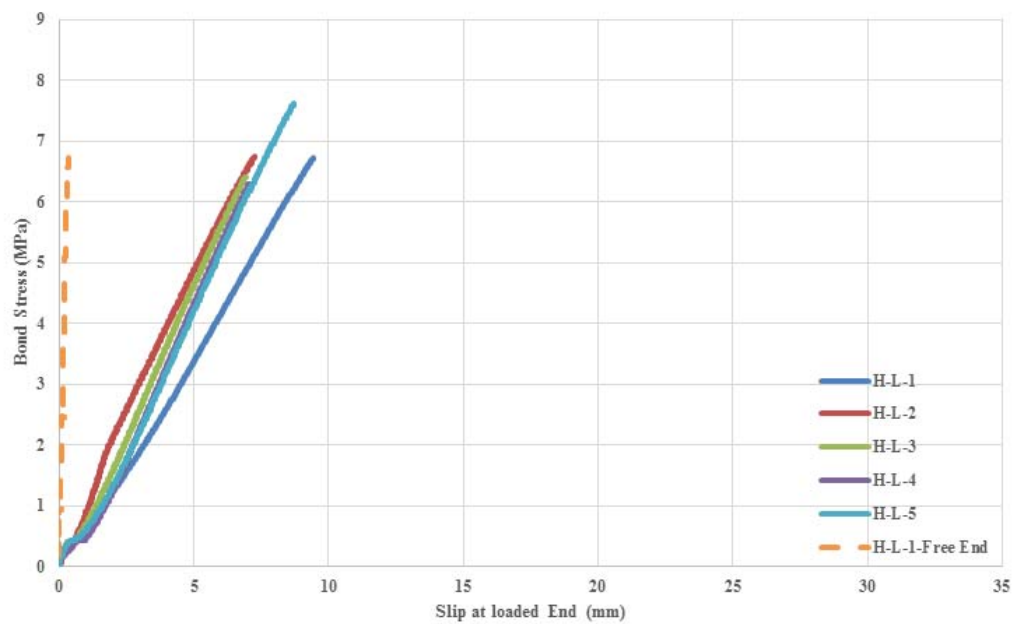


Figure 2.5: Bond-slip data of GFRP-H samples with longer embedment length

As shown in Table 2.2, the average bond stress increased by reducing the embedment length. This observation was expected due to the generation of non-uniform bond stress.

Table 2.2: Results of pull-out tests performed on GFRP-H

Sample ID	F_{\max} (kN)	τ_{ave}^{max} (MPa)	Bond Failure Mode
H-L-1	103.14	6.73	Concrete Splitting
H-L-2	103.36	6.74	
H-L-3	102.28	6.67	
H-L-4	96.55	6.30	
H-L-5	116.90	7.62	
Ave	104.44	6.81	
SD	6.71	0.44	
COV (%)	6.42	6.42	
H-S-1	89.64	18.71	Concrete Splitting
H-S-2	84.71	17.68	
H-S-3	64.99	13.56	
H-S-4	73.51	15.34	
H-S-5	73.06	15.25	
Ave	77.18	16.11	
SD	1.97	1.85	
COV (%)	11.46	11.46	

Note: 1kN= 0.2248 kips; 1 MPa= 0.145 ksi

GFRP-C

GFRP-C samples with the long bonded length presented the separation of the surface profile from the core of the bar due to the high level of the applied load. The generated shear stress exceeded the adhesion strength of the surface enhancement layer (Figure 2.6).

The test was stopped as soon as this phenomenon happened.



Figure 2.6: Failure of GFRP-C samples due to separation of surface enhancement layer

The bond-slip results of GFRP-C samples with the short embedment length are provided in Figures 2.7 and 2.8. The bond strength achieved at approximate slippage of 0.5 mm at the free end, next the slippage continued accompanied by drop of the load. All samples failed due to propagation of cracks through the entire concrete cover. The ribbed surface of the bar transferred a sufficient load to propagate the crack through the entire concrete cover. A considerable slippage happened at the free end of the bar since the surface of the bar was not highly deformed as GFRP-H,

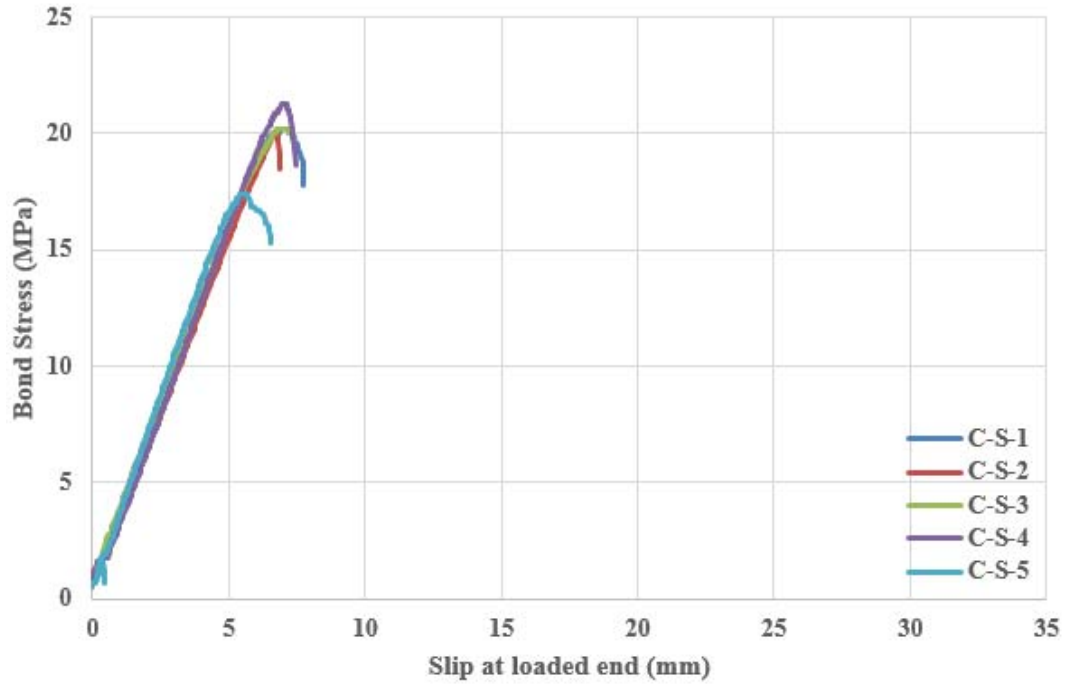


Figure 2.7: Bond-slip results at the loaded end of GFRP-C with the short embedment length

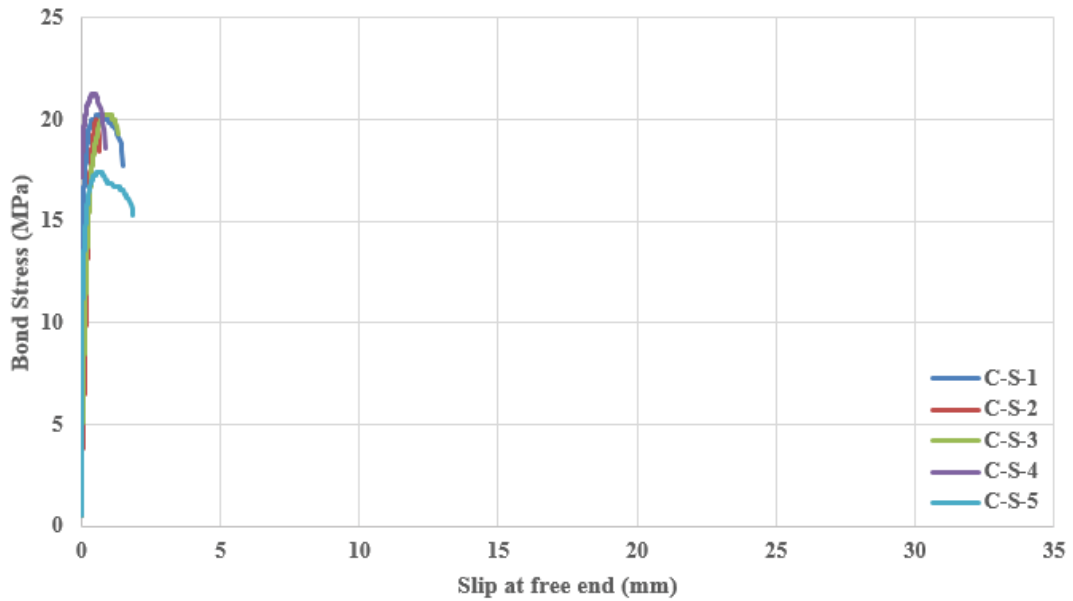


Figure 2.8: Bond-slip results at the free end of GFRP-C with the short embedment length

Table 2.3 shows the detailed result of the tests performed on GFRP-C.

Table 2.3: Results of pull-out tests performed on GFRP-C

Sample ID	F_{\max} (kN)	τ_{ave}^{max} (MPa)	Bond Failure Mode
C-L-1	75.48	9.24	Bar Surface Separation
C-L-2	79.92	9.78	
C-L-3	91.44	11.19	
C-L-4	100.40	12.29	
C-L-5	92.78	11.36	
Ave	88.00	10.77	
SD	9.06	1.11	
COV (%)	10.30	10.30	
C-S-1	51.55	20.19	Concrete Cracking
C-S-2	51.10	20.02	
C-S-3	51.55	20.19	
C-S-4	54.23	21.24	
C-S-5	44.37	17.3	
Ave	50.56	19.80	
SD	3.29	1.29	
COV (%)	6.5	6.5	

Note: 1kN= 0.2248 kips; 1 MPa= 0.145 ksi

GFRP-A

All GFRP-A samples failed in the pull-through mode of failure. The concrete cylinder provided adequate confinement that avoided the cracks to propagate through the entire concrete cover. In addition, sand coated and helically fiber wrapped surface of the bar did not transfer a high level of interlock that could lead to concrete splitting. The bond-slip results of the tests performed on all GFRP-A samples are shown in Figure 2.9-2.12.

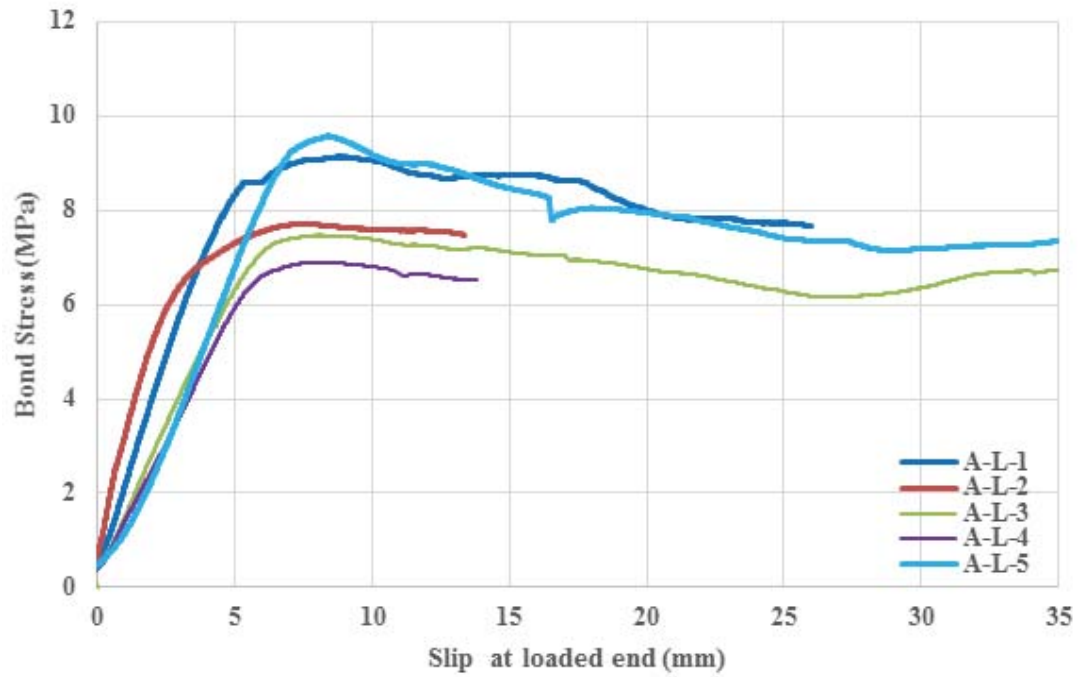


Figure 2.9: Bond-slip results at the load end of GFRP-A with the long embedment length

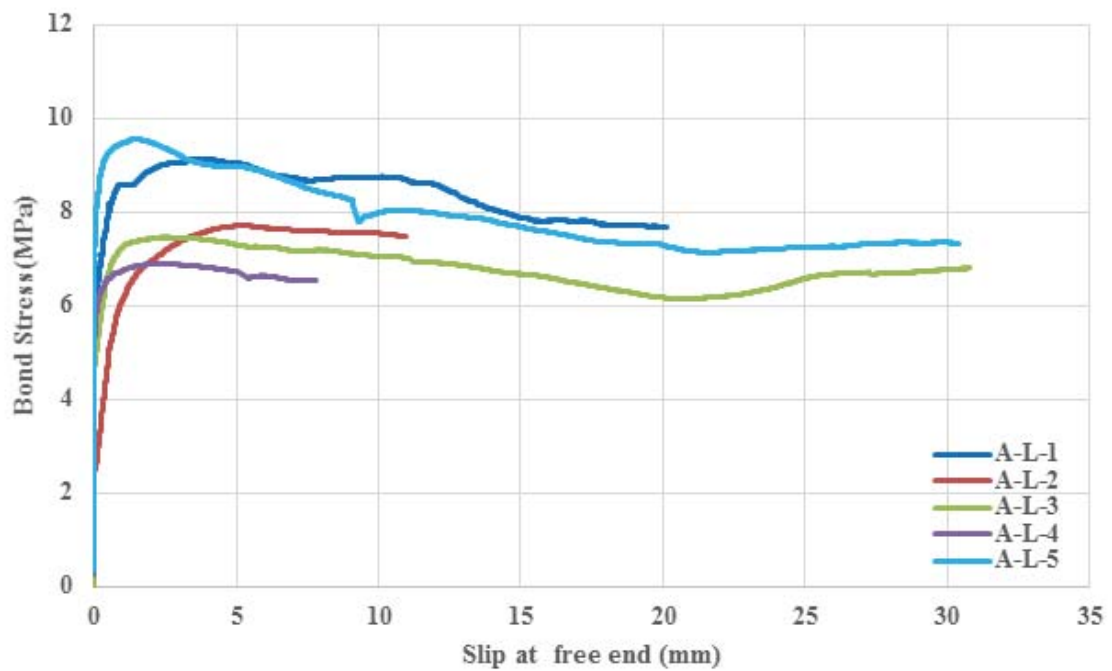


Figure 2.10: Bond-slip results at the free end of GFRP-A with the long embedment length

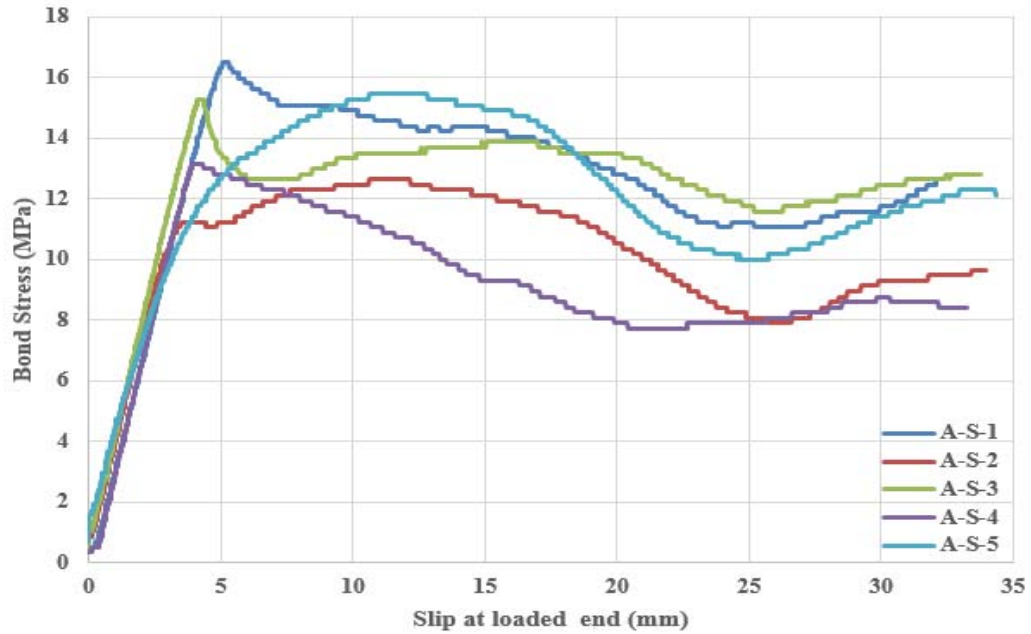


Figure 2.11: Bond-slip results at the load end of GFRP-A with the short embedment length

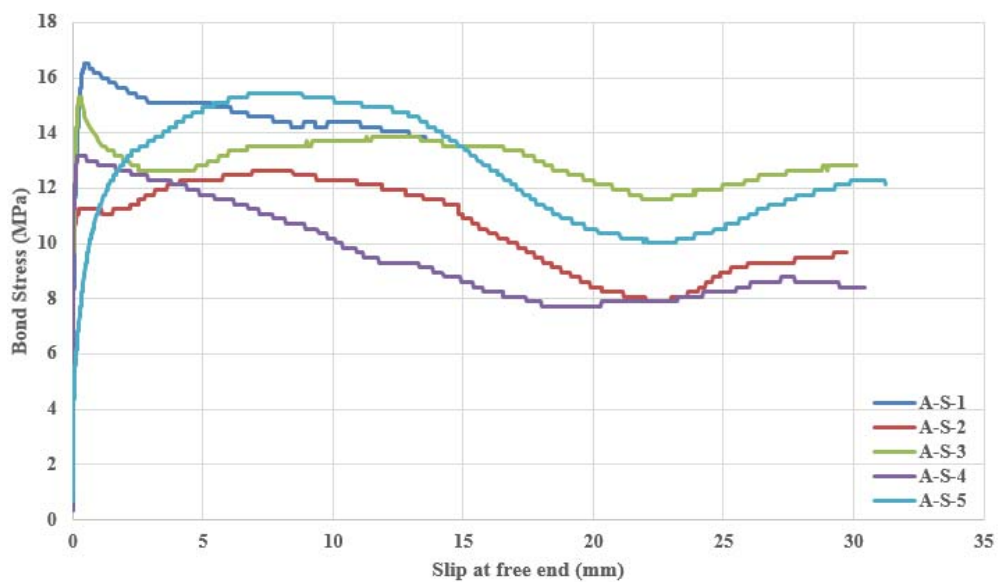


Figure 2.12: Bond-slip results at the free end of GFRP-A with the short embedment length

After the bond stress reached the maximum value, it gradually reduced and finally stayed constant. The tests were stopped when an approximate slippage of 30 mm (1.18 in.) was achieved at the free end of the bar. Table 2.4 shows the detailed results of the tests performed on GFRP-A.

Table 2.4: Results of pull-out tests performed on GFRP-A

Sample ID	F_{\max} (kN)	τ_{ave}^{\max} (MPa)	Bond Failure Mode
A-L-1	74.75	9.12	Pull-through
A-L-2	62.97	7.71	
A-L-3	60.96	7.46	
A-L-4	71.67	8.77	
A-L-5	78.12	9.56	
Ave	69.65	8.53	
SD	6.63	0.81	
COV (%)	9.52	9.52	
A-S-1	42.13	16.50	Pull-through
A-S-2	32.27	12.64	
A-S-3	39.00	15.27	
A-S-4	33.62	13.17	
A-S-5	39.44	15.45	
Ave	37.29	14.61	
SD	3.73	1.46	
COV (%)	10.01	10.01	

Note: 1kN= 0.2248 kips; 1 MPa= 0.145 ksi

The average bond strength increased for samples with shorter embedment length due to generation of more uniform bond stress.

Concrete strength played a negligible role in the bond behavior of GFRP bars with smooth or semi-smooth surfaces (GFRP-A) by presenting the pull-through mode of failure. The bond strength of the bars with deformed surface (GFRP-H and GFRP-C) also depended on the concrete strength due to transfer of high mechanical interlock and the failure occurred by concrete cracking/splitting.

Concrete Modeling

A smeared crack model was employed to model the concrete behavior. This method was developed by Lubliner and coworkers [32] and modified by Lee & Fenves [33]. It

combines the concepts of isotropic damage elasticity with isotropic tensile and compressive plasticity to represent the inelastic behavior of the concrete.

For the concrete under uniaxial compression, the stress-strain relationship below, proposed by Saenz [34], was implemented in Abaqus:

$$\sigma_c = \frac{E_0 \varepsilon_c}{1 + \left(\frac{E_0 \varepsilon_{\max}}{\sigma_{\max}} - 2 \right) \left(\frac{\varepsilon_c}{\varepsilon_{\max}} \right) + \left(\frac{\varepsilon_c}{\varepsilon_{\max}} \right)^2} \quad (2.3)$$

where σ_c and ε_c are the compressive stress and strain, σ_{\max} and ε_{\max} are the experimentally determined maximum stress and strain which are cylindrical strength of concrete (f'_c) in (MPa) for the stress and 0.002 for the strain (Figure 2.13). Concrete used for the pull-out tests was found to have a compressive strength of $f'_c = 57.3$ MPa (COV of 4.6%) obtained by performing compressive tests on cylinders according to ASTM C39/C39M [35]. The elastic modulus of the concrete was estimated from the cylinder compressive strength based on the American Concrete Institute (ACI) 318 equation (i.e. $E_0 = 4730 \sqrt{f'_c}$ in MPa) [36]. The resulted elastic modulus was calculated as $E_0 = 35.8$ GPa.

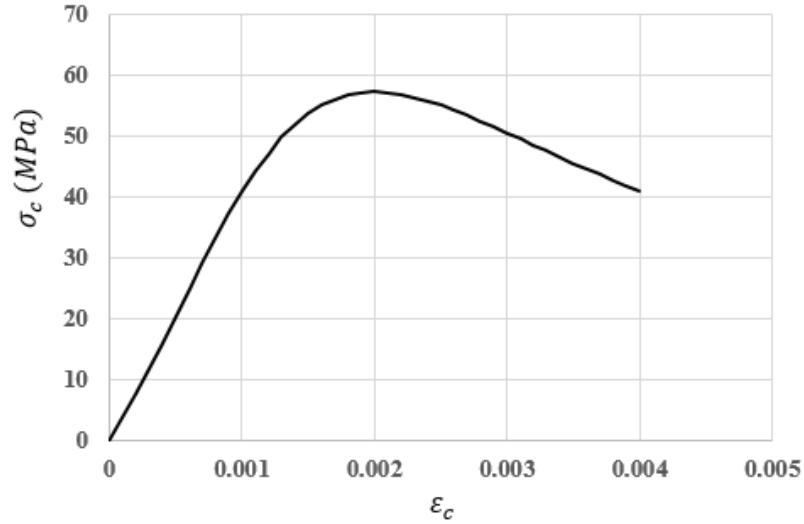


Figure 2.13: The concrete behavior in compression implemented in Abaqus

For the concrete under uniaxial tension, the stress vs. crack opening relation, proposed by Hordijk [37], was employed to present the nonlinear portion of the stress-strain response:

$$\frac{\sigma_t}{f_t} = \left[1 + \left(c_1 \frac{w_t}{w_{cr}} \right)^3 \right] e^{\left(-c_2 \frac{w_t}{w_{cr}} \right)} - \frac{w_t}{w_{cr}} (1 + c_1^3) e^{(-c_2)} \quad (2.4)$$

$$w_{cr} = 5.14 \frac{G_F}{f_t} \quad (2.5)$$

where G_F refers to the fracture energy which is the required energy to create a unit area of the crack surface, w_t is the crack opening displacement, w_{cr} is the crack opening displacement at the complete loss of tensile stress, σ_t is the tensile stress normal to crack direction, f_t is the concrete uniaxial tensile strength. $c_1=3.0$ and $c_2=6.93$ are the experimentally determined constants.

To find the tensile strength of the concrete and fracture energy, the following estimates, proposed by CEM-FIP [38] was employed:

$$f_t = 1.4 \left(\frac{f_c' - 8}{10} \right)^{2/3} \quad (\text{MPa}) \quad (2.6)$$

$$G_F = G_{F_0} \left(\frac{f_c'}{10} \right)^{0.7} \quad (\text{N/mm}) \quad (2.7)$$

where G_{F_0} refers to the base value of the fracture energy and depends on the maximum aggregate size d_{max} (Table 2.5). In this study, d_{max} was equal to 6mm (0.24 in) according to concrete mix design. Any other value than those reported in Table 2.5 were interpolated using the following formula:

$$G_{F_0} = \frac{1}{1000} (0.0469d_a^2 - 0.5d_a + 26) \quad (\text{N/mm}) \quad (2.8)$$

Table 2.5: Base values of the fracture energy for different aggregate sizes

d_{max} (mm)	G_{F_0} (N/mm)
8	0.025
16	0.03
32	0.058

Figure 2.14 presents the adopted model in terms of the concrete tensile strength and the crack opening.

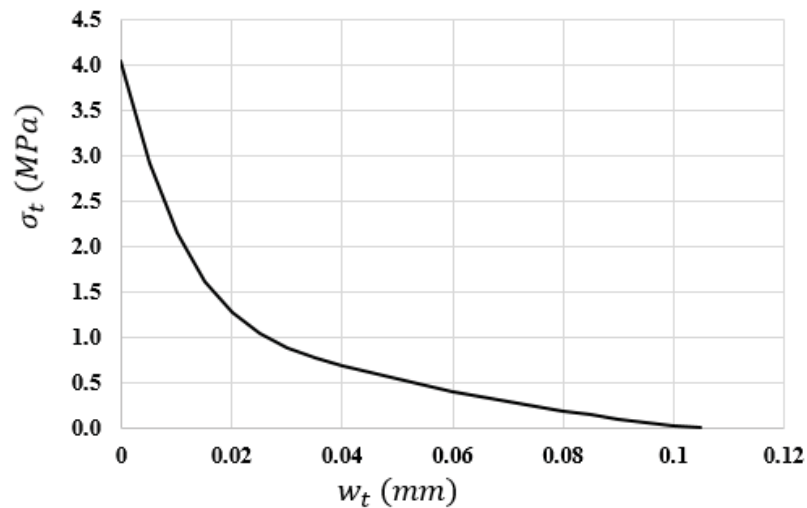


Figure 2.14: Concrete behavior in tension

The main disadvantage of the smeared crack method is being “mesh dependent”. Since the smeared crack model considers the cracks existing at the boundaries of the elements, it leads to zero energy consumption during the crack propagation when the element size approaches to zero. One of the most popular solutions for this problem was proposed by Bazant and Oh [39-41] as the “crack band model” which relates the element size to the constitutive law of the concrete so the fracture energy is independent of the element size. In this model, fracture process zone (FPZ) is the domain in which the micro-cracks evolve $0 < w_t < w_{cr}$ and cohesive stresses are transferred between the crack surfaces till the crack opening reaches a critical value and then the macro-crack occurs. The stress is assumed to decrease gradually in the FPZ with increasing the crack width (w_t). Crack band theory was implemented in this study to eliminate the mesh dependency of the post- failure part of the stress-strain region by considering a crack width related to strain perpendicular to the cracking. Cracking strain (ε_{cr}) was considered to be uniformly distributed along the characteristic length of the element (l_{ch}) as:

$$w_t = l_{ch} \varepsilon_{cr} \quad (2.9)$$

where cracking strain is defined as total strain minus the elastic strain corresponding to the undamaged material $\varepsilon_{cr} = \varepsilon_t - \sigma_t / E_0$.

l_{ch} depends on the element size, type and integration scheme. Since in this study the concrete was modeled using the square plane stress elements (CS4R) with four integration points and linear shape functions, characteristic length was considered to be $\sqrt{2} l_e$ where l_e is the side length of the elements according to Rots [42].

The adopted theory replaced the tensile stress vs. crack opening displacement [σ_t vs. w_t] with a tensile stress vs. cracking strain [σ_t vs. ε_{cr}] relation. The resulted tensile stress relationship is mesh dependent as shown in Figure 2.15 and significantly reduces the strain localization when the element size approaches zero.

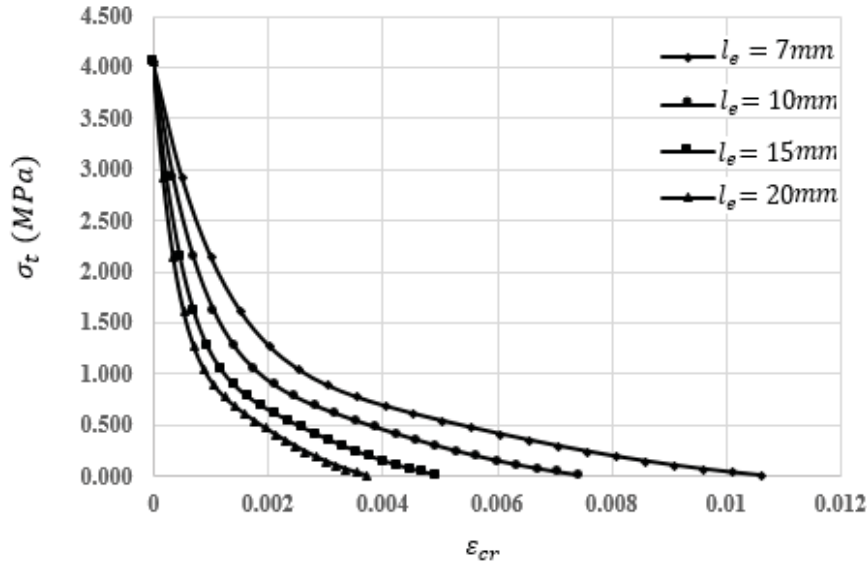


Figure 2.15: Concrete tensile strength vs. cracking strain adopted for different concrete mesh sizes

The post-tensile failure represents the load transfer from the reinforcement to concrete across the cracks by introducing “tension stiffening”. Proper tension stiffening improves the numerical convergence while too little tension stiffening leads to the local cracking failure and unstable respond of the structure.

Numerical convergence problems may happen at the softening regime since the complete non-linearity of the concrete was considered. Hence, a viscosity parameter that allowed slightly exceeding the plastic potential surface area was implemented to regularize the constitutive equations. The viscosity parameter plays a critical role in improving the

convergence rate of the simulation without comprising the results. In this study, 10^{-4} was chosen based on trial and error.

Concrete Damage Model

Tensile damage parameter (d_t) was related to cracking tensile strain (ε_{cr}) using an experimentally obtained parameter $b_t=0.1$ as follows while compression damage played a negligible role in the recent modeling [17].

$$d_t = 1 - \frac{\sigma_t E_0^{-1}}{b_t \varepsilon_{cr} (1/b_t - 1) + \sigma_t E_0^{-1}} \quad (2.10)$$

Cracking strain (ε_{cr}) is modified to plastic strain (ε_{pl}) by incorporating the damage parameter in tension as follows:

$$\varepsilon_{pl} = \varepsilon_{cr} - \frac{d_t}{(1-d_t)} \frac{\sigma_t}{E_0} \quad (2.11)$$

Figure 2.16 schematically shows the effect of stiffness degradation in tensile cracking of the concrete.

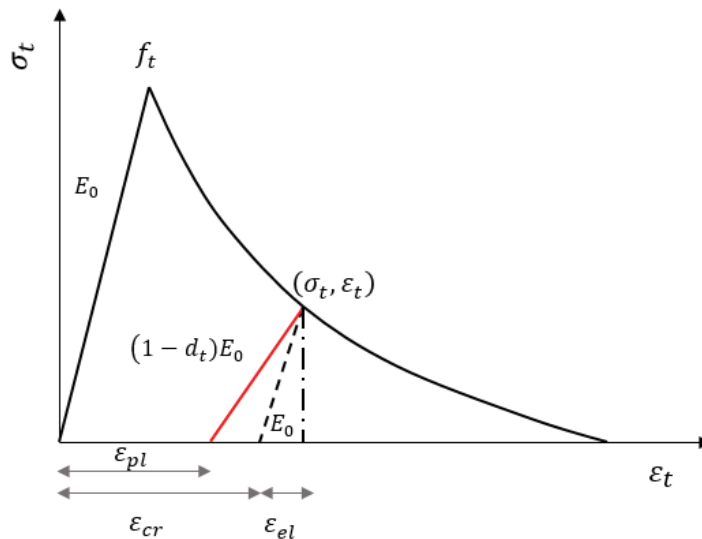


Figure 2.16: Tensile damage of concrete in softening region

Cracks initiate at points where the tensile stress of the concrete exceeds its tensile strength and leads to non-zero plastic strains ($\epsilon_{pl} > 0$).

The direction of the vector normal to the crack plain is assumed to be parallel to the direction of the maximum principal plastic strain. Hence, the plastic strain was adopted to present the crack orientation.

In addition to mentioned constitutive laws and material properties, the following parameters were implemented for the concrete: Poisson's ratio $\nu=0.2$, dilatation angle $\psi=35$, ratio of concrete strength in biaxial compression to the concrete strength under uniaxial compression $f_{b0} / f'_c = 1.16$. Abaqus employs an eccentricity parameter (ϵ) that can be modified for each model to provide a proper convergence rate of the numerical solution. The default value of $\epsilon=0.1$ was considered [43].

FEM Model

The geometry was modeled as a two-dimensional problem while a fictitious third dimension was assumed for both GFRP and the concrete. Considering an equivalent rectangular cross-section with the same area of the actual cross-section ensured that the same amount of material exists in the third dimension. The fictitious width, (w) was calculated as:

$$w = \frac{\pi d}{4} \quad (2.12)$$

where d is the actual diameter.

The GFRP surface was idealized by a cylindrical shape [44] and modeled as a linear-elastic brittle material with the properties presented in Table 2.1. The concrete surface close to the loading end was completely fixed while the concrete surface close to the free end of

the bar was fixed in the lateral direction. A displacement control load was applied at the loaded end of the bar. The load was applied in small increments to avoid any numerical problems. Both GFRP and concrete were modeled using four-node plane stress elements (CS4R). A mesh analysis was performed to investigate the effect of concrete mesh size on the reported results. Three different mesh sizes of 15mm (0.60 in.), 10mm (0.40 in.), and 7mm (0.28 in.) square elements were studied. Since concrete cracking was presented properly with the 7mm (0.28 in.) mesh size, it was employed to present the final results.

Concrete to GFRP Bond Modeling

Translator elements in Abaqus were implemented to simulate the bond action [45-47]. This element consists of two nodes (one in each surface). All the nodes' degrees of freedom are constrained to be the same except for the degree of freedom along the slip direction (u_1). Having this relative displacement as an independent variable, a force being a function of this local variable is assigned to the translator element. Figure 2.17 presents the kinematic configuration of the translator element accompanied by its local coordinate definition.

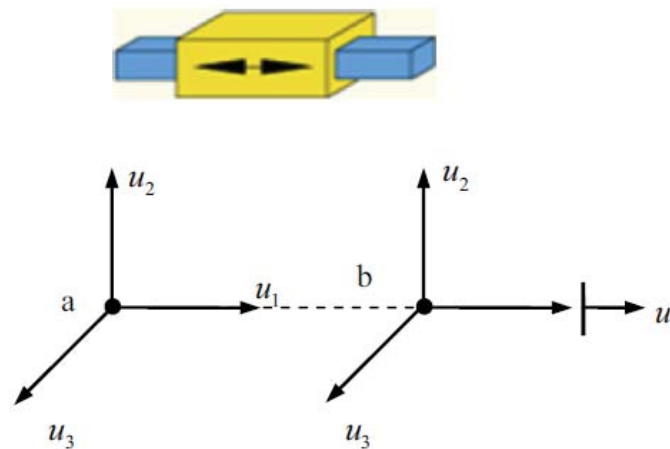


Figure 2.17: The configuration of translator element

Both elastic and damaged parts of the bond response are implemented in the translator elements to present the entire bond behavior. The elastic behavior allows the translator element to behave as a spring in the rising portion of the bond-slip law (either linear or nonlinear). The implementation of the damage behavior covers the degrading portion of the bond law by defining the damage initiation and evolution.

A parametric bond-slip law obtained from the pull-out tests on GFRP-A was employed to assign the bond-slip law for the translator elements. It was assumed that the stiffness of the translator element along the reinforcement was uniform. Assigning the load to each translator element depends on the number of defined translators and their distribution. The load per unit length (f) along the embedment length was calculated as:

$$f = \frac{F}{l} \quad (2.13)$$

where F is the total load and l is the total embedment length of the reinforcement.

Considering the definition of the translator with equal spacing along the reinforcement, the force calculated for each element was found as:

$$F_{tr} = f \times l_{tr} \quad (2.14)$$

where F_{tr} is the force in a single translator and l_{tr} is the spacing between the translator elements. With this procedure, a force was associated to each translator corresponding to any slip values from the experimental pull-out test. Using the extracted data of the translators, the force-slip response can be back calculated.

Parametric Bond-slip Law

A model consists of three stages was proposed in Figure 2.18 for GFRP-A based on the experimental results. τ represents the bond stress and D refers to the slip at the free end of the bar. Five parameters were employed for the bond-slip model.

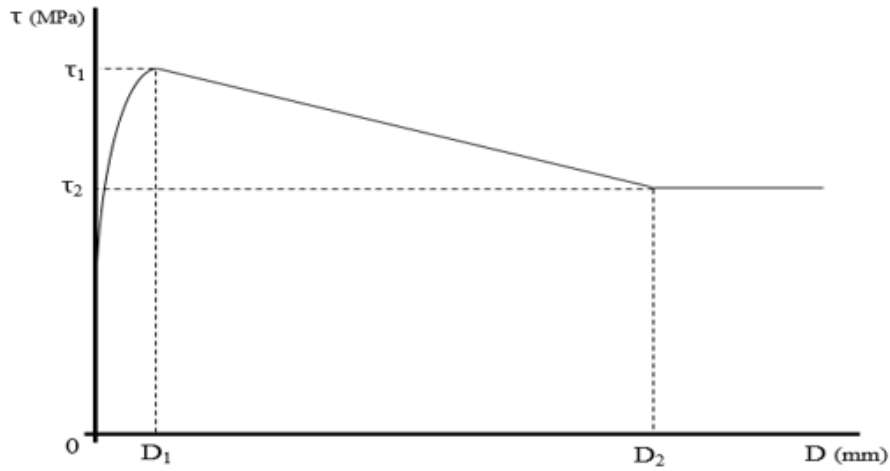


Figure 2.18: Proposed parametric bond slip law

In the first stage, the bond stress exponentially increases to the peak value of τ_1 at the slip level of D_1 :

$$\tau = \tau_1 \left(\frac{D}{D_1} \right)^\alpha \quad 0 \leq D \leq D_1 \quad (2.15)$$

Where $0 < \alpha < 1$ is the exponential parameter.

After the stress reaches to the maximum value of τ_1 , in the second stage, it linearly decreases to τ_2 while the slip at free end is D_2 :

$$\tau = \left(\frac{\tau_2 - \tau_1}{D_2 - D_1} \right) (D - D_1) + \tau_1 \quad D_1 \leq D \leq D_2 \quad (2.16)$$

Finally, in the last stage, the bond stress remains constant.

$$\tau = \tau_2 \quad D_2 \leq D \quad (2.17)$$

Results of FEM Analysis

Connector elements were defined at the embedded portion of the bar at every 30 mm (1.18 in.) and no translator was defined at the debonded portion of the bar.

Sensitivity analysis was performed on parameters τ_1 , α and D_1 to find the bond-slip law compared to the experimental solutions. $D_2=20.32$ mm (0.8 in.) and $\tau_2=6.93$ MPa (1.005 ksi) were extracted as bond properties from the experimental results and were kept constant during the analysis.

Table 2.6 provides the parameters implemented in each sensitivity analysis.

Table 2.6: Implemented parameters in the sensitivity analysis

Analysis ID	D_1 (mm)	α	τ_1 (MPa)
1	1.270, 1.524, 1.778, 2.286	0.1	8.5
2	1.524	0.1, 0.15, 0.17, 0.2	8.5
3	1.422, 1.524, 1.625	0.17	8.5
4	1.524	0.17	8.5, 8.95, 9.33

Note: 1mm=0.0393 in., 1 MPa=0.1450 psi

First, the analysis was performed on combinations of parameter α and D_1 . Figure 2.19 shows the results of the sensitivity analysis performed for four different values of D_1 while the other two parameters were kept constant (Analysis 1).

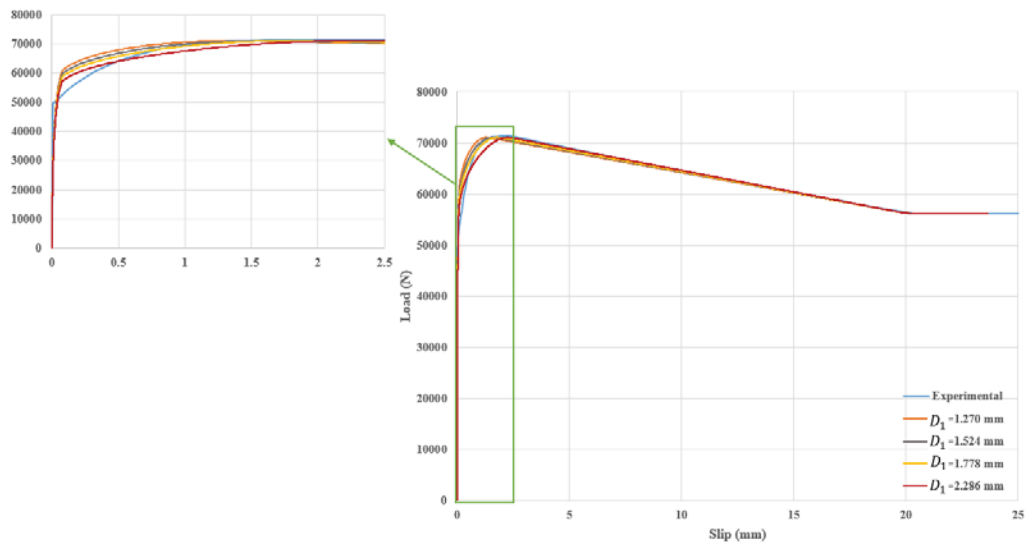


Figure 2.19: Sensitivity analysis on parameter D_1 ; pull-out load vs. slip at the free end compared to the experimental results

$D_I=1.524$ mm (0.06 in.) provided the most accurate model compared to the experimental results. In Analysis 2, the simulation was performed on four different values of α while $D_I=1.524$ mm was kept constant chosen from Analysis 1. The result is shown in Figure 2.20.

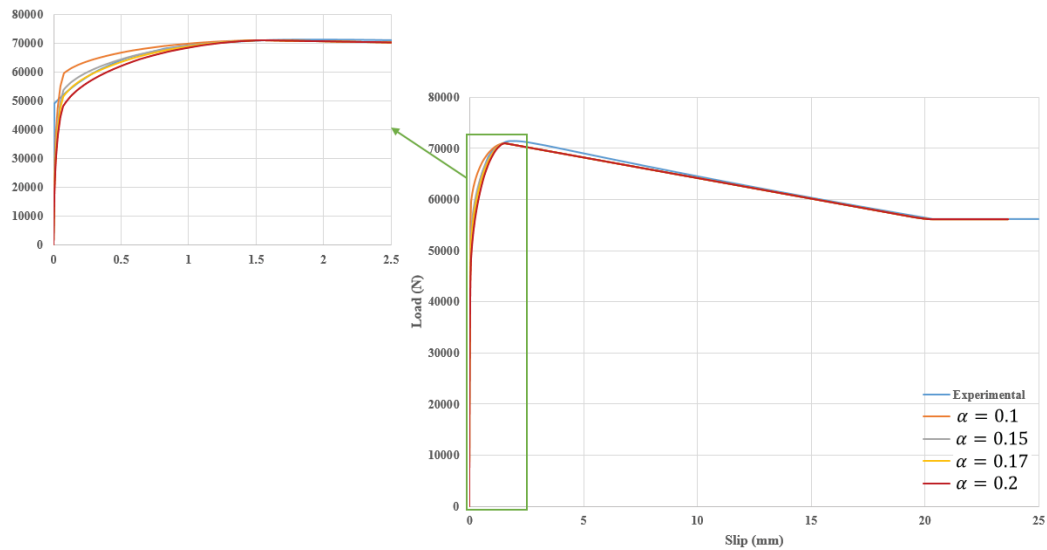


Figure 2.20: Sensitivity analysis on parameter α ; pull-out load vs. slip at free end compared to the experimental results

$\alpha=0.17$ provided the most accurate results compared to the experimental data. In Analysis 3, three more values of D_I were tested to find the most accurate value. The results are provided in Figure 2.21.

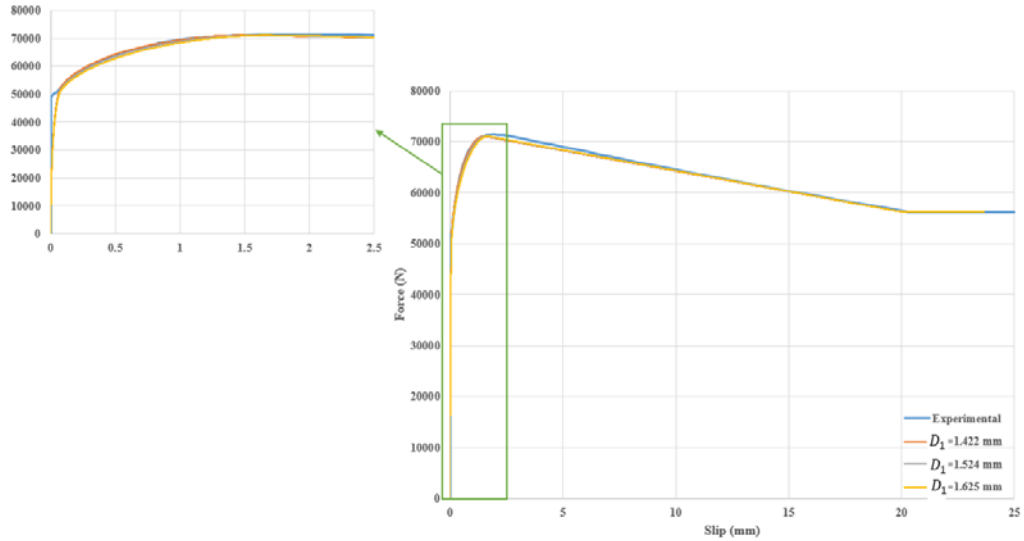


Figure 2.21: Final sensitivity analysis of parameter D_1 ; pull-out load vs. slip at the free end compared to the experimental results

After the first three sets of simulations, $D_I=1.524$ mm (0.06 in.) and $\alpha=0.17$ were chosen as the final values. Finally, the sensitivity analysis was performed on three different values of τ_I .

$\tau_I=8.95$ MPa (1.30 ksi) provided the closest result compared to the experimental ones. The final stage of the sensitivity analysis is presented in Figure 2.22. The maximum obtained shear stress $\tau_I=8.95$ MPa (1.3 ksi) is higher than the average value of 8.53 MPa (1.23 ksi) over the entire embedment length (Table 2.4).

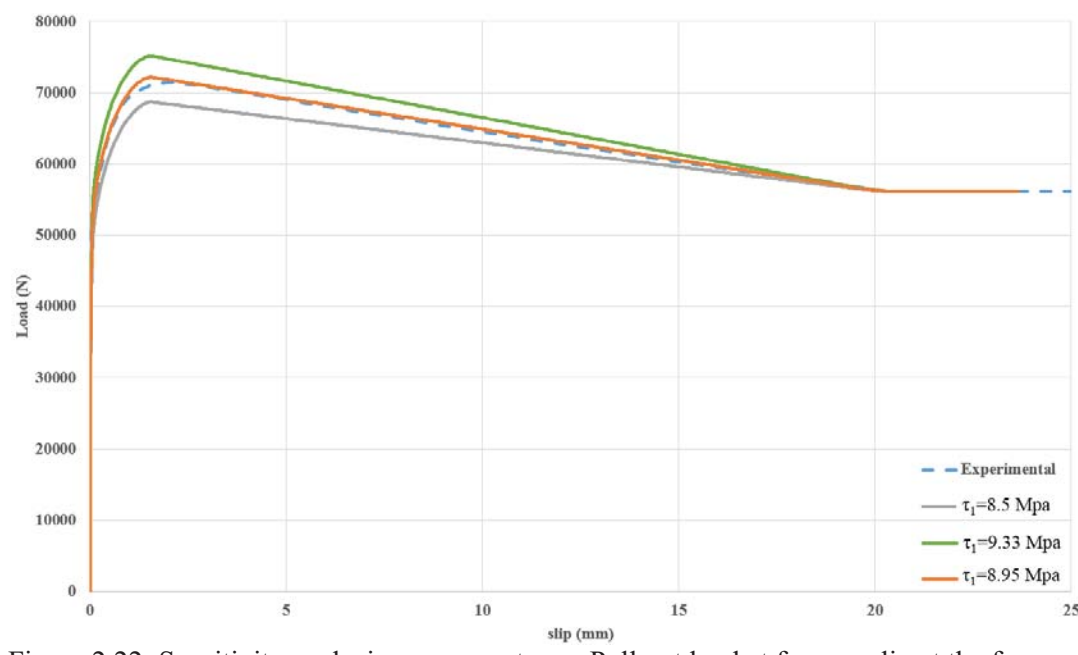


Figure 2.22: Sensitivity analysis on parameter τ_1 ; Pull out load at free vs. slip at the free end compared to the experimental results

The response of the translator elements was studied at the location close to the loaded end (T1), middle of the interface (T4) and close to the free end (T7) as shown in Figure 2.23.

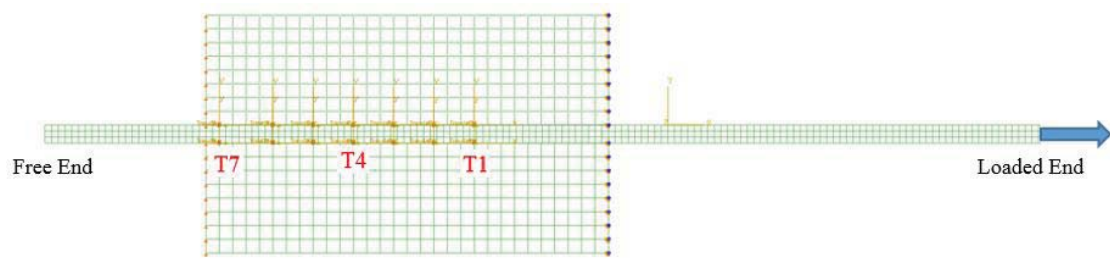


Figure 2.23: Translator elements defined at the interface

The response of the translators at different loading stages are shown in Figure 2.24. At the peak overall load, only the translator closer to the loaded (T1) end reached the peak load while T4 and T7 have experienced a lower load. After the peak overall load, all the translators have reached the peak load while experiencing different displacements.

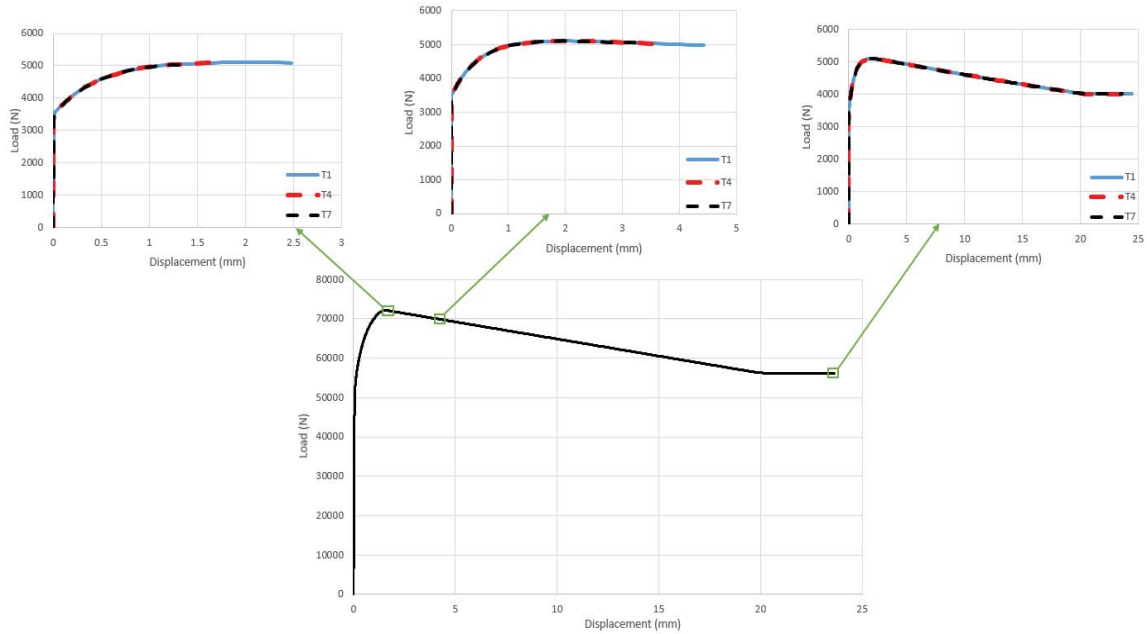


Figure 2.24: The overall force-displacement response at the free end and the response of the translators at different stages of the pull-out load

Figure 2.25 presents the von Mises stress in concrete and GFRP bar. The portions of the bar closer to the loaded end experienced a higher stress and the load in the bar decreases with the embedment length as the load is transformed to the concrete by the bond action.

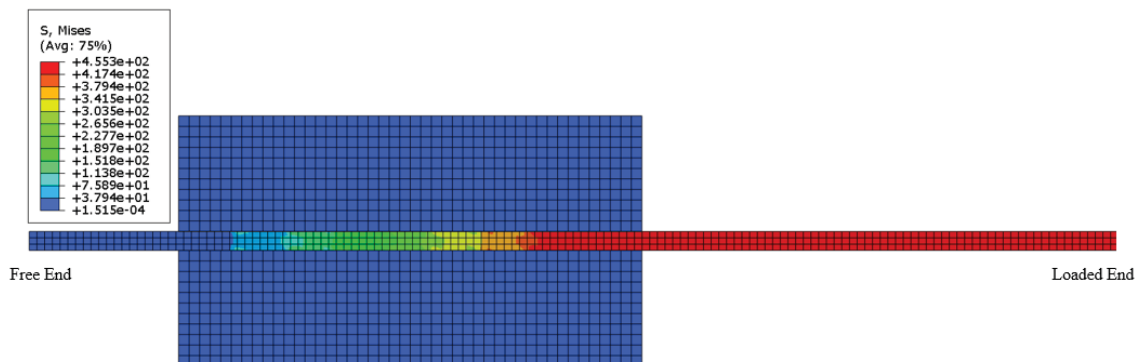


Figure 2.25: von Mises Stress (MPa) in GFRP bar and concrete

The cracking in the concrete is presented in Figure 2.26 by demonstrating the plastic strain. As expected from the experimental results, the level of the mechanical interlock was not high enough for the cracks to propagate through the entire concrete cover. As a result,

the pull-through mode of failure occurred. Longer cracks were noticed in concrete sections closer to the free end. The sections closer to the loaded end underwent more compression due to fixed boundary conditions which resulted in delayed tensile cracking.

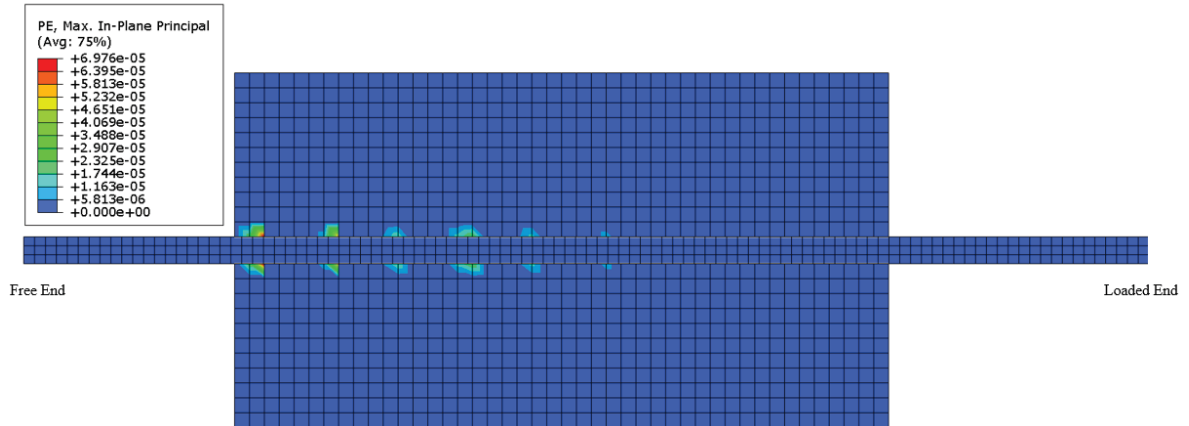


Figure 2.26: Cracks in the concrete due to the bond action

A finite element simulation was also performed for a sample with a smaller concrete cover. Material properties and geometries were kept unchanged while the bar was located closer to the surface of the concrete. The concrete cover was 24.5 mm (1 in.) in this model while it was 68.9 mm (2.75 in.) in the earlier one. The plastic strain illustrating the concrete cracking is presented in Figure 2.27. The load-displacement response of the translators at the final stage of the pull-out load is shown in Figure 2.28. Since the concrete cover was not large enough, the cracks propagated through the entire concrete cover and caused the failure by concrete splitting. The splitting happened after a negligible slippage of the free end of the bar (1 μ m). The applied pull out load was lower than the maximum experienced load in the earlier case.

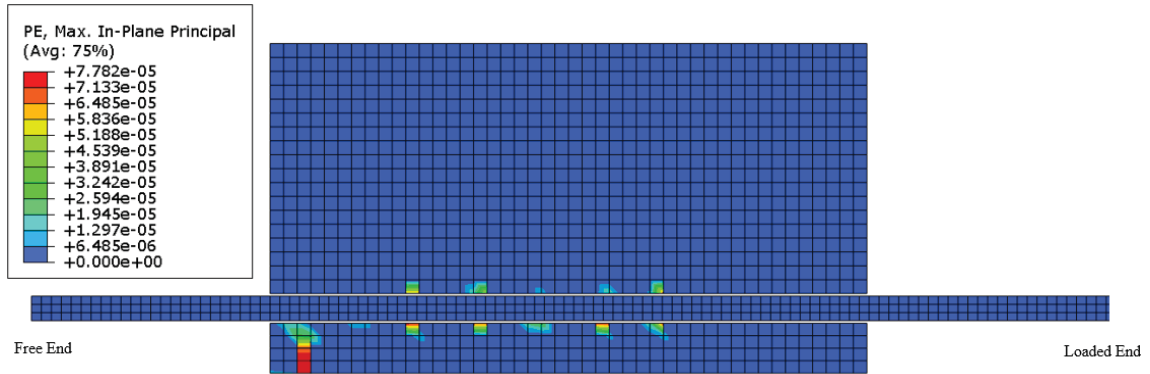


Figure 2.27: Splitting failure of concrete due to propagation of cracks through the entire cover

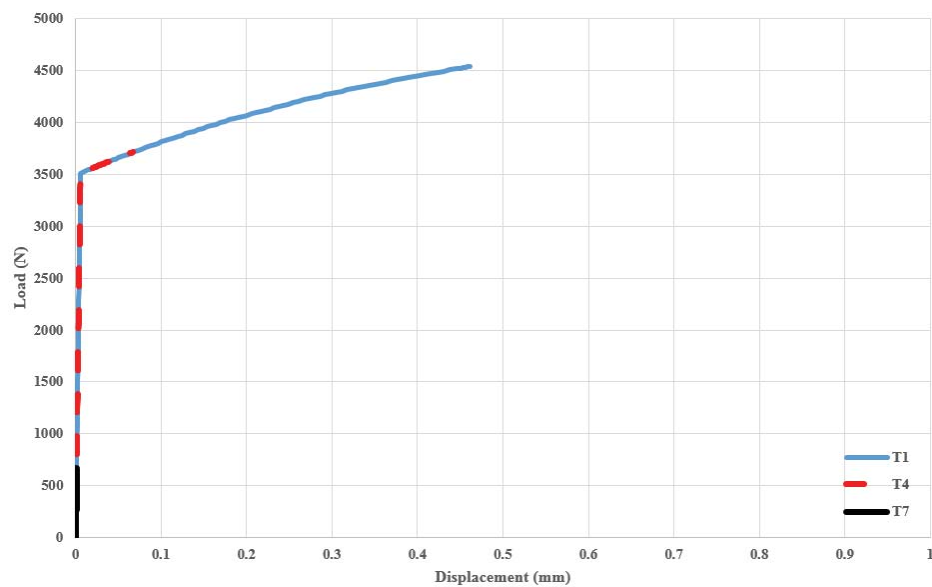


Figure 2.28: Force-displacement response of the translators at the final stage of the pull-out load for the sample with smaller concrete cover

FEM Analysis of GFRP-RC Slab

The bond and load transfer mechanism between reinforcement and concrete plays a critical role in RC structures which has been studied by several researchers [48-50]. It has been demonstrated in the previous section that the employed translators properly simulated the elastic and damaged range of the bond-slip behavior between concrete and the reinforcement. The adopted bond-slip model was implemented in a GFRP-RC slab and the result of the load-deflection from FEM model was compared to the experimental ones. The

analysis was first performed by considering a perfect bond between the concrete and the reinforcement and ignoring any slippage. Next, the bond-slip relationship was implemented between concrete and the reinforcement.

A slab with the geometry specified in Figure 2.29 reinforced with one No. 4 GFRP-A bar was investigated numerically using Abaqus and different effective parameters were investigated using sensitivity analysis.

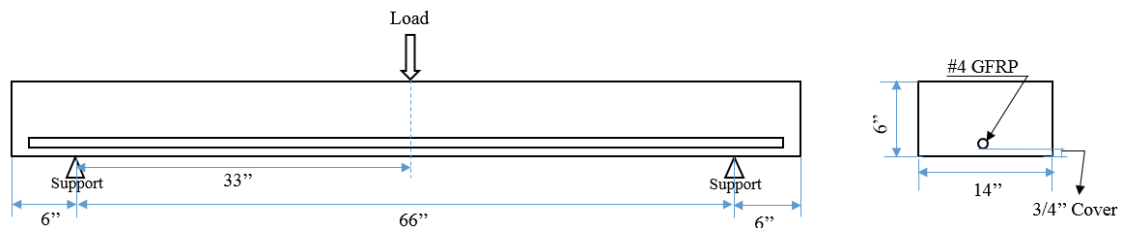


Figure 2.29: Dimension of GFRP-RC slab (Note: 1 in=25.4 mm)

The slab was modeled as a 2D plain stress case which led to a significantly lower computational effort [15, 17-20]. A fictitious thickness was assumed for both the concrete and GFRP reinforcement (2.12) to ensure the same amount of material exist in the third dimension. Due to the symmetry of the load and geometry, only half of the beam was modeled. The symmetry condition was enforced by imposing the longitudinal displacement at the mid-span as zero ($U_1=0$). The other boundary condition was the roller support which implied the vertical displacement to be zero ($U_2=0$) at that point.

First, the self-weight gravity load was applied. Next, the external load was applied in a displacement control configuration by imposing a negative vertical displacement at the top-right part of the mid-span.

The concrete was found to have a compression strength of $f'_c = 31.02$ MPa (4500 psi) [51]. The concrete material property was derived following the same constitutive laws and procedures explained (equation 2-2 to 2-10).

Plain stress square element (CPS4) was chosen for both the concrete and the reinforcement. Four different concrete mesh sizes were investigated for the concrete. To make the concrete plasticity model effective, mesh sizes bigger than the maximum aggregate size ($d_{max}=6$ mm) was chosen. The maximum aggregate size in the concrete was 6.35 mm (0.25 in.) As a result, mesh sizes of 20 mm (0.78 in.), 15 mm (0.60 in.), 10 mm (0.40 in.) and 7 mm (0.28 in.) were investigated [18].

In addition to the mesh size, eccentricity and viscosity parameters in the concrete plasticity model in Abaqus were found to have a considerable impact on the convergence and accuracy of the result. Different values for each of these parameters were considered and proper values were reported. It was also noticed that choosing the proper allowable maximum time increment (t_{max}) is crucial for the numerical convergence and accuracy of the results. Four different limits for maximum time increment were investigated. Table 2.7 presents a summary of all different parameters investigated in the sensitivity analysis.

Table 2.7: Different parameters implemented in sensitivity analysis

Analysis ID	Parameter	Investigated values
1	Viscosity	$10^{-4}, 10^{-5}, 0$
2	Eccentricity	0.1, 0.01
3	t_{max} (s)	0.05, 0.005, 0.001, 0.0005
4	Mesh size (mm)	20, 15, 10, 7

Note: 1 mm=0.0393 in

The concrete to GFRP interaction was considered both as the perfect bond and also considering slippage at the interface. First, the above-mentioned sensitivity analyses were performed while embedding the reinforcement in the concrete and considering the perfect bond (no slippage) to find the proper combination of the parameters. Finally, the selected parameters were employed in the FEM model incorporating the bond action.

Perfect Bond

Models with viscosity parameter equal to zero and 10^{-5} led to problems in convergence rate and nonrealistic oscillations in load-deflection results. The value of 10^{-4} was selected for this parameter. Changing eccentricity parameter (ε) from 0.1 to 0.01 led to similar results. 0.01 was chosen due to providing a faster convergence rate.

Because of the sensitivity of the problem to the applied load increment and cracking phenomena, using both 0.05 and 0.005 as the maximum allowable time increment did not lead to a converged solution. $t_{max}=0.001$ led to a converged solution, the same situation resulted for the case of $t_{max}=0.0005$. In order to have a lower computational cost, the value of 0.001 was chosen.

The mesh sensitivity analysis was performed with three different values of concrete mesh sizes considering the $t_{max}=0.001$. The results of the load-deflection of the mid-span are shown in Figure 2.30. FEM analysis overestimated the results at the first stage of the test which was dominated by concrete property [52]. Concrete demonstrated a lower strength compared to the value considered in the modeling.

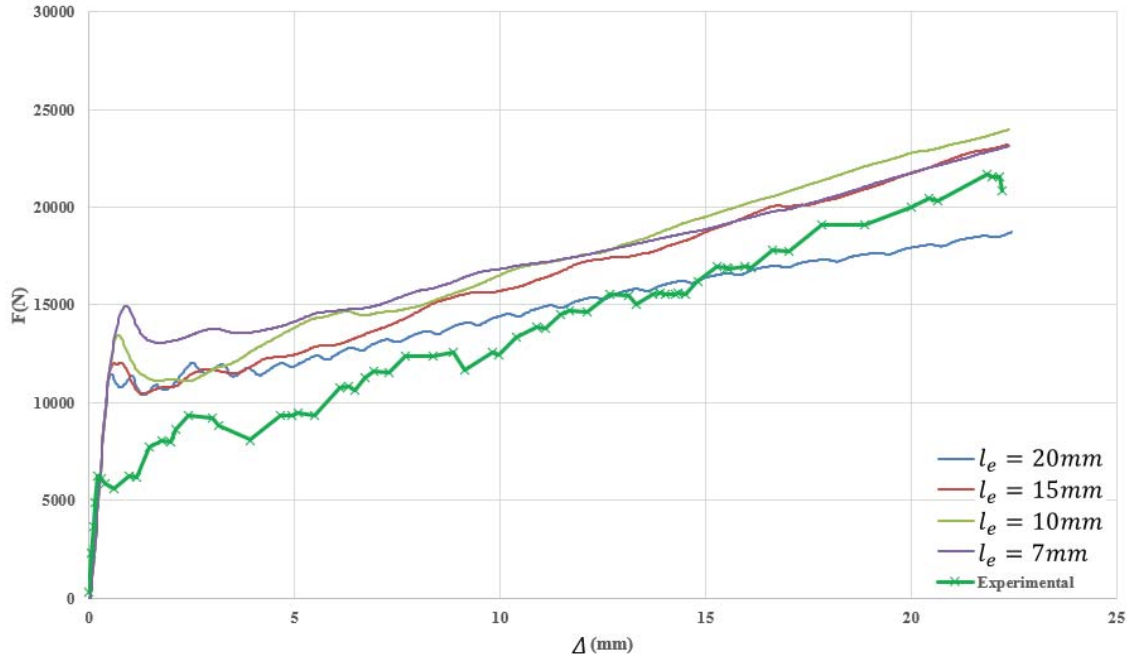


Figure 2.30: Load-deflection results using different concrete mesh sizes and perfect bond

Using the 20 mm (0.78 in.) mesh size resulted in unrealistic oscillations in the load-deflection results while the other three mesh sizes led to acceptable solutions. Due to the importance of concrete cracking, the contour of the plastic strain was investigated to provide the most proper mesh size.

Figure 2.31 and 2.32 show the crack propagation in the slab using the plastic strain contour for the concrete mesh sizes of 20 mm (0.78 in.) and 15 mm (0.60 in.), respectively.

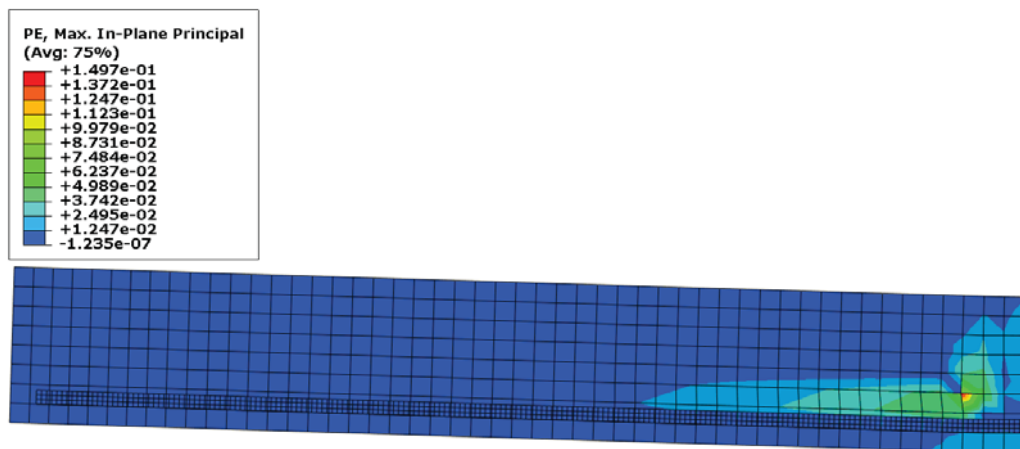


Figure 2.31: Cracks in concrete (plastic strain) in the model with the mesh size of 20 mm

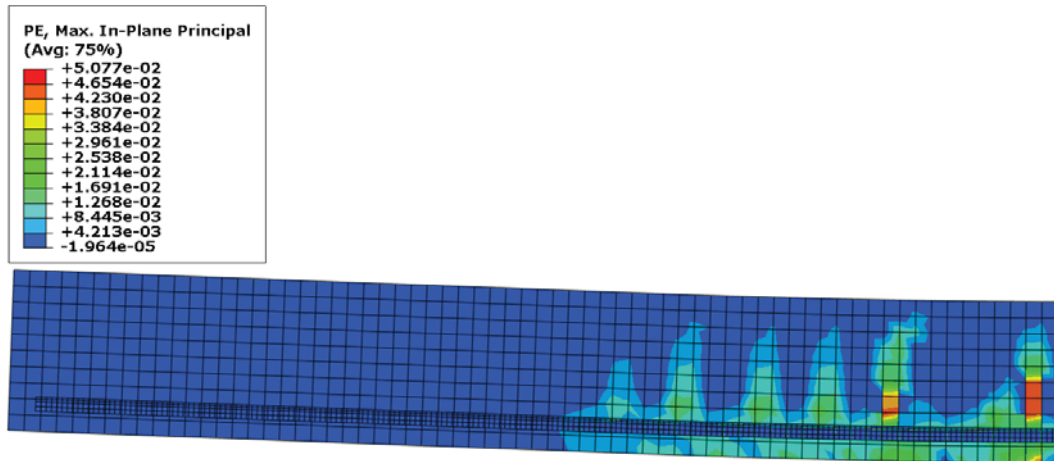


Figure 2.32: Cracks in concrete (plastic strain) in the model with the mesh size of 15 mm

The effect of refining the mesh on the concrete cracking was investigated. With a 20mm (0.78 in.) mesh size, a cracked region was demonstrated instead of real cracks with proper spacing along the slab. The cracks in the concrete below the reinforcement, were properly demonstrated with a mesh size of 15 mm (0.60 in.). Figure 2.33 and 2.34 show the crack propagation in the slab using the plastic strain contour for the concrete mesh sizes of 10 mm (0.4 in.) and 7 mm (0.28 in.), respectively.

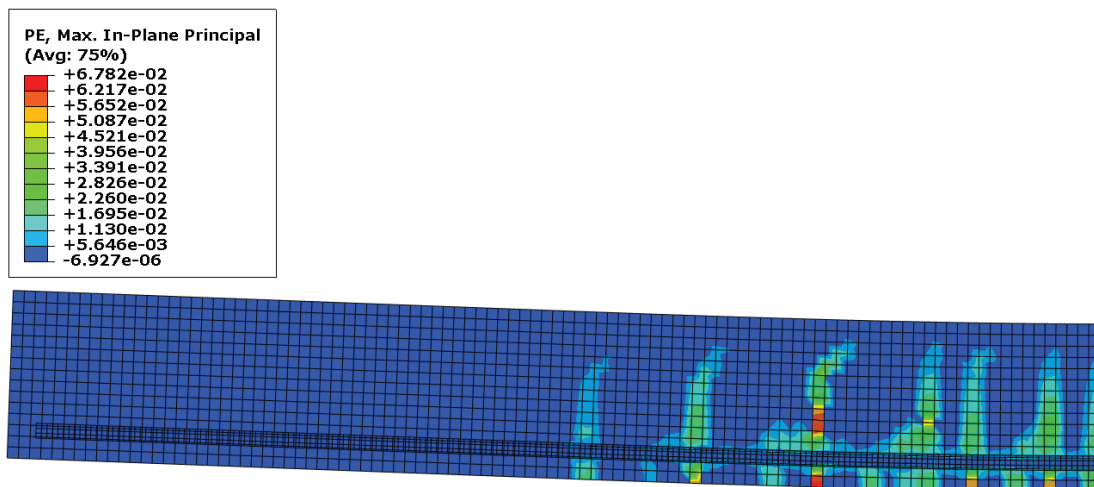


Figure 2.33: Cracks in concrete (plastic strain) in the model with the mesh size of 10 mm

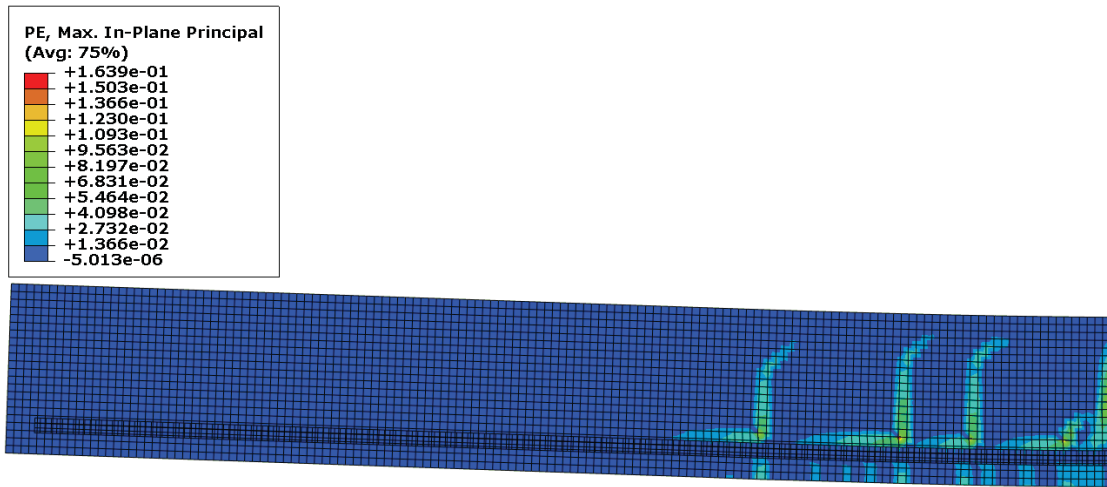


Figure 2.34: Cracks in concrete (plastic strain) in the model with the mesh size of 7 mm

Reducing the mesh size to 10 mm (0.40 in.) provided more acceptable results compared to the mesh size of 15mm (0.60 in.). The cracked concrete below the reinforcement was demonstrated properly instead of having a cracked region using the mesh size of 15mm. Also, the direction of the crack tip was presented properly.

While the results using the mesh size of 7mm (Figure 2.35) presented a proper crack direction, the number of cracks decreased. Refining the mesh did not necessarily lead to more accurate results in numerical modeling of the structure.

Figure 2.35 presents the von Misses stress in the slab. The result of one mesh size is presented since it was not as mesh sensitive as the strain and deflection.

Due to the linear elastic behavior of GFRP bars which did not yield, the stress increased along the length of the bar toward the mid-span. The rupture of the bar at the mid-span occurred when the stress exceeded the tensile strength.

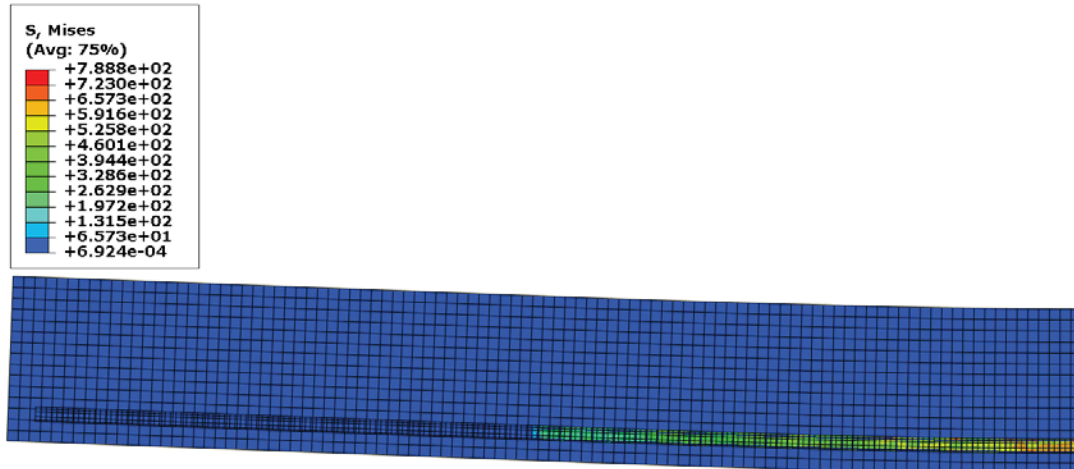


Figure 2.35: von Mises stress in the model with the concrete mesh size of 10 mm

Incorporating the Bond-Slip Model

Translator elements were defined at the GFRP to concrete interface at constant intervals as shown in Figure 2.36. The developed bond-slip model was implemented in the translator elements. The force was divided among the translators as explained in equations 2.12 and 2.13.

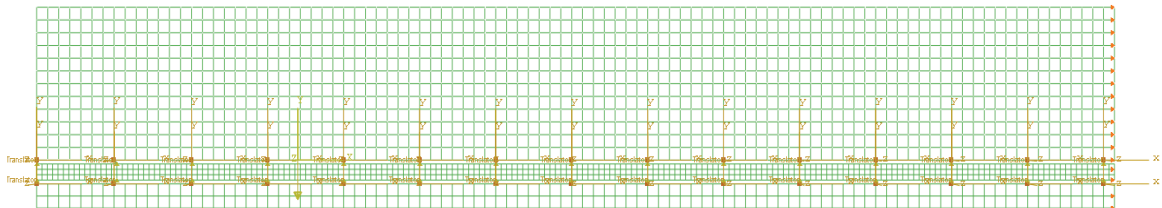


Figure 2.36: Translator elements defined in the GFRP-RC slabs at the concrete interface

A sensitivity analysis was performed to derive the proper spacing of the translators. The translator spacing of 45 mm (1.77 in.) and 75 mm (2.95 in.) were implemented. The concrete mesh sizes of 10 mm (0.40 in.) and 15 mm (0.60 in.) were implemented while the mesh size of the reinforcement was not found to considerably affect the results. The mesh size of 15 mm was chosen for the GFRP.

Figure 2.37 shows the result of the load deflection at the mid-span by defining translator elements at equal intervals of 75 mm for two concrete mesh sizes and the results are compared to the experimental data [51].

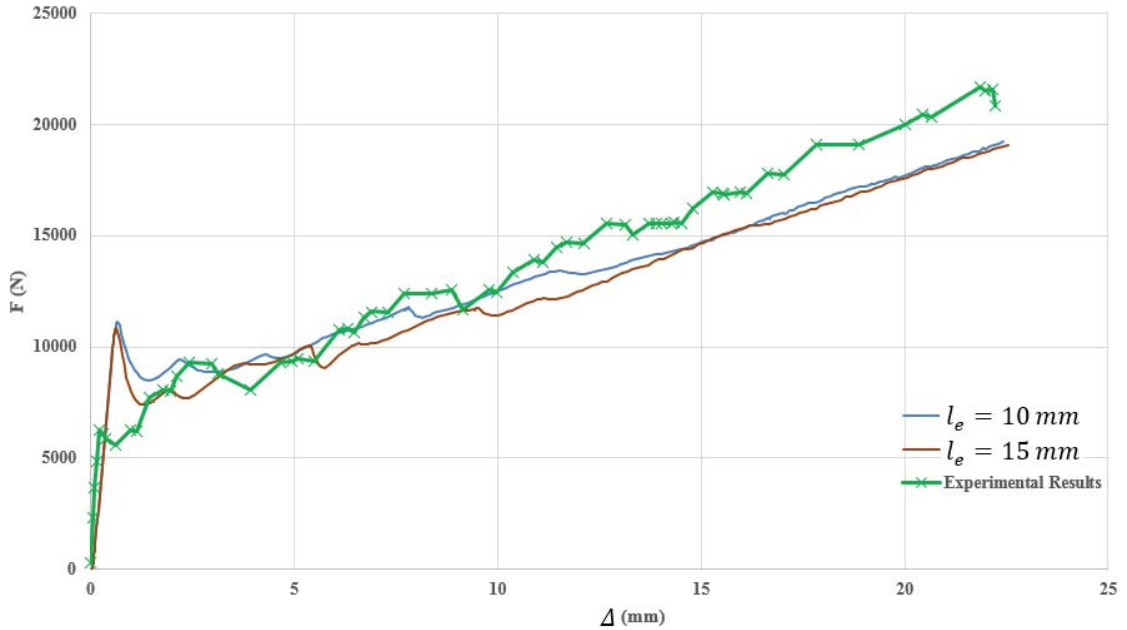


Figure 2.37: Load vs. mid-span deflection results of GFRP-RC slab using translator elements at the spacing of 75 mm

Using the 75 mm spacing led to acceptable results for both concrete mesh sizes of 10 mm and 15 mm. A smaller spacing for the translators was also adopted to provide more accurate results. As a result, spacing of 45 mm was chosen. The results are shown in Figure 2.38 and compared to the experimental data [51].

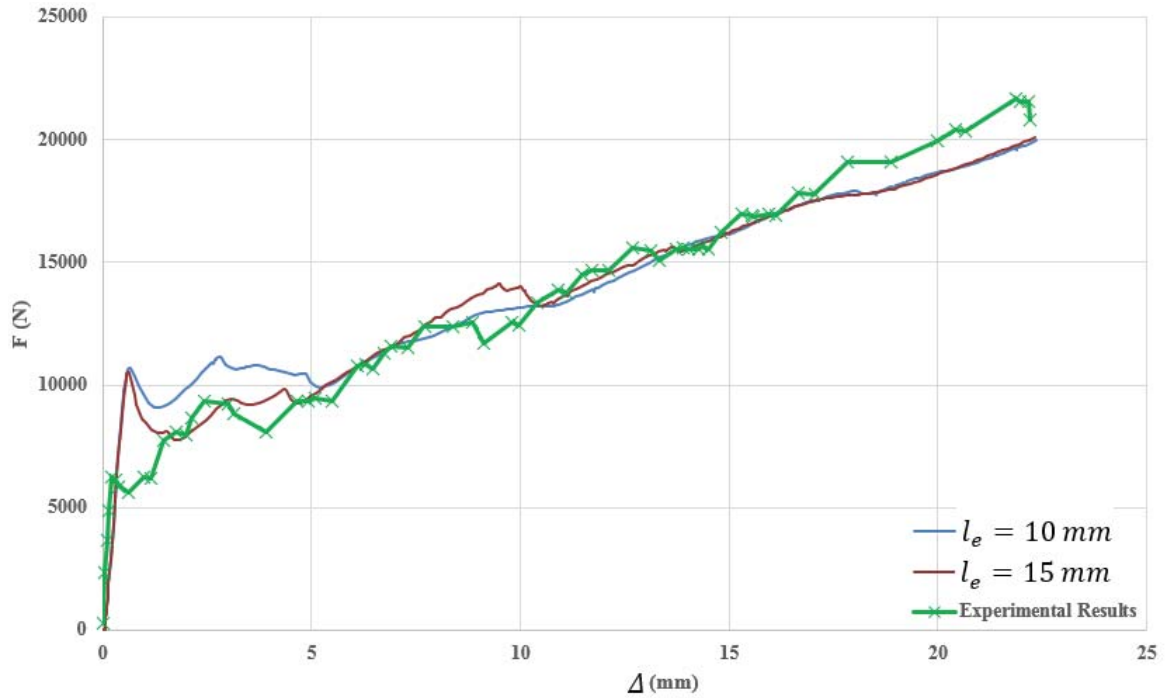


Figure 2.38: Load vs. mid-span deflection results of the GFRP-RC slabs using the translator elements with the spacing of 45 mm

Implementing translators at equal spacing of 45 mm led to more accurate results. The concrete size of 15 mm provided more accurate results compared to the mesh size of 10 mm.

Figure 2.40 compares the load-deflection response of the slab at mid-span comparing the perfect bond model, the final selected model implementing the bond-slip relationship with the experimental results.

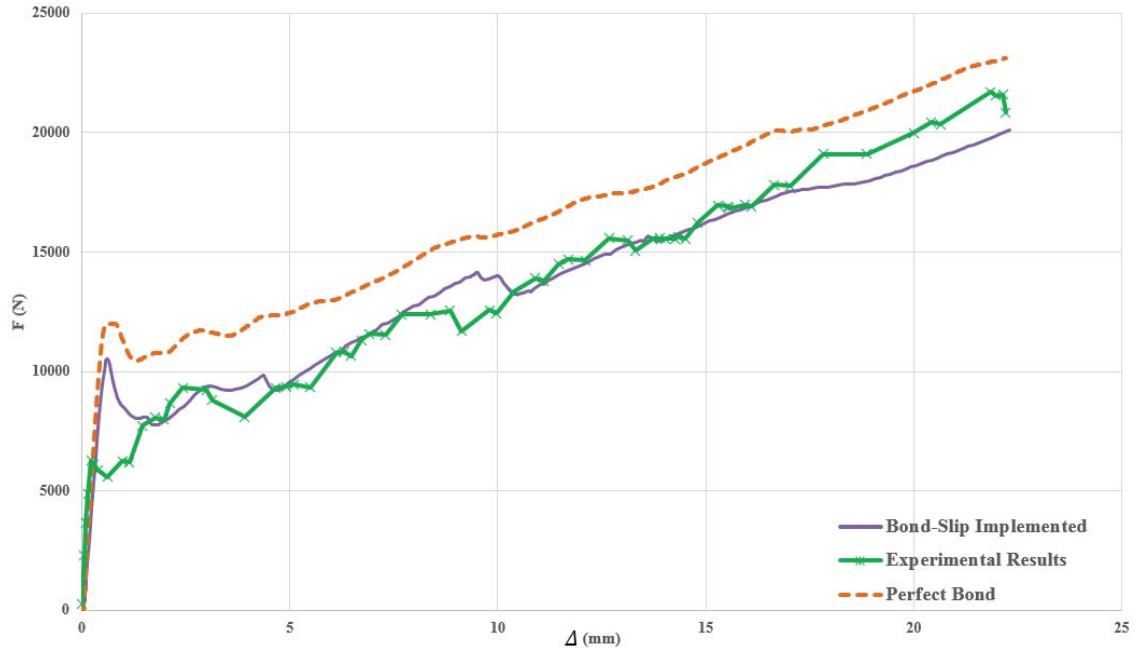


Figure 2.39: Load-deflection at the mid-span of the GFRP-RC slab compared to experimental results

As shown in Figure 2.39 ignoring any possible slippage overestimated the results. Implementing the bond-slip provided more accurate results of the load-deflection at the mid-span of GFRP-RC slab. At the same time, from the design point of view, the perfect bond assumption for the GFRP-RC slab was accurate enough.

Figure 2.40 shows the cracking in the concrete (plastic strain) while implementing the bond-slip model.

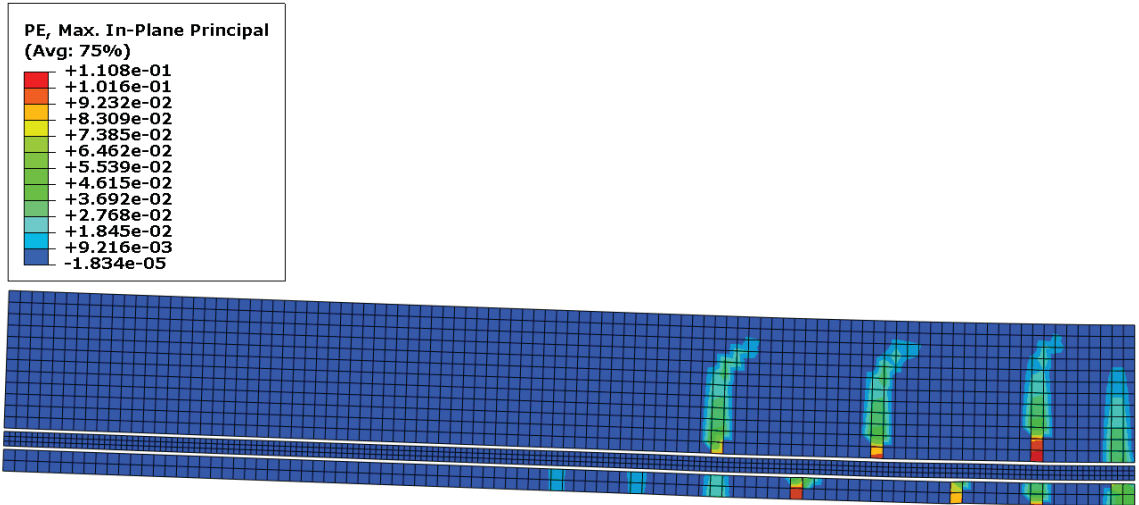


Figure 2.40: Concrete cracking in the model incorporating the bond-slip relationship

Bond Coefficient (k_b)

Crack width is one of the main serviceability limits in design of RC structures. In steel-RC structures, limiting the crack width is critical to avoid the corrosion. In case of GFRP-RC structures while corrosion is not an issue, crack width is still limited for aesthetic reasons and to also avoid water leakage [1]. The maximum crack width at the tension face of a flexural member, w_c , is recommended in ACI 440.1R [2] based on the work of Frosch [53] as follows:

$$w_c = 2 \frac{f_f}{E_f} \beta k_b \sqrt{d_c^2 + \left(\frac{s}{2}\right)^2} \quad (2-17)$$

where f_f is the reinforcement stress, d_c is the concrete cover from tension face to the center of the closest bar, s is the bar spacing, β is the ratio between the displacement from the neutral axis to the tension face of the member and the distance from the neutral axis to the centroid of the tensile reinforcement and k_b is the bond coefficient.

ACI 440.1R recommends a conservative value of 1.4 when k_b is not based on experiments. Reducing this conservative parameter may lead to an efficient use of GFRP

materials in construction, lower the economic cost and result in enhancing the use of GFR as concrete reinforcement. Numerical modeling of GFRP-RC structures which incorporate the bond-slip relationship between concrete and the reinforcement and capture the concrete cracking in concrete (such as the model developed in this study) can propose a more realistic estimation of this property¹.

Concluding Outcomes

Pull-out tests were performed on three different GFRP bars with different surface characteristics to determine the bond strength. Two sets of samples with different embedment length were tested for each bar. Based on the reported results, the following can be concluded:

- The GFRP bar with the highly deformed surface (GFRP-H) failed with sudden concrete splitting. The level of the transferred load from the reinforcement to concrete was high. The average bond strength was 6.81 MPa for samples with 203.2 mm (8 in.) of embedment length while it increased to 16.11 MPa for samples with short embedment length of 63.5 mm (2.5 in.) due to generation of more uniform bond stress.
- The GFRP bar with the ribbed surface (GFRP-C) failed with the separation of the surface enhancement for samples with the long embedment length. The shear stress generated by the bond action exceeded the shear strength of the attached enhancement surface. The average bond strength was determined as 19.80 MPa for samples with the short embedment length. A considerable slippage was observed

¹ Addressing the k_b factor was out of the scope of this dissertation and will be addressed in future publications.

at the free end of the bar before the final failure. The failure occurred by concrete cracking without any sudden splitting.

- The sand coated, fiber wrapped (GFRP-A) bars demonstrated a bond strength of 8.53 MPa for samples with long embedment length which increased to 14.61 MPa by reducing the embedment length due to generation of more uniform stress. The concrete cover was 68.9 mm (2.75 in.) and all the samples presented the pull-through mode of failure since the cover was large enough to prevent the splitting of concrete.
- A parametric nodal bond-slip relationship consists of five parameters was proposed for the GFRP-A. The proposed law consisted of three different stages. Exponentially rising, linearly descending and residual constant stress. A sensitivity analysis was performed to find the parameters of the bond law compared to the experimental results. The proposed explicit bond model can be applied to any arbitrary GFRP bar with various types of surface characteristics and diameter.
- The parametric bond law was employed in a finite element model which captured the concrete cracking and was capable of presenting both pull-through of the bar and the concrete splitting by explicitly modeling the bond action between concrete and reinforcement. The difference between average and nodal bond-slip relationship was investigated by monitoring the bond action at different locations along the embedment length of the bar.
- A simulation was performed on a sample with a concrete cover of 25.4 mm (1 in.). The model predicted the splitting failure mode of the concrete emphasizing the importance of the concrete cover on final failure mode.

- The proposed bond-slip model was implemented in a GFRP-RC slab reinforced with GFRP-A bars. The FEM analysis was performed for two cases of perfect bond, and by implementing the bond-slip relationship. The results were compared to the experimental data. Considering the slippage between the reinforcement and concrete led to more realistic and precise predictions of the load-deflection results compared to the case which did not consider any slippage. At the same time, the perfect bond assumption was accurate enough for the design of GFRP-RC element.

Future Research

More experimental tests should be conducted to investigate the effect of GFRP surface characteristics in bond properties to concrete. The future studies can address the detail characteristics of the surface enhancements such as roughness for the sand coated bars and rib geometry for the GFRP bars with ribbed surface. Numerical models which incorporates the bond-slip model between GFRP and concrete can lead to more realistic bond reduction factor (k_b). Additionally, capturing the cracking in the surrounding concrete can be used in suggesting optimized required concrete cover for GFRP bars implemented in different applications.

Chapter 3-GFRP Microstructural Investigation

GFRP consists of the glass fibers as load carrying elements and the resin which transfers and distributes the load among the fibers. Microstructural patterns of the fibers and resin play a crucial role in understanding the GFRP behavior. Different manufacturing parameters (e.g. pulling speed and dye temperature) lead to various GFRP microstructural patterns including the presence of the voids and defects at various locations of GFRP cross-section. These patterns present combinations of connected defects and disconnected voids and lead to a unique pattern for each GFRP bar type. Understanding the GFRP microstructural pattern may lead to predicting the GFRP behavior under different loading conditions and states of stress. Since there is a lack of GFRP microstructural knowledge in the literature, the main purpose of this chapter is to provide a documentation of GFRP microstructure and investigate its possible contribution on GFRP durability.

In the present study, four commercially available GFRP bars with a nominal diameter of 12.7 mm (0.5 in.), equivalent to No. 4 steel rebar, were investigated. First, samples were properly polished and prepared for the microscopic examination. Next, SEM imaging was employed at different magnification levels to capture different aspects of the microstructural pattern including i) existing defects/voids in the matrix; ii) fiber-matrix interface; and, iii) fiber distribution in the matrix. Panorama images of the entire cross-sections were provided to give a proper comparison between different bars. Investigations were performed on several samples for each bar type and similar patterns were observed.

In the final section of this study, the possible effect of the microstructural patterns in GFRP durability was investigated [54-56]. Two types of the bar that demonstrated the most different microstructural patterns were exposed to accelerated conditioning. The horizontal

shear test was performed and the results were compared with the pristine bars. Finally, SEM imaging and EDS analysis were performed on the conditioned bars to provide additional evidence of the effect of microstructural patterns on durability.

GFRP Samples

Four different GFRP bars with different surface characteristics were investigated in this study: Fine sand coated with the helically wrapped fibers (GFRP-A), double twisted fiber wrapped (GFRP-B), ribbed deformed surface (GFRP-C) and coarse sand coated (GFRP-D). Table 3.1 provides the nominal and measured cross-sectional areas for all the GFRP bar types. The nominal area is based on a circle with nominal diameter of 12.7 mm (0.5 in.). The average measured area was computed based on a work by Claire and coworkers [30] following a standard test method for density and specific gravity (relative density) of plastics by displacement, ASTM D792 [31].

Sample Preparation

Three GFRP samples for each bar type were cut in an approximate thickness of 7 mm (0.27 in). The specimen surfaces were prepared by sanding using different levels (i.e., 180, 300, 600 and 1200) of sand paper and employing dedicated grinding and polishing equipment. Fine polishing completed the specimen preparation using a wet-polishing agent and polycrystalline diamond paste. Prior to imaging, specimens were placed in an oven at 60°C (140 °F) for 24 hours to remove moisture produced during the polishing procedure. Samples were properly cleaned using an air-blower which also saved the SEM chamber from being contaminated and provided higher quality images. Since GFRP was a non-conductive material, an ion sputtering device was used to coat the samples with gold prior

to SEM examination. Figure 3.1 provides a photo of the final prepared samples prior to the microscopic examination.

Table 3.1: GFRP nominal and measured cross-sectional areas





Specimen ID	GFRP	Area				Diameter (mm)			
		Nominal		Measured		Nominal		Measured	
		mm ²	in ²	mm ²	in ²	mm	in	mm	in
GFRP-A		126.5	0.196	137.8	0.214	12.7	0.5	12.7	0.522
GFRP-B				152.6	0.237			13.9	0.549
GFRP-C				130.5	0.202			12.6	0.507
GFRP-D				162.6	0.252			14.7	0.567



Figure 3.1: Final prepared GFRP samples (from left: GFRP-A, B, C, and D)

SEM Imaging

SEM was conducted at low (0-200x), medium (200-1000x) and high (>1000x) magnification levels. Low magnification images provided a general pattern of the cross-section by covering a higher area in each image. This level was used to measure the length of the existing defects. The images captured in this level were stitched together to prepare the panorama image of the entire sections. Medium level magnification images provided a more detailed view of the section and eventually high-level magnification imaging was mainly conducted to monitor the single glass fibers.

Results

GFRP-A displayed a continuous defect along the edge as shown at different magnification levels in Figure 3.2. These defects were not the result of sample preparation since similar pattern were observed in multiple samples of GFRP-A. Disconnected voids were observed at the entire cross section. The void numbers increased at the vicinity of the edges compared to the central portion of the section (Figure 3.3).

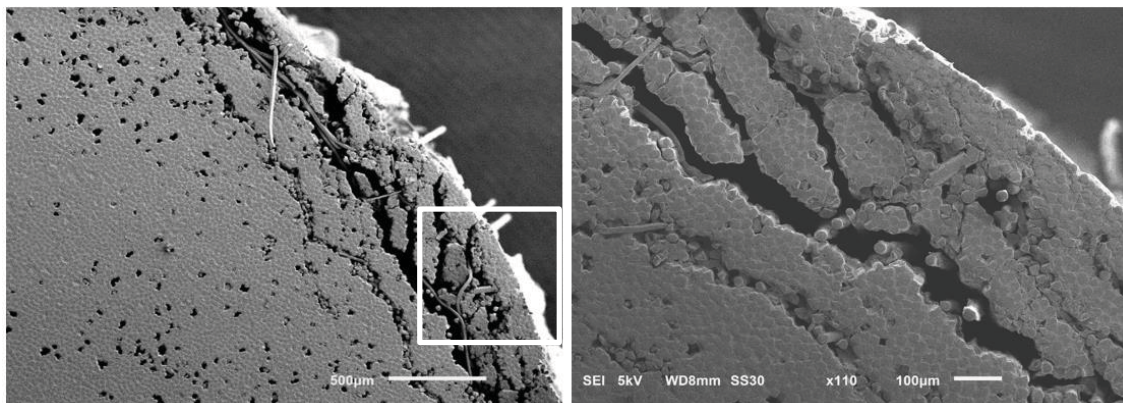


Figure 3.2: A continuous defect at the edge of GFRP-A at magnification levels of 40x (left) and 110x (right)

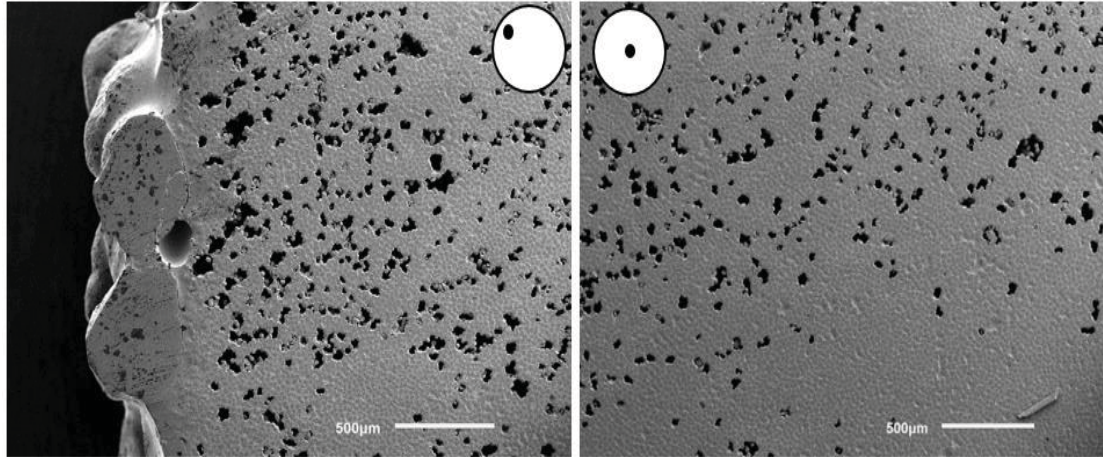


Figure 3.3: Distributed voids in the cross-section of GFRP-A: close to the edge (left), close to the center (right)

GFRP-B displayed both connected defects and disconnected voids in the cross-section including the central portion and edges while no defects were observed at the surface of the bar (Figures 3.4-3.6). The continuous defect patterns across the entire section is problematic for durability, especially the ones close to the edges since deterioration of the reinforcement due to the diffusion of chemical and environmental attacks initiate at the boundaries.

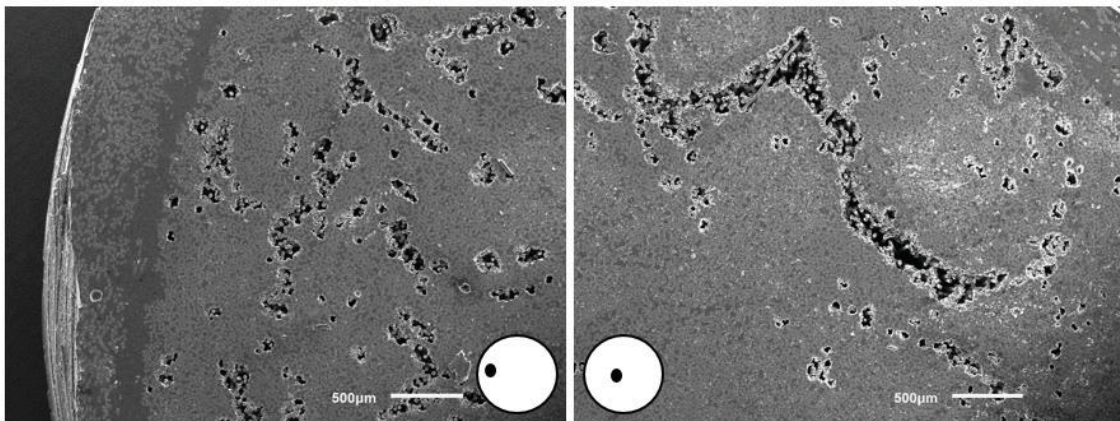


Figure 3.4: Connected void patterns at the edge (left) and at the center (right) of GFRP-B

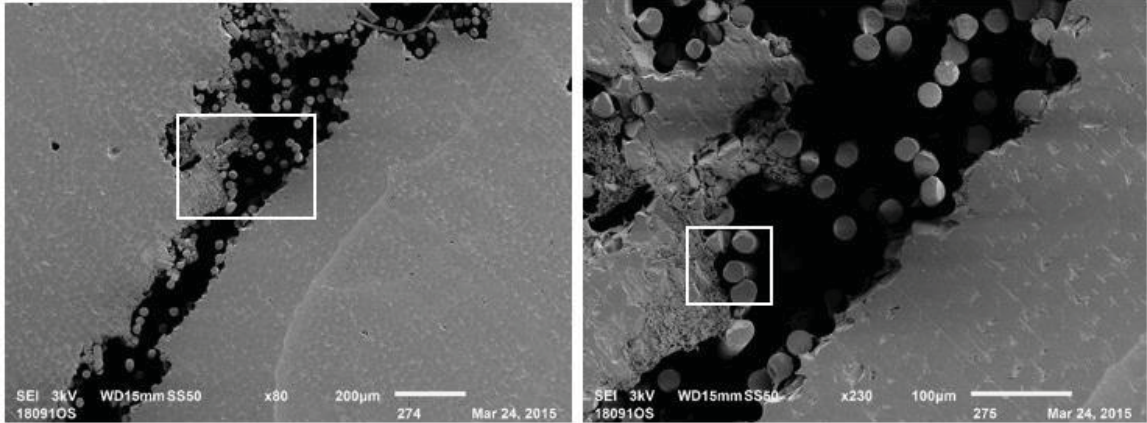


Figure 3.5: Detailed view of a defect close to the edge of GFRP-B at magnification levels of 80x (left) and 230x (right)

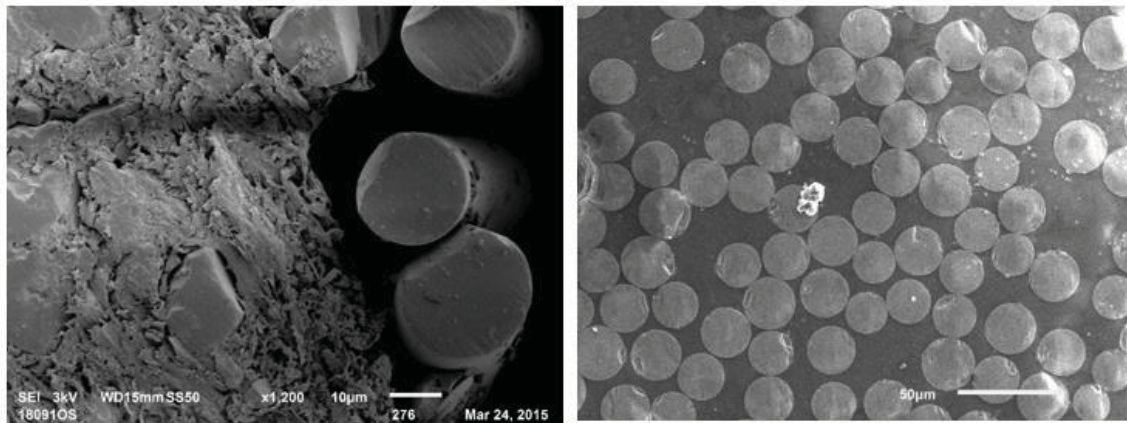


Figure 3.6: High magnification image of a void (left) and area with no void (right) of GFRP-B

GFRP-C presented a continuous defect at the edge (Figure 3.7). A large void with the length of 1.38 mm (0.054 in.) was observed at the center of the bar (Figure 3.8). The rest of the cross-section did not show any voids/defects and the resin properly impregnated the fibers (Figure 3.9).

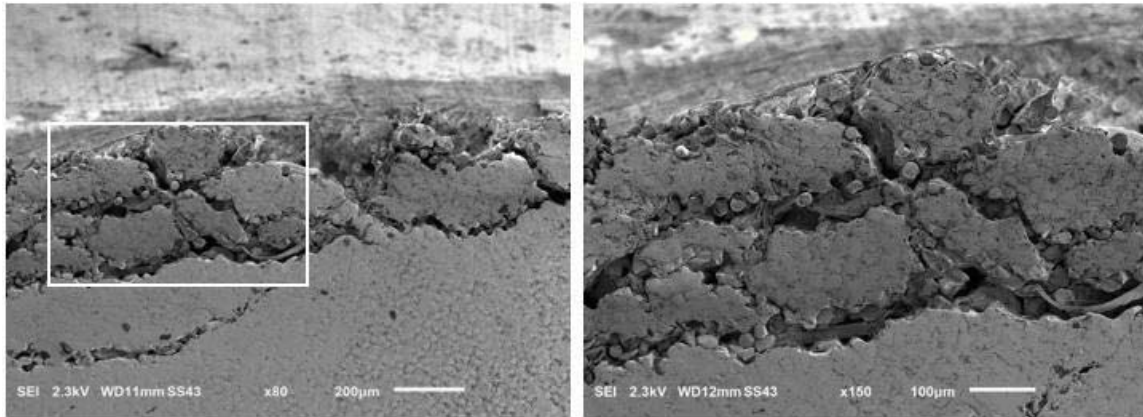


Figure 3.7: A defect at the edge of GFRP-C at magnification levels of 80x (left) and 150x (right)

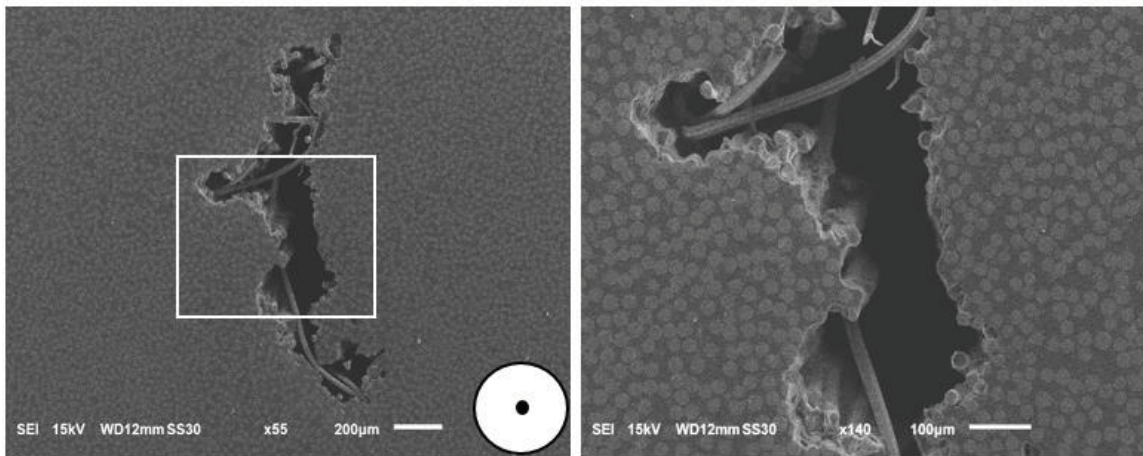


Figure 3.8: Detailed view of a void in the center of GFRP-C at magnification levels of 55x (left) and 140x (right)

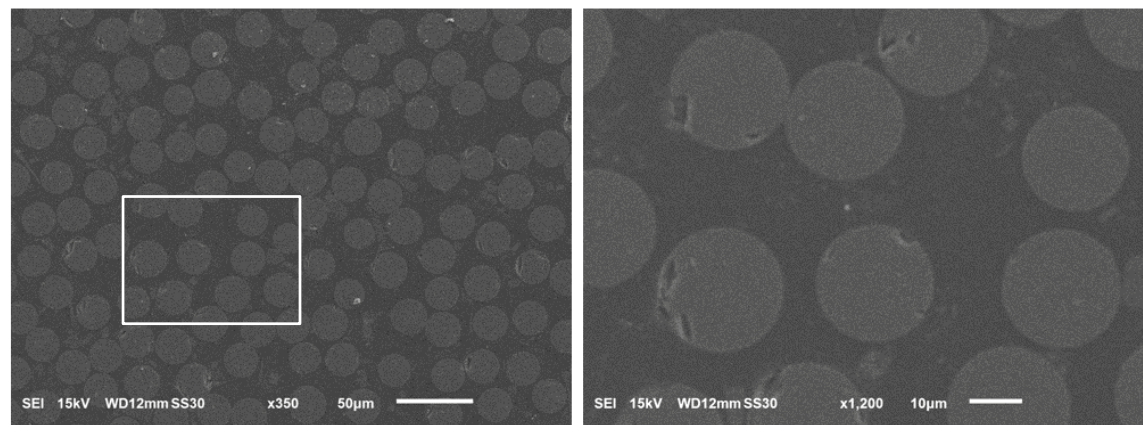


Figure 3.9: Area with no void of GFRP-C at magnification levels of 350x (left) and 1200x (right)

GFRP-D demonstrated disconnected void patterns in the cross-section including both at the central portion and edges (Figure 3.10). The number of voids reduced in the central part compared to the edges. Figure 3.11 provides higher magnification images of the voids and the no void area.

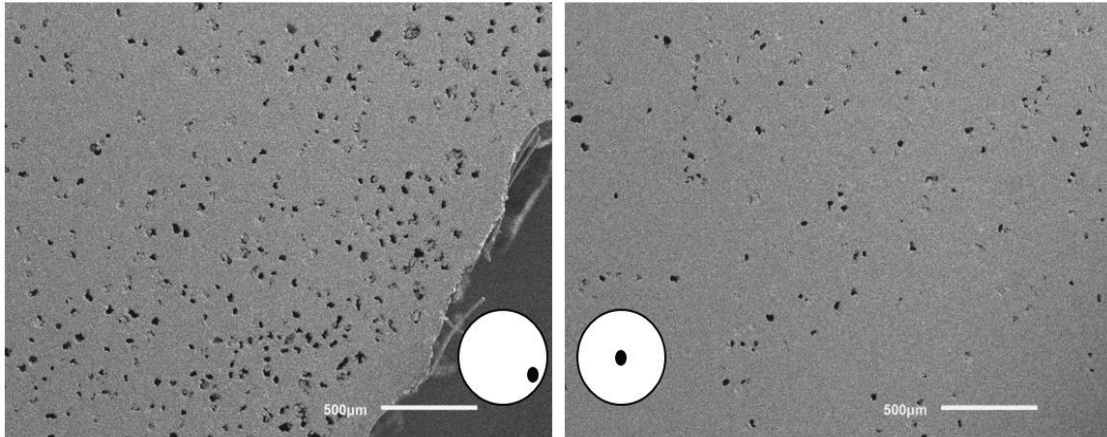


Figure 3.10: Disconnected void patterns at the edge (left) and at the center (right) of GFRP-D

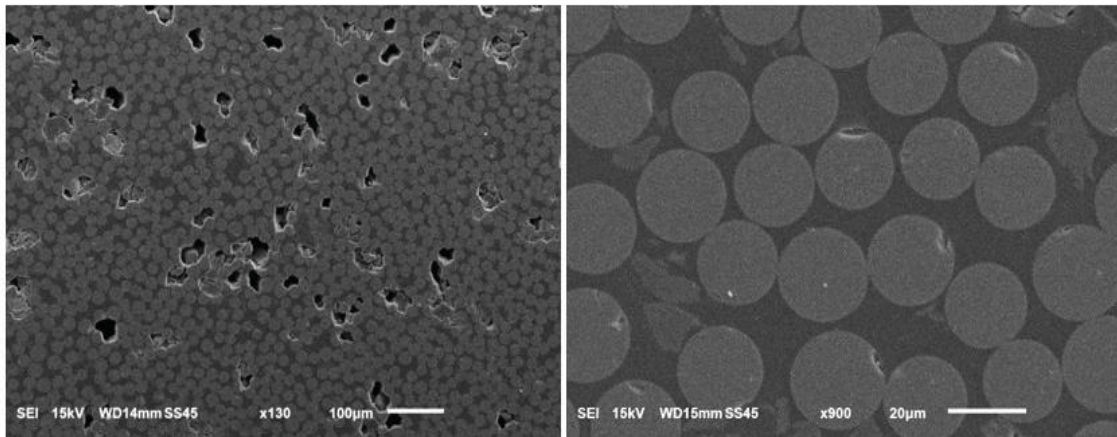


Figure 3.11: Higher magnification image of the area with voids (left) & area with no void (right) of GFRP-D

Finally, Figure 3.12 provides a panorama image of the entire section for all the GFRP bars. It serves as a proper comparison purpose and demonstrates that each bar had a unique microstructural pattern.

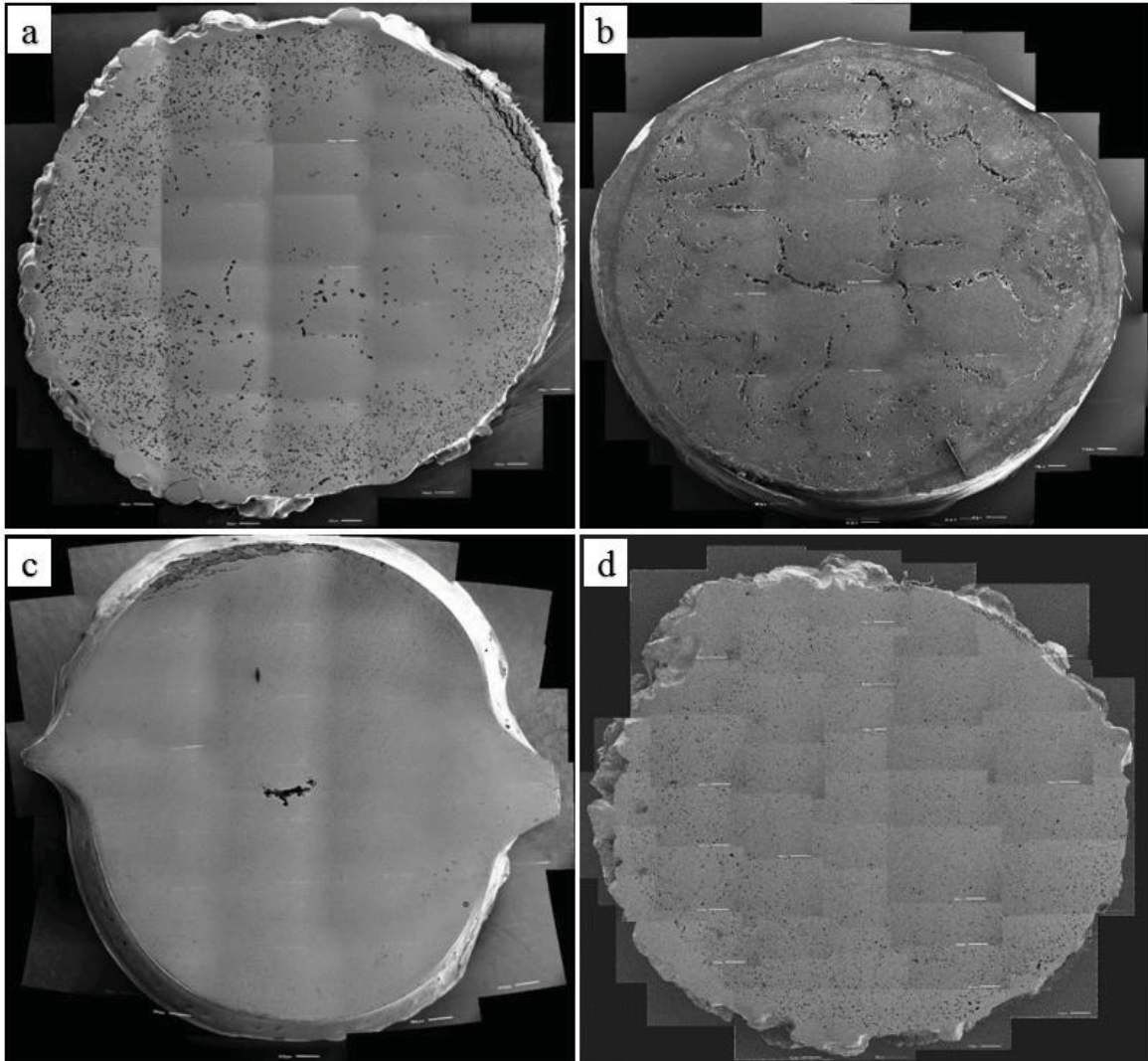


Figure 3.12: Panorama images of GFRP-A (a), GFRP-B (b), GFRP-C (c), and GFRP-D (d)

Alkaline Conditioning

GFRP-B and GFRP-C were exposed to the alkaline solution with the pH of 12.5-13 for a duration of 1000 hours. The alkaline solution was prepared following the ACI-440.3R by mixing 118.5 gr of $\text{Ca}(\text{OH})_2$, 0.9 gr of NaOH and 4.2 gr of KOH in 1 liter of deionized water [3]. A temperature of 60 °C (140 °F) was chosen to accelerate the exposure effect [56]. Five samples for each bar with the length of 0.5 m (19.7 in.) were placed in the environmental chamber. The GFRP ends were sealed with epoxy to reduce the effect of the moisture absorption through the ends. Next, the horizontal shear strength was determined

following the ASTM D4475 standard [57], since it provides mechanical properties at fiber-resin interface and is a useful parameter for quality control purposes. Five conditioned samples with the length of 50.8 mm (2.0 in.) were tested for each bar type. The same test repetition was performed on pristine samples. Figure 3.13 shows the difference of the pristine and conditioned GFRP bars.

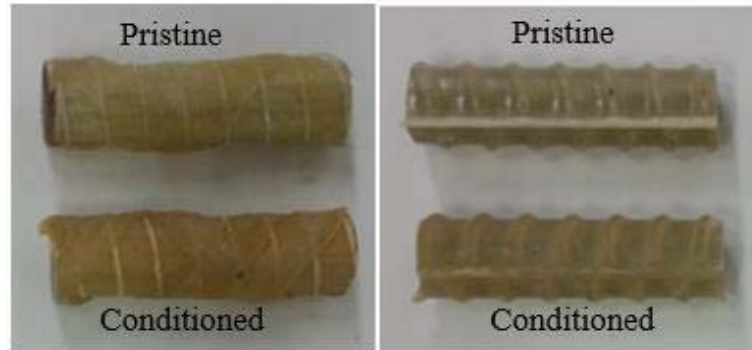


Figure 3.13: GFRP-B (left) and GFRP-C (right) samples used in the horizontal shear test

Test span was set as three times of the bar diameter following the standard. The load was applied in the displacement control mode at the rate of 1.27 mm/min (0.05 in./mm). The test Fixture is shown in Figure 3.14.

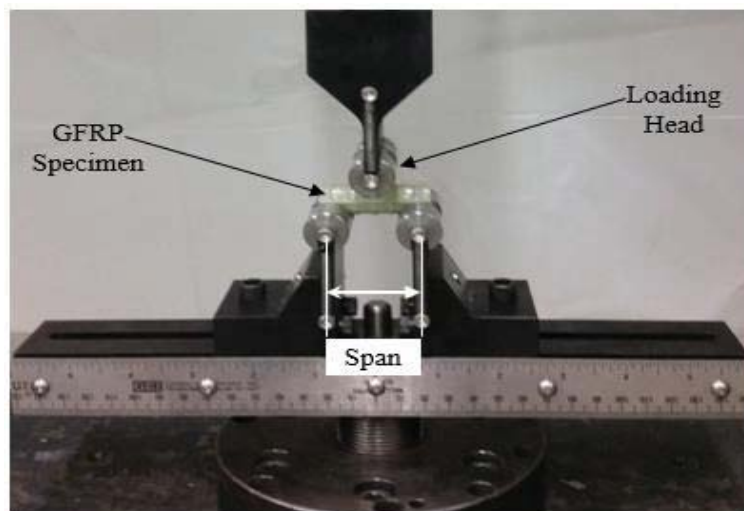


Figure 3.14: Horizontal shear test performed on GFRP bars

Table 3.2 reports the average results, where S_p refers to the horizontal shear strength of the pristine, and S_e refers to the horizontal shear strength of the exposed bars. The same

notation is used for the failure load (P). Based on the results, after 1000 hours of exposure to the alkaline solution at 60 °C, the horizontal shear strength of GFRP-C decreased only by 1% compared to the pristine values while GFRP-B exhibited a 15% reduction in the horizontal shear strength.

Table 3.2: Results of the horizontal shear test on pristine and conditioned GFRP samples

Type	P_p			P_e			S_p (MPa)	S_e (MPa)	Ratio (S_p/S_e)
	No. of Samples	Average (kN)	CoV (%)	No. of Samples	Average (kN)	Cov (%)			
GFRP-B	5	10.45	9.2	5	8.91	3.5	54.93	46.90	0.85
GFRP-C	5	12.19	12.2	5	12.07	4.0	64.16	63.55	0.99

Note: 1 kN= 0.2248 kip; 1 psi=0.0069 MPa

The results obtained from the horizontal shear test was consistent with the expectations from the SEM imaging. The entire cross-section of GFRP-B was covered with the connected and disconnected defect patterns and it was expected to affect the durability. GFRP-C was characterized with no connected or disconnected void/defect patterns and demonstrated a higher resistance to alkaline conditioning. Additional evidence was provided by performing the SEM imaging and the EDS analysis on the conditioned samples which investigated the change in the microstructure at the vicinity of the existing defect patterns. Figure 3.15 shows the conditioned and intact regions and the alkaline surface penetration in GFRP-C. Microstructure of GFRP-C did not include any existing defect/void pattern. As a result, no localized damage was observed and the alkaline surface was penetrating from the edge toward the core of the bar.

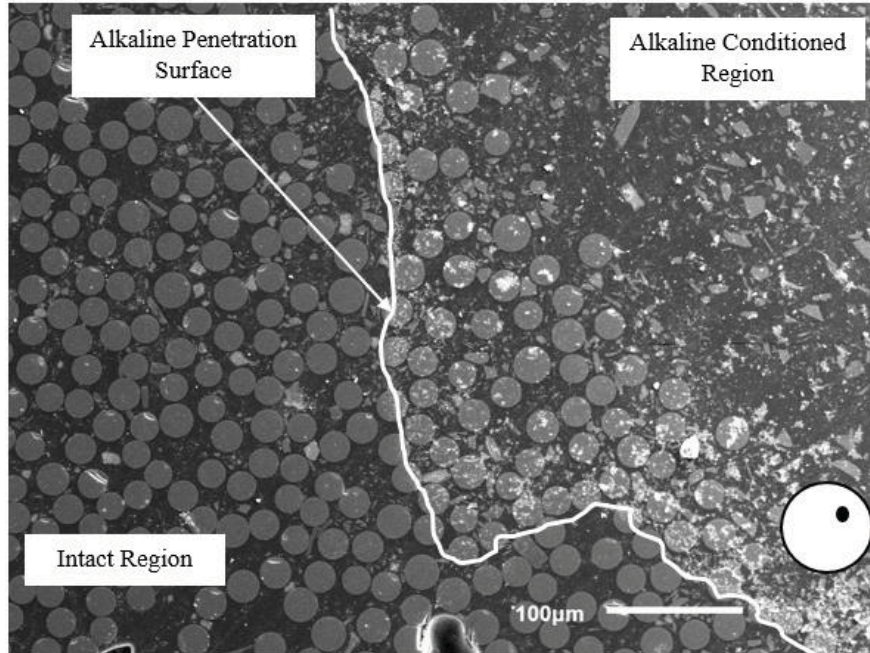


Figure 3.15: Conditioned and intact region in GFRP-C

SEM images of GFRP-B presented extensive damage in the vicinity of the existing defects. Figure 3.16 shows an alkaline conditioned region of GFRP-B demonstrating the damage in the resin and glass fibers. Additionally, Figure 3.17 presents excessive damage in the fibers at the vicinity of an existing defect. The damaged area was not clearly separated from the intact region. EDS analysis was performed and compared to the pristine bars to distinguish the existing chemical elements (Figures 3.18 and 3.19). Additionally, elemental scatter was provided to demonstrate the distribution of each element (Figure 3.20).

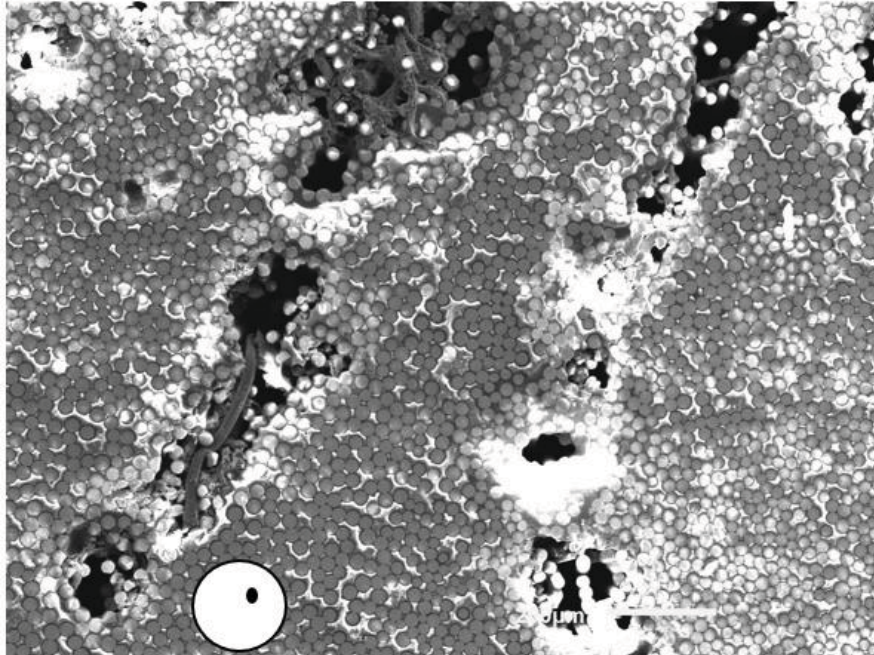


Figure 3.16: A conditioned region of GFRP-B presenting an extensive damage in the resin and glass fibers

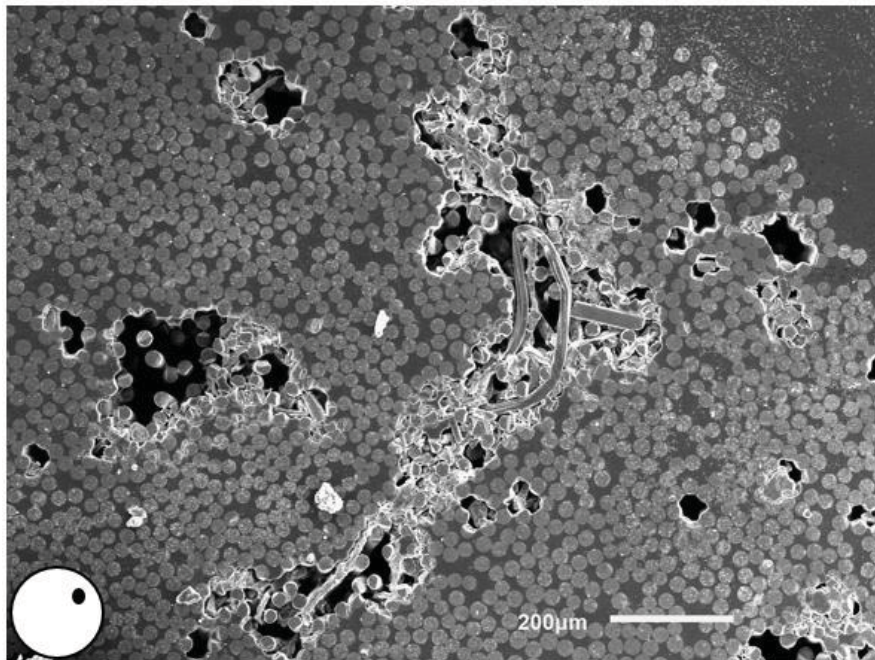


Figure 3.17: A conditioned region of GFRP-B presenting an extensive damage in the fibers at the vicinity of an existing defects

Na and Cl were detected at the entire monitored area of the conditioned sample. Si, Ca, Al and Mg were mainly detected in the fibers.

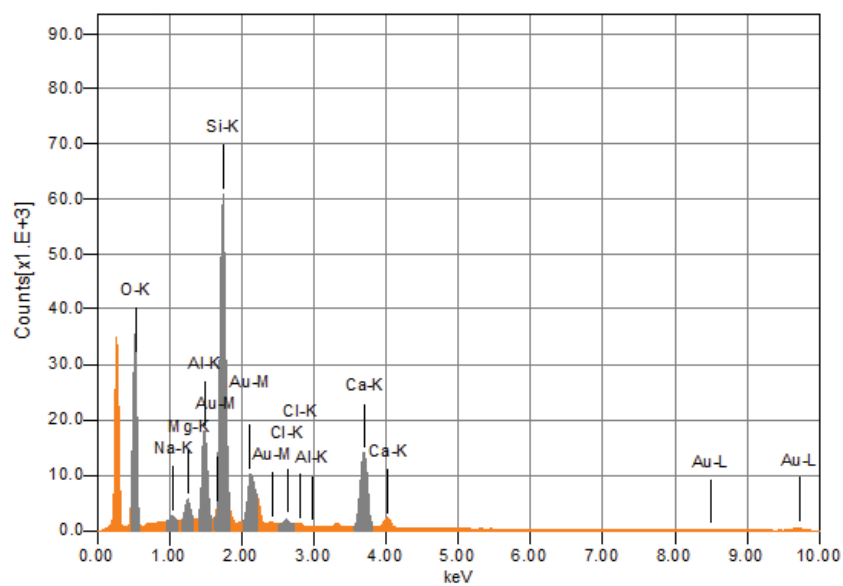


Figure 3.18: Result of the EDS analysis performed at the edge of GFRP-B after accelerated conditioning

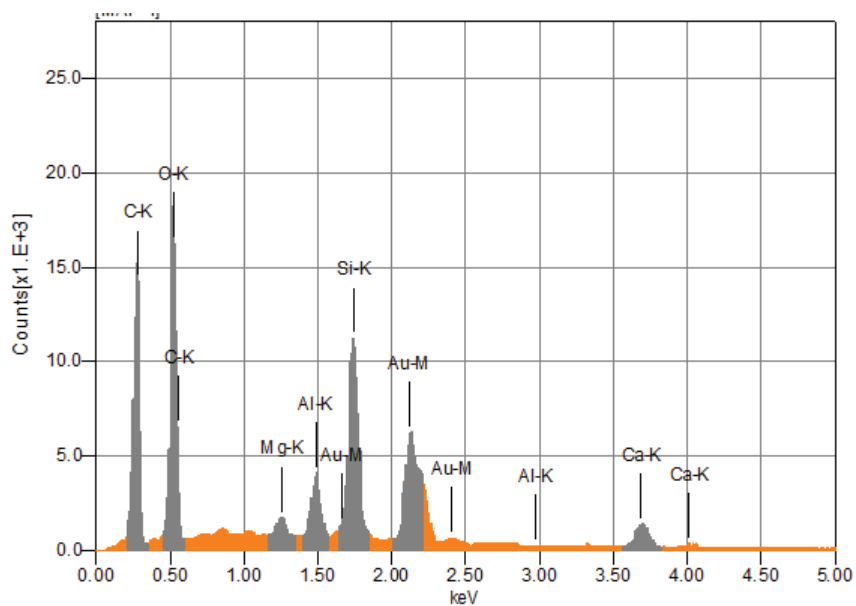


Figure 3.19: Result of the EDS analysis performed on pristine GFRP-B bar

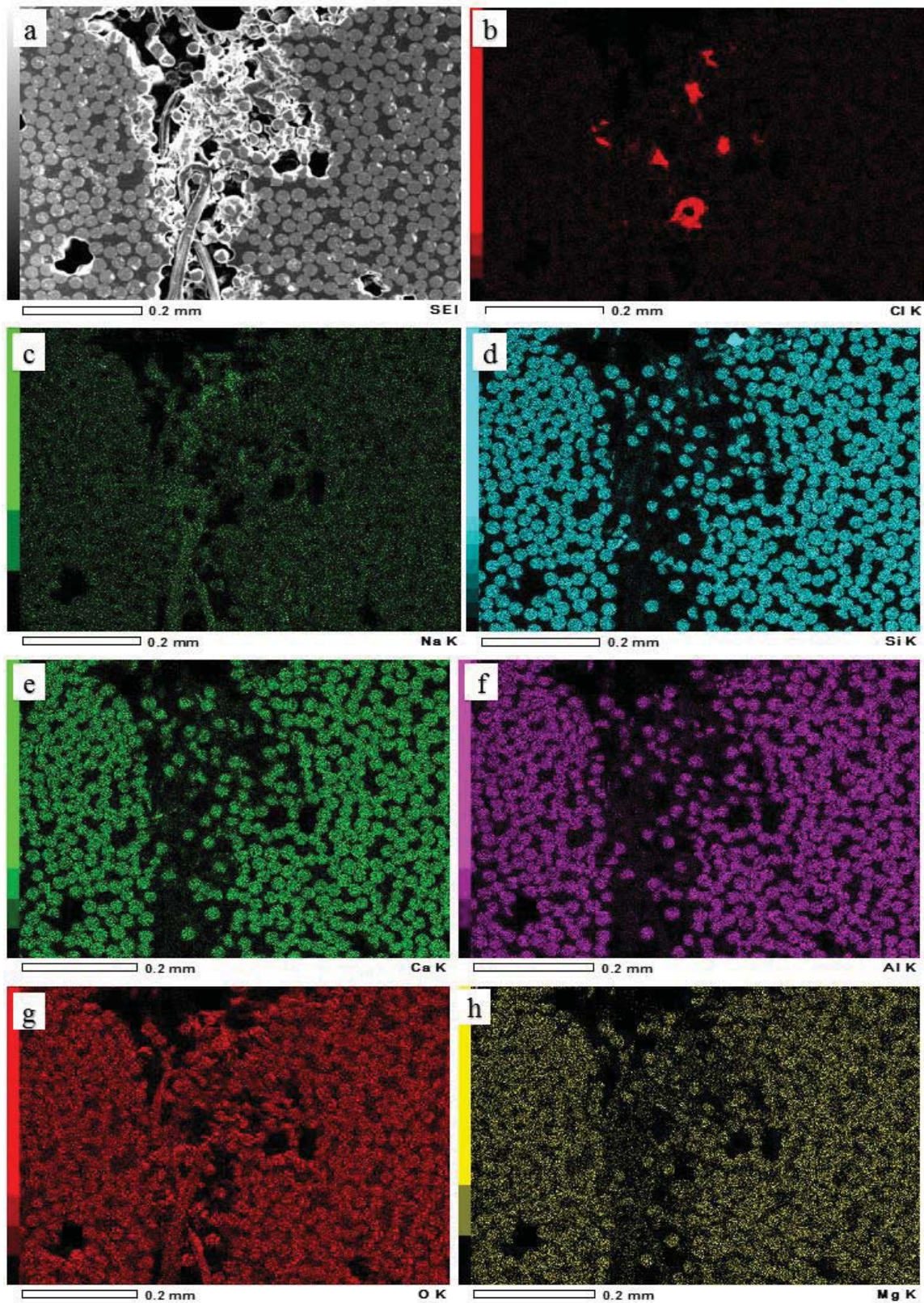


Figure 3.20: Elemental scatter of GFRP-B after exposure to alkaline solution: SEM image of GFRP-B (a) and elemental distributions of: Cl (b), Na (c), Si (d), Ca (e), Al (f), O (g), and Mg (h)

Concluding Remarks

Scanning electron microscopy was performed at different magnification levels on four different commercially available GFRP bars. Each bar presented a unique microstructural pattern due to the different manufacturing process. The effect of these patterns on GFRP durability was investigated by conditioning two of the bars in alkaline solution. Horizontal shear tests were performed as a proper indication of durability. SEM and EDS analysis were performed on the conditioned samples to provide additional data points. According to the results from the SEM imaging, the following conclusions are made:

- Each GFRP bar demonstrated a unique signature of the existing defect/void pattern characterized by a combination of disconnected and continuous voids at different locations of the cross-section due to the different manufacturing process.
- GFRP-A demonstrated both disconnected voids mostly at the vicinity of the edges as well as the defects along the edges of the bar. GFRP-B showed the most voids/defects in the cross-section compared to the other GFRP bar types. It mostly included connected voids at the entire area. GFRP-C presented the lowest existing void/defect compared to the other GFRP bar types. There was a single void in the center of the bar and a macro-defect at the edge. GFRP-D presented disconnected voids all over the cross section while there were fewer voids at the center of the bar compared to the edges.
- After 1000 hours of exposure to the accelerated conditioning in a high pH alkaline environment at 60 °C (140 °F), GFRP-C did not lose the horizontal shear strength (less than one 1%) while GFRP-B demonstrated 15% loss of this property.

- SEM imaging and EDS analysis were performed on the conditioned bars. GFRP bars with different microstructural patterns displayed differences in the penetration of the alkaline front. Extensive damage was observed at the vicinity of existing defects/voids.
- GFRP microstructural pattern plays a critical role in the mechanical properties and durability of GFRP bars while it may not be the only effective parameter.
- The results of this study can be used as a benchmark for microstructure of commercially available pristine GFRP bars and serve as a base for monitoring possible changes after conditioning or field use.

Future Research

Additional tests need to be conducted to provide more evidence on the effect of GFRP microstructural patterns on its long-term behavior. Documents can be developed to emphasize the importance of microstructural pattern as a signature of each GFRP due to different manufacturing processes. It should be suggested to GFRP manufacturers to investigate the quality of their products using SEM imaging.

Chapter 4-GFRP Post-Fire Behavior

Fire represents one of the most severe conditions experienced during the service life of a structure. Structures should maintain their load bearing capacity within an adequate time to preserve life safety. It is critical to consider the fire safety in structural design to ensure the structural integrity and stability and to minimize the global and localized structural damages [58-59].

A real fire consists of four fundamental stages as shown in Figure 4.1. The first stage is the incipient ignition phase where the available fuels are heated. In the growth stage, the visible flaming combustion occurs. Next the fire develops accompanied by the increase of temperature. When the temperature reaches the flashover point, the burning period starts which consists of high temperature and is the most severe stage of the fire. Finally, the available fuel starts exhausting and the fire dies out gradually in the decay stage [60].

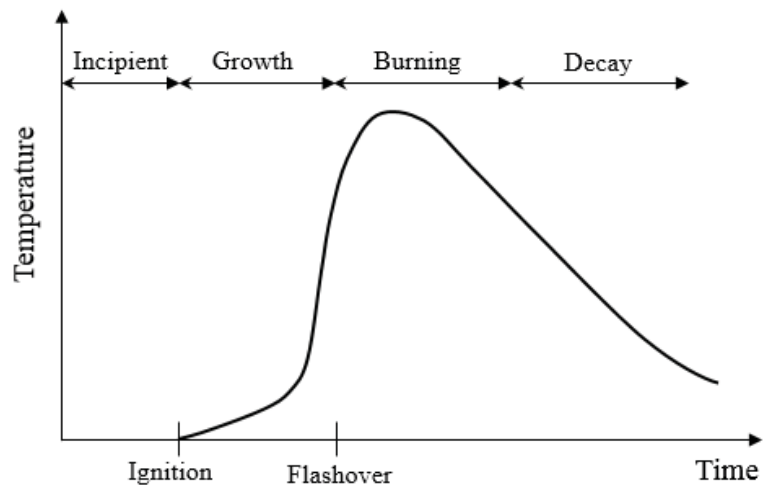


Figure 4.1: Different stages of a real fire

Several standard test methods have been provided to validate the fire resistance of a structure such as ASTM E119 and ASTM E1529 [61-62]. These methods usually expose

the structural members to predefined time dependent temperature curves using gas furnace or any other thermal sources. ASTM E119 has been the traditional standard for testing fire resistance of the structures in the US since 1918 and is applicable to the individual structural members such as beams, slabs, columns, floors and walls of any material [60]. It consists of a temperature-time curve which reaches the equivalent temperature of 538 °C (1000 °F) in almost 5 minutes. Figure 4.2 compares the temperature-time profiles of ASTM E119 standard with a real fire.

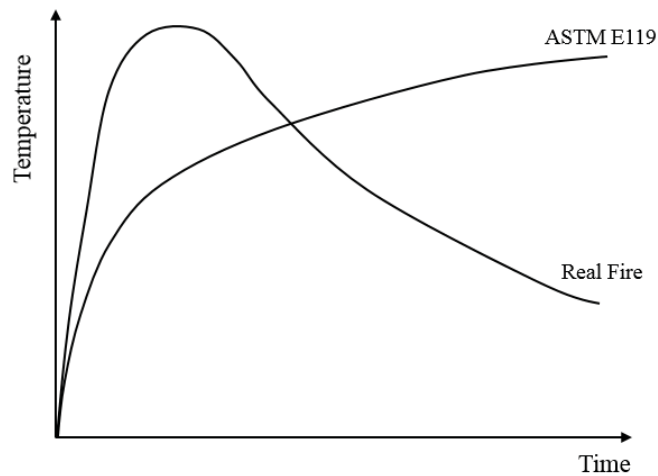


Figure 4.2: Schematic temperature-time curves of the ASTM E119 standard and the real fire [58]

As shown in Figure 4.2, the ASTM E119 standard is not the perfect representative of the fire scenario. It consists of an ever-increasing profile ignoring the decay stage of the real fire. The standard fire test only simulates the most severe burning stage of the real fire. Additionally, it does not represent a realistic rate of the temperature increase and may not be applicable for the severe fire scenarios. In these cases, a different fire standard (ASTM E1529) is recommended in which the temperature reaches the equivalent of 1093 °C (2000 °F) in 5 min. In addition, several parameters such as the type of combustible material, ventilation, heat release, smoke generation/propagation are not considered in the standard

fire tests. Standard fire tests also focus on the behavior of single members due to the practical possibility of testing only a few members simultaneously inside the furnace. In a real structure, forces in the failing members can be transferred to the other undamaged members. Despite all their limitations compared to the real fire, standard fire tests are useful comparative tools to test the relative fire resistance of structural members.

Fire safety is even more important for the structures incorporating GFRP materials compared to the conventional steel reinforced structures since the elevated temperature may cause severe deterioration of the GFRP mechanical and bond properties. Adequate fire resistance of GFRP-RC elements is still a fundamental design requirement to ensure structural integrity for a sufficient period of time [63-66].

There is a lack of reliable data on the behavior of GFRP-RC elements exposed to fire. Moreover, there is no proper structural design code for the fire exposure of the structures incorporating FRP materials, except the Canadian code [67] that provides a design procedure based on a study by Kodur and Baingo [68]. Further experimental studies and advance numerical models are required to provide more confidence in using GFRP materials in the structures with the possible fire scenario. Updating the existing building codes and providing suggestions should be one of the aims of these studies [69]. In the case of steel, the design for fire resistance is based on avoiding a threshold temperature defined as the temperature in which the bar retains only 50% of the original tensile strength. In North America, this temperature corresponds to 593 °C (1099 °F) [63-64, 69]. This criterion may not be applicable to GFRP due to different design procedure of the GFRP-RC structures [69-70]. Additionally, while the material property of the steel at elevated temperature is well studied, additional research is required for the GFRP bars. In particular,

limited information is available on changes in the structural and material properties after fire exposure and on the post-fire residual strength of the GFRP-RC materials [64].

The purpose of the first part of this study was to evaluate the residual mechanical properties of the GFRP bars extracted from the fire exposed GFRP-RC slabs. To this end, one-way slabs reinforced with two types of commercially available GFRP bars were studied by exposing the slabs to a simultaneous service load and standard fire temperature profile of ASTM E119 standard. Concrete samples and GFRP bar segments were extracted after the tests to evaluate the residual mechanical properties, i) transverse shear strength; ii) horizontal shear strength; iii) transition glass temperature (T_g) since beyond this temperature, the bond of the concrete to the bar decreases significantly due to resin softening [71]; iv) microstructural investigation using the SEM imaging to monitor possible microstructural degradation in the GFRP bars or loss of interfacial bond between GFRP and concrete.

In the second part of this study, a thermomechanical FEM model was developed in Abaqus to find the temperature distribution and to investigate the thermal loading on the GFRP-RC structures and concrete cracking.

Important Factors in GFRP Fire Behavior

Various parameters contribute to the fire behavior of GFRP-RC members such as resin transition glass temperature (T_g), concrete cover, unexposed zone of the reinforcement and aggregate type. The effect of each parameter is explained briefly.

T_g : The resin plays a critical role in transferring and distributing the load among the fibers. Above a certain temperature called transition glass temperature, the resin softens, changing from a hard glass to a soft rubber-like state. T_g is usually in the range of 65-120

°C (150 °F-248 °F) for GFRP bars [3]. After the bar temperature reaches the T_g , the resin loses the ability to transfer the load and the interfacial bond to concrete reduces. The GFRP material properties start degrading even before T_g , but dramatic changes occur after this temperature [72].

Concrete cover: Concrete acts as a thermal insulator for the GFRP bars due to its low thermal conductivity and high heat capacity resulting from chemical properties of its constituents (cement and aggregates). The slow rate of heat transfer makes the concrete an effective fire insulator. Proper concrete cover (the distance between the concrete surface and edge of reinforcement) can help keeping the temperature of the internal reinforcement below the critical temperature for a desired time period. Different required minimum concrete cover values, ranging between 30-70 mm (1.18-2.75 in.), have been reported to ensure the structural safety of GFRP-RC members [73-74].

Unexposed zone: Unexposed zone of the GFRP bars increases the load-carrying capacity of the structure by avoiding the pull-out of the bar and shifting the failure mode to bar rupture while an inadequate anchorage length leads to slippage of the reinforcement due to the bond reduction.

Aggregate type: Carbonate based aggregates lead to higher thermal resistance compared to the silica based aggregates due to their higher thermal capacity [75].

Concrete cracking: Cracking may cause the heat flow to penetrate in the structure and provide significant localized damage in the reinforcement [65].

Specimen Configuration

Two GFRP bars with equivalent size and distinct surface characteristics were selected in this study named as GFRP-A and GFRP-C (similar to the ones used in chapter 2),

corresponding to a fine sand coated with helically wrapped fibers (GFRP-A) and ribbed deformed surface similar to the steel rebars (GFRP-C).

GFRP-RC slabs were designed with a single GFRP bar located at the center with 19 mm (0.75 in.) of the clear concrete cover corresponding to minimum cover for the design requirements. All the slabs were monolithically cast from a single concrete batch of normal weight concrete consisting of type I cement with a maximum aggregate size of 6.4 mm (0.25 in.). Average 28-day compressive concrete strength of 42.3 MPa (6135 psi) was obtained according to the ASTM C39 [35]. Figure 4.3 illustrates the slab geometry and location of the GFRP reinforcement and the load configuration used during fire test.

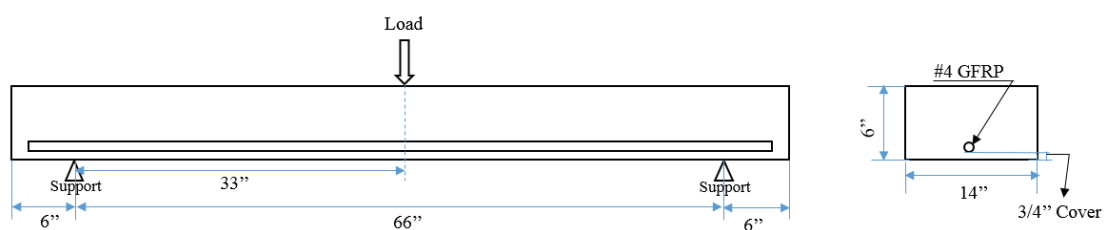


Figure 4.3: Schematic of GFRP-RC slabs (Note: 1 in.=25.4 mm)

The slabs were designed so that the failure was controlled by the failure of the GFRP bars (under reinforced). Internal type-K thermocouples were installed on the GFRP bar and different depths of the concrete to measure the temperature during the fire test.

Fire Exposure

GFRP-RC slabs were placed side by side vertically at the furnace opening, with the flexural face of the slabs facing the furnace, held on a steel frame providing simple support conditions and tested simultaneously for two hours per ASTM E119. The gap between the slabs and the steel frame was filled with the fire resistant insulation materials to minimize the heat lost. A rigid deep steel spreader beam was used to distribute the load from

hydraulic jack to each slab independently providing a service point load (P_{ser}) of 5.78 kN (1300 lbs) [51] at the mid-span per slab (Figure 4.4).



Figure 4.4: GFRP-RC slabs facing the vertical furnace

The ASTM E119 standard furnace temperature-time profile is approximate as [61]:

$$T = 750 \left[1 - e^{-3.79553\sqrt{t}} \right] + 170.41\sqrt{t} + T_0 \quad (4.1)$$

where t refers to time (hours), T corresponds to the temperature in $^{\circ}\text{C}$, T_0 corresponds to the ambient temperature.

The actual furnace temperature was measured during the test using the average value of the temperature readings from nine shielded furnace thermocouples evenly distributed inside the furnace (Figure 4.5).

The maximum temperature of 115°C (240°F) was recorded at the mid-plane of GFRP reinforcement. Due to low thermal conductivity of the GFRP bars, the lower and upper faces of the bar experienced significantly different temperatures [69]. In addition, it was also inferred that at 76 mm (3 in.) from the exposed face, the temperature within the

concrete slabs was not affected due to high thermal insulation properties of the concrete as presented in Figure 4.6 [76].

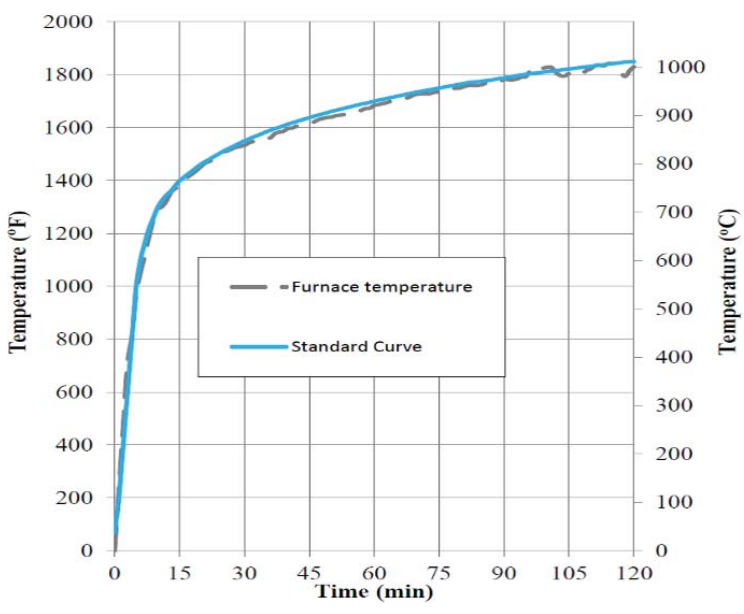


Figure 4.5: Temperature-time profile of the furnace

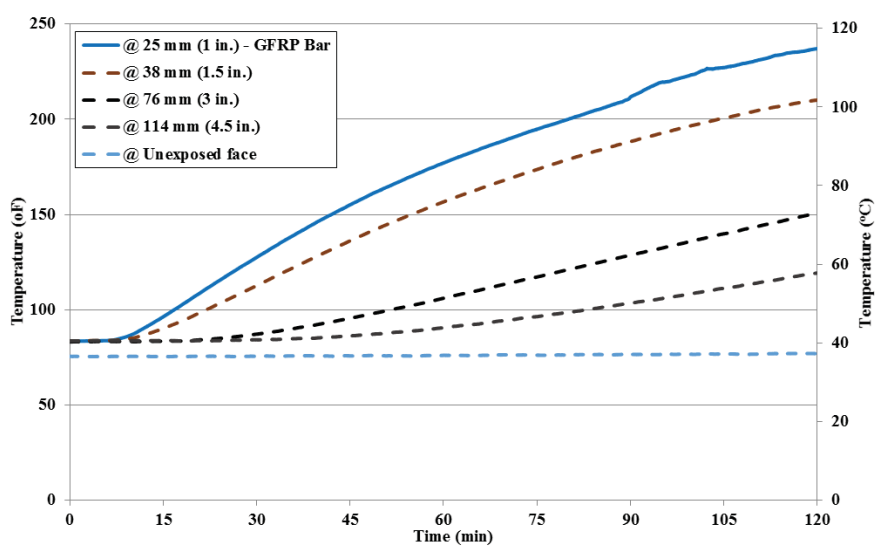


Figure 4.6: Temperature gradient in a representative fire exposed GFRP-RC slab

Multiple concrete samples and GFRP bar segments were extracted after the cooling phase from different location along the reinforcement to provide proper repetition for each test (Figure 4.7)

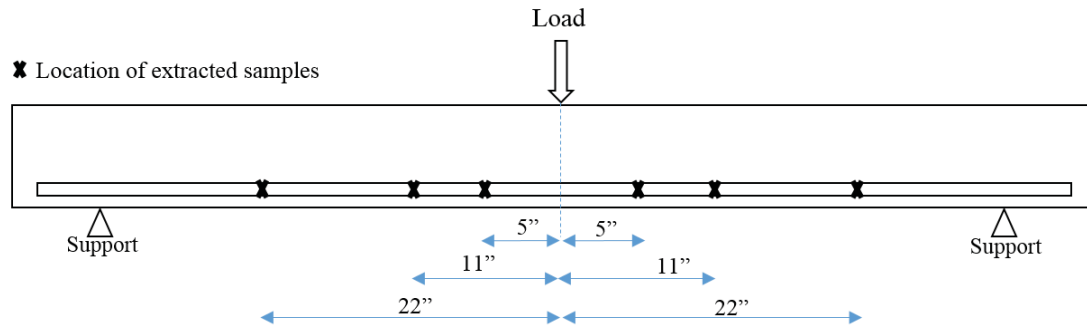


Figure 4.7: Location of the extracted samples along the GFRP bar after fire exposure

Residual Mechanical Properties of the GFRP Bars

Transverse Shear Strength

The transverse shear strength of extracted GFRP bars from slabs exposed to the furnace fire was determined according to the ASTM D7617 standard [77]. This parameter was used since it provides an overall mechanical performance of the composite rebar system. Three 228.6 mm (9 in) long samples per GFRP bar type were tested using a screw-driven test frame with the capacity of 150 N (30 kips) shown in Figure 4.8. The load was applied at the rate of 1.27 mm/min (0.05 in./mm).



Figure 4.8: GFRP bars tested in transverse shear fixture

The results were compared with pristine samples for each bar type. Table 3.1 presents the summary of the average results and coefficient of variance (COV), where τ_P^T refers to the average transverse shear strength of the pristine bars, and τ_F^T corresponds to the average transverse shear strength of the fire exposed samples.

Overall, GFRP-A and GFRP-C experienced a 5% and 11% of reduction in shear strength, respectively. In both cases, the transverse shear strength was always higher than the minimum accepted value of 152 MPa (22 ksi) [6]. After 120 minutes of furnace fire exposure, the transverse shear strength of the bars was not affected significantly, maintaining an acceptable level of the residual strength compared to the pristine bars. GFRP-C experienced a higher reduction of shear strength compared to GFRP-A.

Table 4.1: Average results of the transverse shear tests on fire exposed GFRP bars

Bar Type	τ_P^T			τ_F^T			Ratio (τ_F^T / τ_P^T)
	Sample number	Average (MPa)	Cov (%)	Sample number	Average (MPa)	Cov (%)	
GFRP-A	5	167.40	3.4	3	158.78	2.5	0.95
GFRP-C	5	194.36	4.6	3	173.40	4.4	0.89

Note: 1 MPa= 0.145 ksi

Horizontal Shear Strength

The horizontal shear strength was determined following the ASTM D4475 standard [57]. This parameter provides the mechanical properties of fiber-resin interface and is a useful parameter for the quality control purposes. The test span was set as three times of bar diameter following the standard. Three samples of each fire exposed slab and five samples of pristine GFRP bars were tested for each bar type (Figure 3.14). Samples were 50.8 mm (2 in.) long. Loading was applied at a rate of 1.27 mm/min (0.05 in./mm).

Table 4.2 reports the average results, where τ^{H_P} refers to the horizontal shear strength of the pristine, and τ^{H_F} refers to the horizontal shear strength of the fire exposed bars. Based on the results, after 120-minutes of fire exposure, the horizontal shear strength of both GFRP bars increased by 15% and 7% for GFRP-A and GFRP-C, respectively. The furnace fire may have post-cured the resin and resulted in the increase of horizontal shear strength. GFRP-A presented a higher increase in horizontal shear strength compared to GFRP-C. Currently, no values have been suggested for the minimum requirements of the GFRP horizontal shear strength. Post-curing of the resin did not result in increase of transverse shear strength since it is mainly dominated by the property of the fibers.

Table 4.2: Average results of the horizontal shear tests performed on the fire exposed GFRP bars

Bar Type	τ^{H_P}			τ^{H_F}			Ratio (τ^{H_F} / τ^{H_P})
	Sample number	Average (MPa)	Cov (%)	Sample number	Average (MPa)	Cov (%)	
GFRP-A	5	49.02	2.5	3	56.67	4.9	1.15
GFRP-C	5	62.53	5.7	3	67.02	1.1	1.07

Note: 1 Mpa= 0.145 ksi

Transition Glass Temperature (T_g)

Transition glass temperature (T_g) of the bars were measured by performing the dynamic mechanical analysis (DMA) tests on three specimens for each bar type and the results were compared with the pristine bars.

The T_g generally varies from rebar to rebar due to the manufacturing process and curing protocol and is desired to be higher than 100°C (212°F) [6]. The rectangular specimens of 1×5×50mm (0.04×0.2×2.0 in.) were extracted from the bars according to ASTM E1640 standard [78]. The DMA test was performed with a three-point-bending fixture as shown in Figure 4.9 for the temperature range of 35-150°C (95-302°F), and a heating rate of

1°C/min (1.8°F/min). Table 4.3 shows the summary of the average results, where T_g^F refers to transition glass temperature of the fire exposed bars and T_g^P corresponds to the transition glass temperature of the pristine GFRP bars.

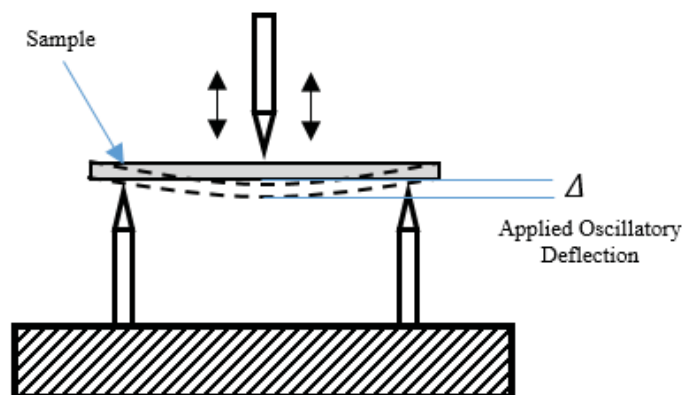


Figure 4.9: DMA test performed in 3-point bending configuration

Table 4.3: Average T_g test results performed on fire exposed GFRP bars

Bar Type	T_g^P			T_g^F			Ratio (T_g^F/T_g^P)
	Sample number	Average (°C)	Cov (%)	Sample number	Average (°C)	Cov (%)	
GFRP-A	3	81.1	16.6	3	119.3	5.9	1.47
GFRP-C	3	107.0	7.9	3	133.5	1.9	1.25

Note: °F=1.8 °C+32

The T_g increased by 47% and 25% after the fire exposure for GFRP-A and GFRP-C, respectively. The fire exposure resulted in increasing the temperature of the bars (Figure 4.6) and accordingly to post-curing of the resin. As a result, the T_g of the bars increased to values consistent with the experienced temperature during the heat exposure. Excessive exposure to heat may over-cure the resin and degrade the mechanical properties.

Figure 4.10 and Figure 4.11 show the analysis output of the DMA test and computation of T_g for pristine and fire-exposed GFRP-A samples, respectively. In the similar manner,

Figure 4.12 and Figure 4.13 represent the DMA analysis output for GFRP-C samples. The increase in T_g is evident in related diagram for both GFRP bars.

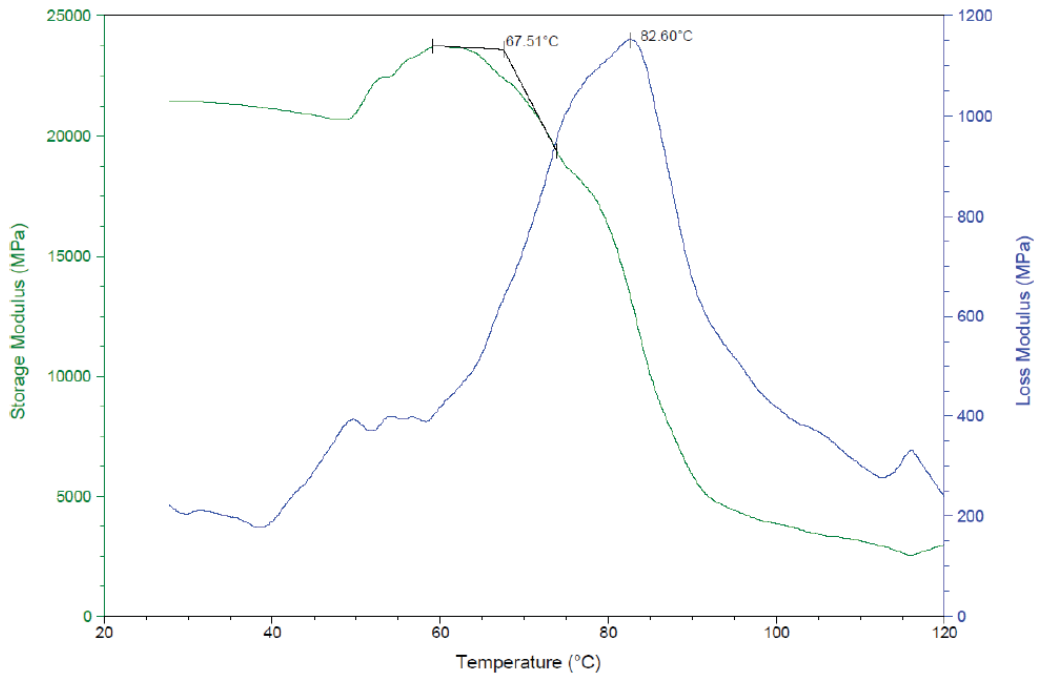


Figure 4.10: Output of DMA test performed on a pristine GFRP-A sample

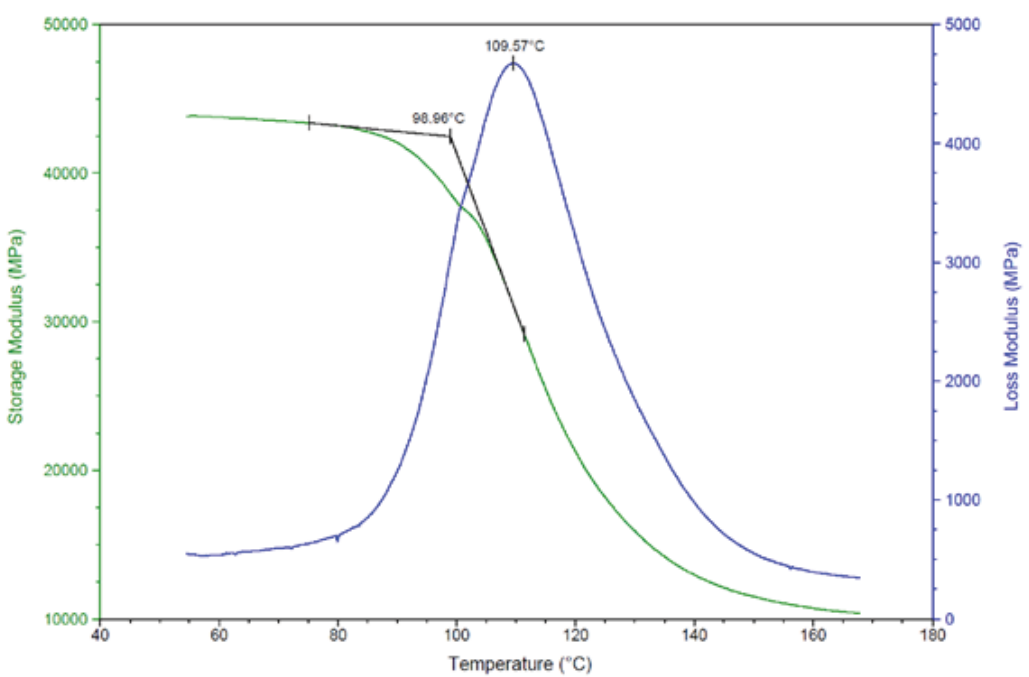


Figure 4.11: Output of DMA test performed on a fire-exposed GFRP-A sample

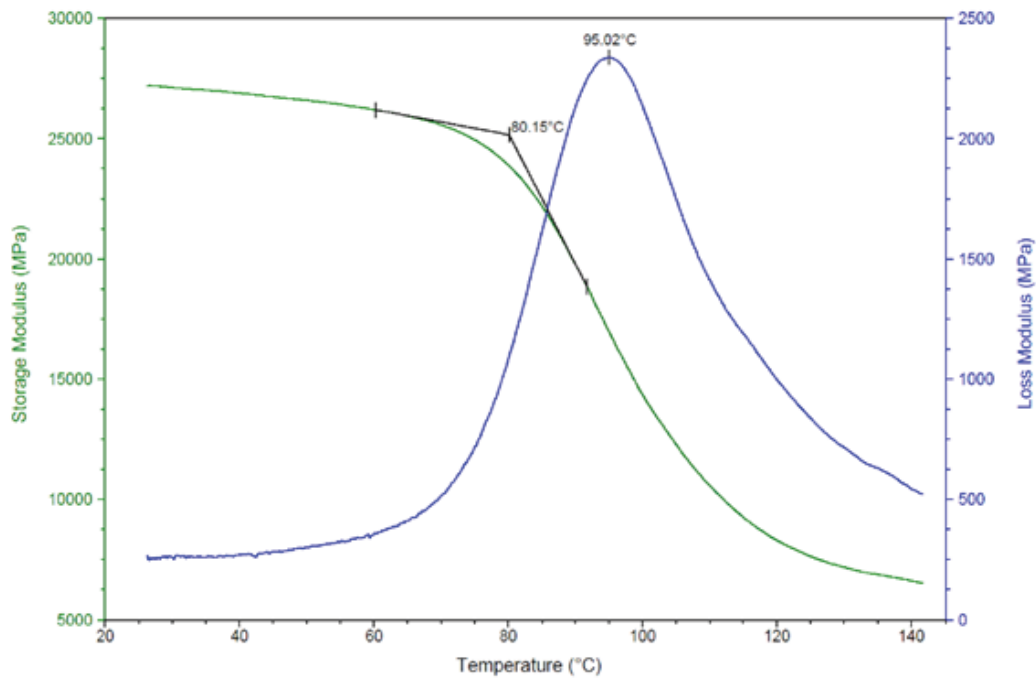


Figure 4.12: Output of DMA test performed on a pristine GFRP-C sample

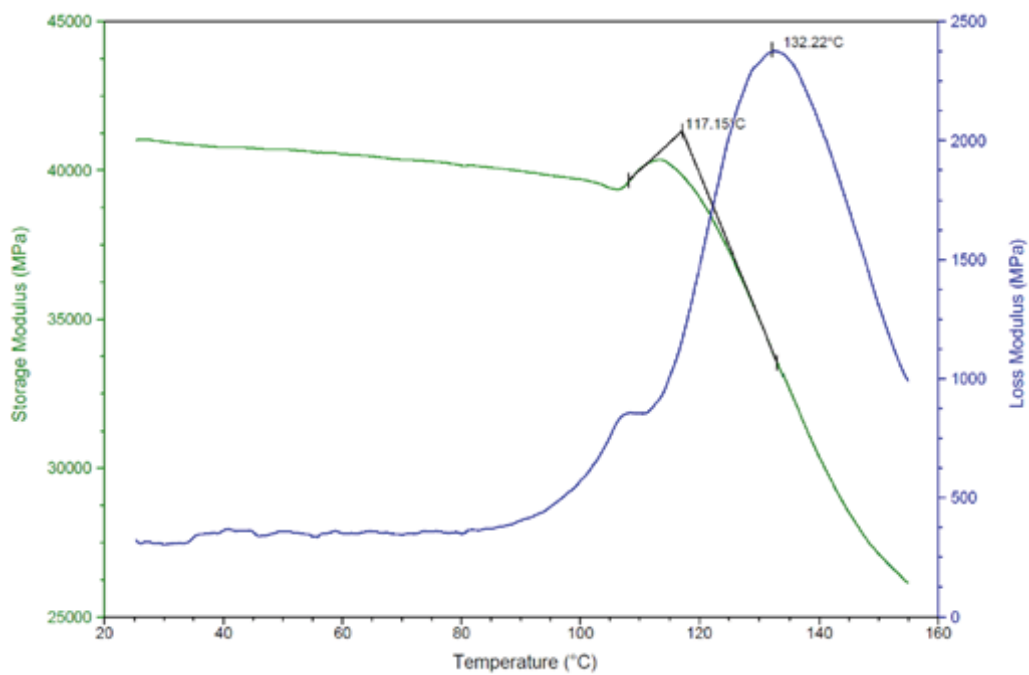


Figure 4.13: Output of DMA test performed on a fire-exposed GFRP-C sample

Microstructural Investigation

In addition to the mechanical tests, SEM analysis was performed on extracted GFRP samples to investigate the effect of fire exposure on the microstructure of GFRP bars. Microscopic examination allows monitoring possible damages at the single fiber scale by capturing the possible deteriorations in the fibers, matrix or concrete-GFRP interface. The extracted fire exposed GFRP samples were cut in approximate thickness of 7mm (0.27 in.). Concrete samples were also cut to monitor the GFRP-concrete interface. The specimen surfaces were prepared by sanding using different grit levels (i.e. 180, 300, 600 and 1200) of sand paper and employing dedicated grinding and polishing equipment. A fine polishing completed the specimen preparation using a wet-polishing agent and the polycrystalline diamond paste. Specimens were placed in an oven at 60°C (140 °F) for 24 hours to remove moisture produced during polishing procedure. Since GFRP bars are non-conductive materials, an ion sputtering device was used to coat the samples with gold prior to the SEM examination (Figure 4.14). Imaging was performed at different magnification levels (Figure 4.15-16).



Figure 4.14: GFRP samples prior to SEM imaging: GFRP-A (left) and GFRP-C (right)

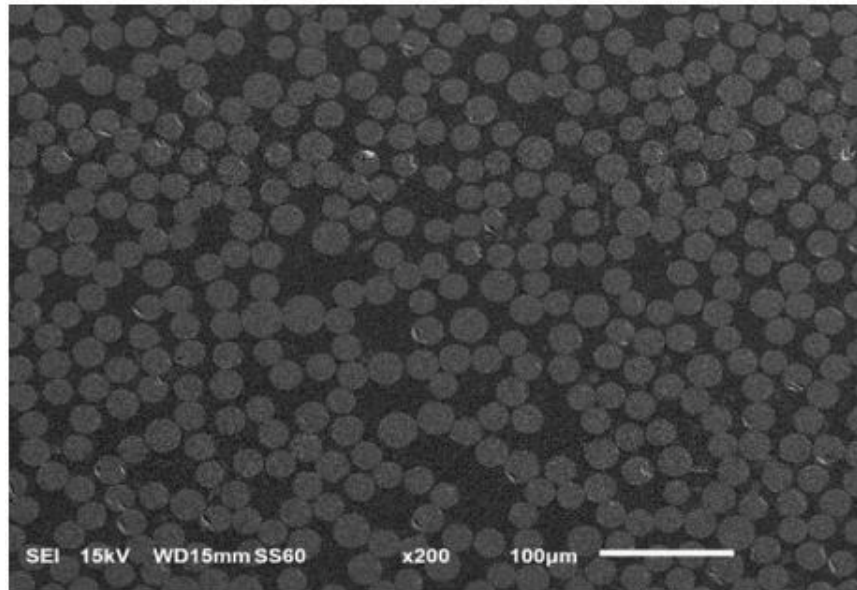


Figure 4.15: SEM image of the GFRP-A after fire exposure at the magnification level of 200x

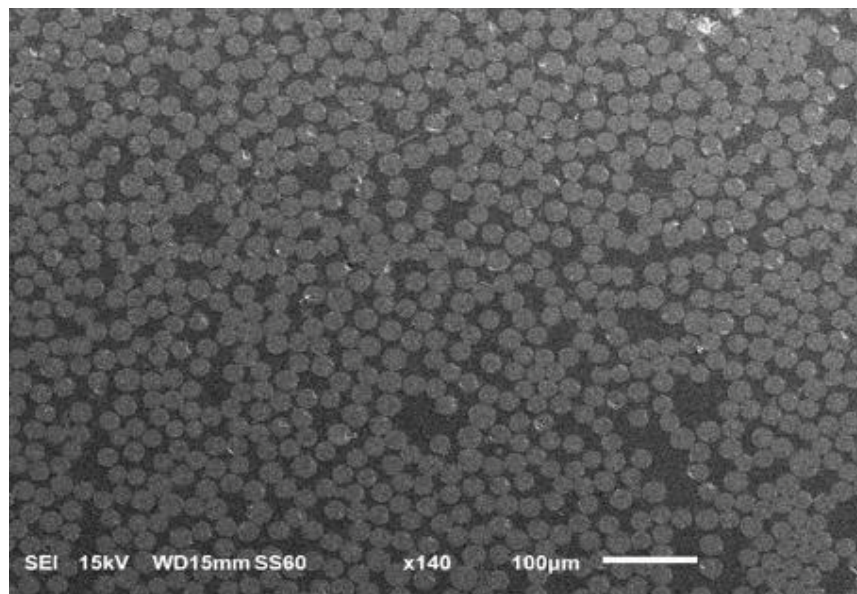


Figure 4.16: SEM image of GFRP-C after fire exposure at the magnification level of 140x

After monitoring the entire cross-section of several specimens, GFRP samples did not show any microstructure degradation after fire exposure and no damage was observed in the matrix nor in the resin-fiber interfaces. The SEM images of fire exposed GFRP bars are identical to the pristine (unexposed) samples presented in chapter 3.

Since, bond degradation between the concrete and reinforcement plays a critical role in fire behavior of the structure, concrete-GFRP interface were also examined (Figure 4.17-18). No apparent damage, degradation or loss of bond was observed. Additionally, the resin-rich region close to the edge of the bars were intact.

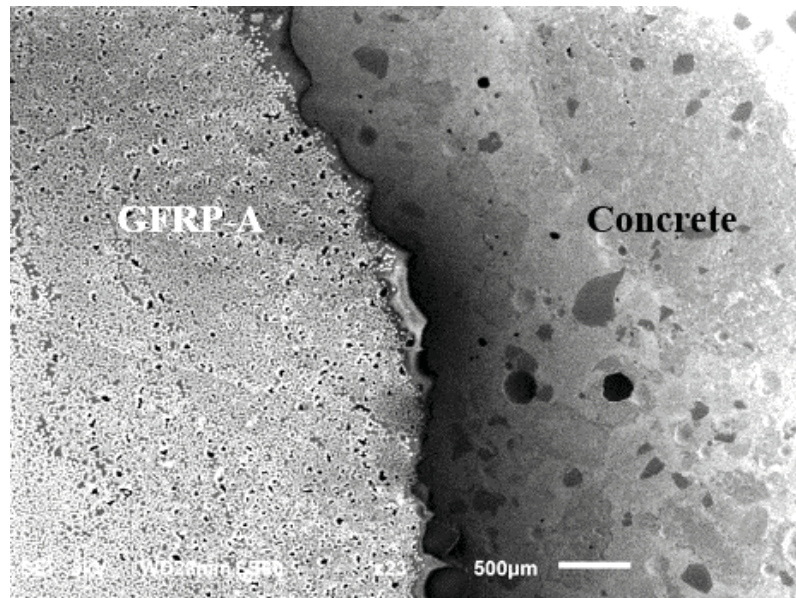


Figure 4.17: SEM image of the concrete to GFRP-A interface after fire exposure at the magnification level of 23x

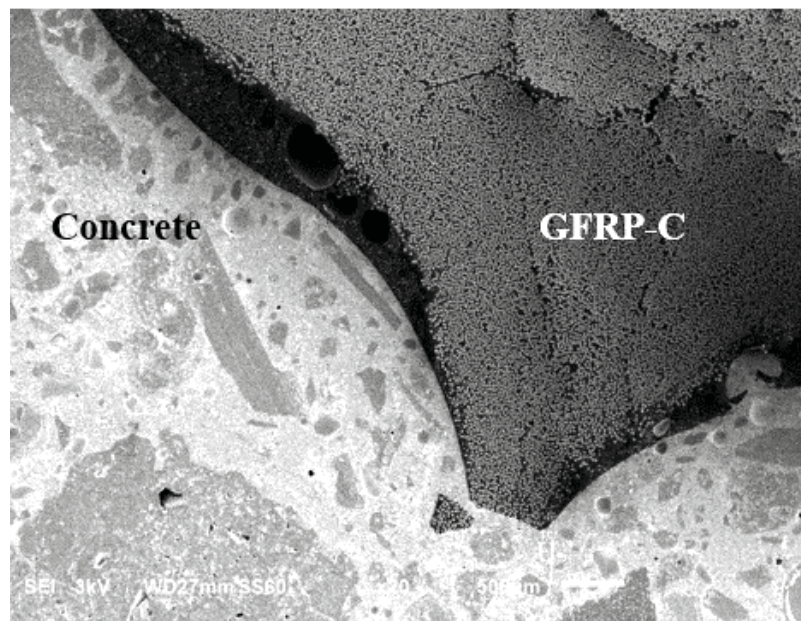


Figure 4.18: SEM image of the concrete to GFRP-C interface after fire exposure at the magnification level of 20x

Thermomechanical FEM Model

Fire tests are expensive and time-consuming to perform [79]. As a result, a numerical modeling approach is helpful in determining the temperature field and investigating the resulting structural behavior. Ultimately, it can provide a rational and holistic approach for the design recommendation [80]. The material properties of concrete and GFRP at different temperature needs to be properly considered in the model.

Concrete Material Properties at Elevated Temperature

Mechanical and thermal properties of the concrete changes with the increase of temperature. The available experimental results are highly scattered since they are dependent on several parameters such as the concrete strength at room temperature, aggregate type, and rate of heating.

The concrete strength reduces with the increase of temperature. The proposed mathematical model in Euro-Code [81] was employed to account for the change of concrete strength due to temperature [82]:

$$\frac{f'_{cT}}{f'_c} = k_c$$

$$k_c = \begin{cases} 1.0 & T \leq 100 \\ (1.067 - 0.00067T) & 100 \leq T \leq 400 \\ (1.44 - 0.0016T) & 400 \leq T \leq 900 \\ 0 & 900 \leq T \end{cases} \quad (4.1)$$

where f'_c is the concrete strength at the ambient temperature and f'_{cT} is the concrete strength at respective temperature T in °C (Figure 4.19).

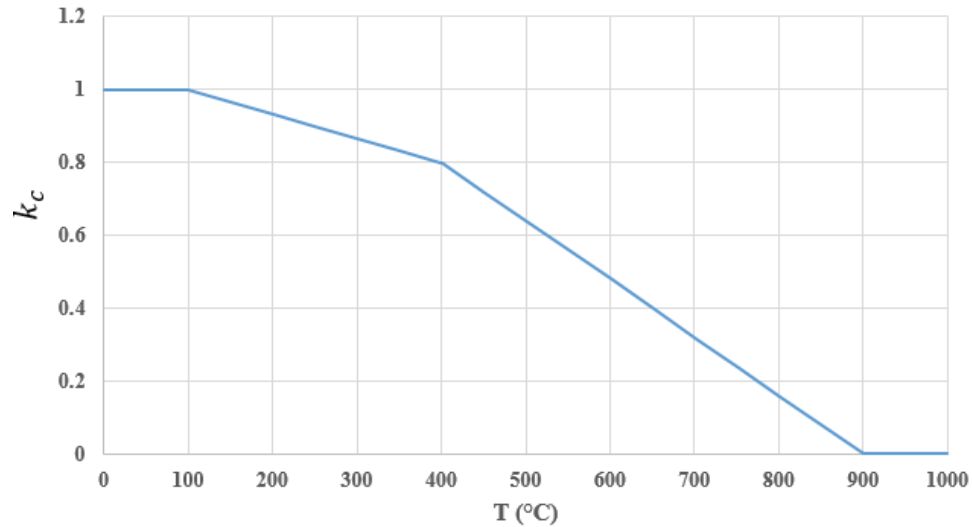


Figure 4.19: Change of the concrete strength with temperature during the fire exposure

Concrete strength stays constant at temperatures below 100 °C and then decreases linearly with the increase of temperature. The rate of reduction increases after 400 °C. When the concrete temperature reaches 900 °C, the strength reduces to zero.

The average 28-day compressive concrete strength was equivalent to 42.3 MPa (6135 psi), determined from testing five concrete cylinders as per ASTM C39 standard.

While the formulation of developing the elastic modulus, tensile strength and stress-strain relationship of concrete based on the concrete strength (chapter 2) was originally derived for ambient temperature, the same formulation was adopted for different temperatures to derive the concrete stress-strain relationships (Figure 4.20 and 4.21). The compression and tension properties were interpolated in Abaqus for other temperatures.

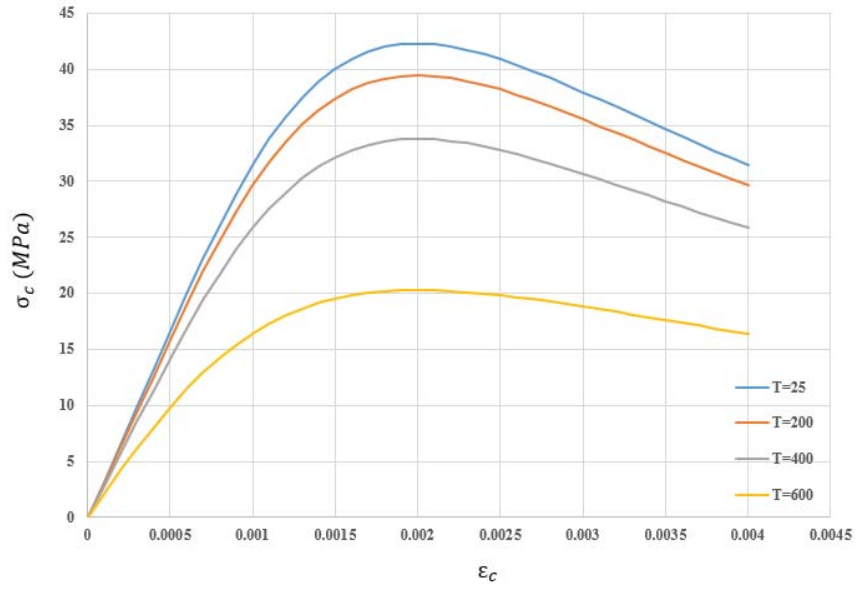


Figure 4.20: Compression behavior of concrete at different temperature of °C

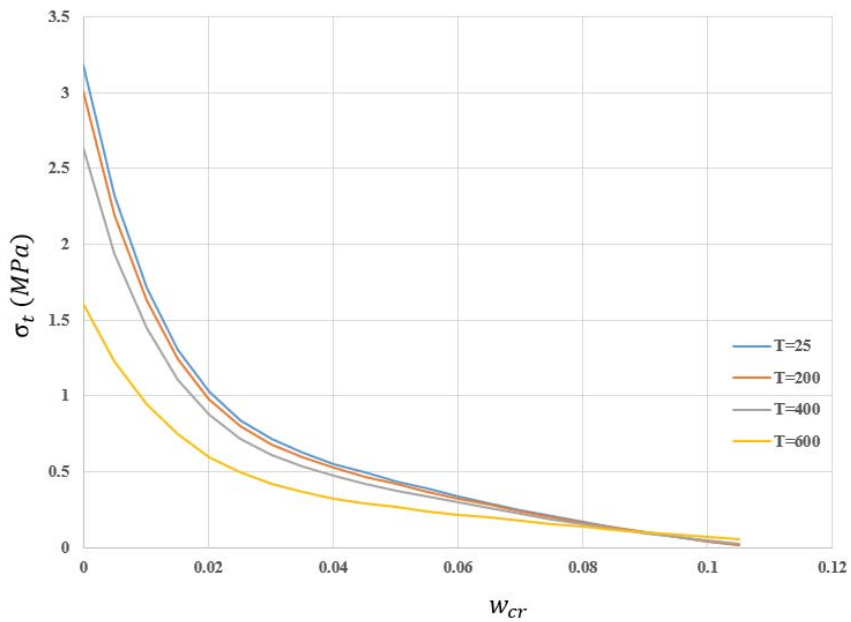


Figure 4.21: Tension behavior of concrete at different temperature of °C

The stiffness (Elastic modulus) and tensile and compressive strength of the concrete decreases by increase of temperature as the result of bond breakage in the microstructure of cement paste and initiation of microcracks.

Usually, an upper and a lower range are provided for the concrete thermal conductivity. In this study, the relationship provided in Euro-code [81] was adopted for the conductivity of the concrete at different temperatures. The use of upper limit is suggested in design procedures to ensure the safety.

The upper and lower range for the conductivity of normal weight concrete, respectively shown as λ_c^u and λ_c^l is determined as: (Figure 4.22)

$$\lambda_c^u = 2 - 0.2451(T/1000) + 0.0107(T/1000)^2 \quad [W/mK] \quad (4.2)$$

$$\lambda_c^l = 1.36 - 0.136(T/1000) + 0.0057(T/1000)^2 \quad [W/mK] \quad (4.3)$$

Where T is the concrete temperature in °C.

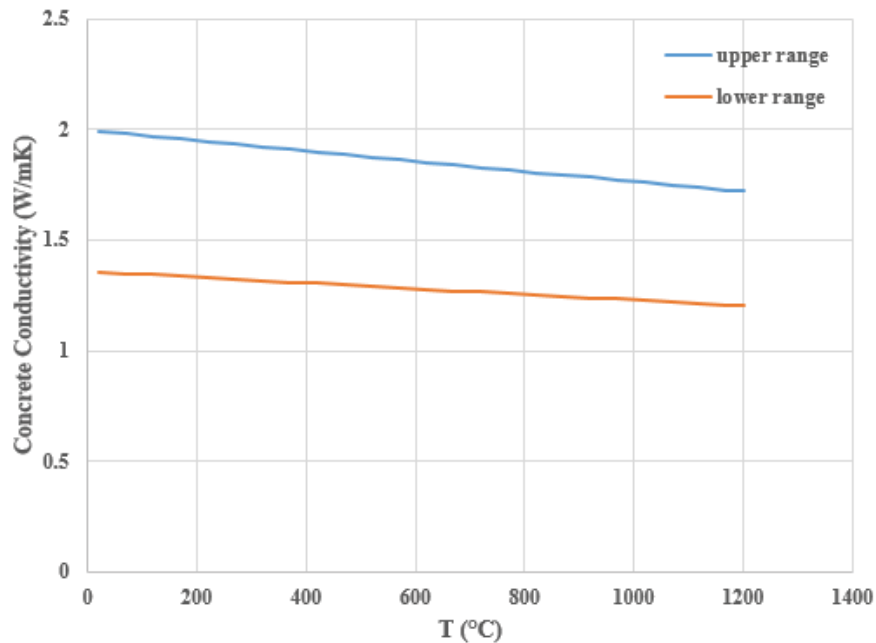


Figure 4.22: Concrete conductivity variation with temperature

The specific heat of the concrete at different temperatures was also implemented using the formulation of Euro-code as (Figure 4.23)

$$C_c = \begin{cases} 900 & 20 \leq T \leq 100 \\ 900 + (\theta_c - 100) & 100 \leq T \leq 200 \\ 1000 + (\theta_c - 200) / 2 & 200 \leq T \leq 400 \\ 1100 & 400 \leq T \leq 1200 \end{cases} \quad (4.4)$$

where T is the concrete temperature in °C.

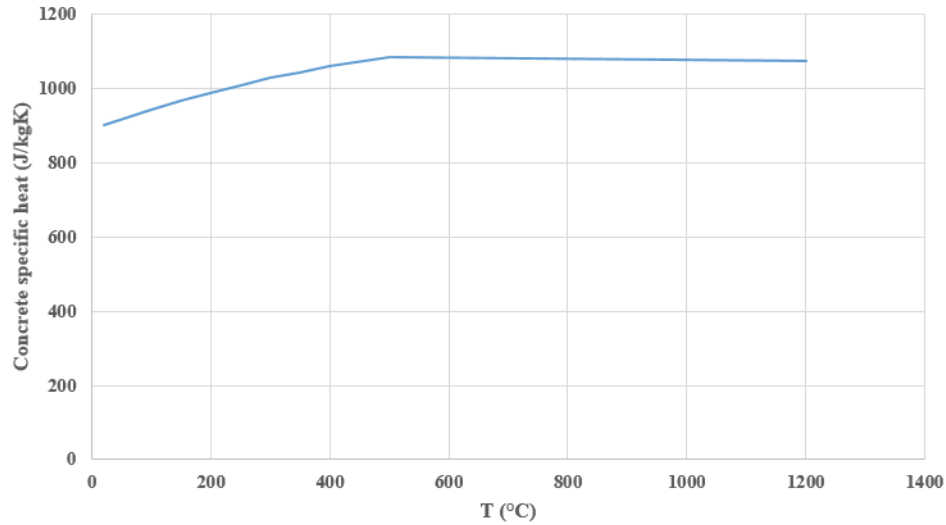


Figure 4.23: Concrete specific heat at different temperatures

The specific heat of the concrete increases with the increase of temperature. The density of concrete was considered to be constant in the current approach.

GFRP Material Properties at Elevated Temperature

The change of GFRP mechanical properties at elevated temperature is not well studied and requires more investigation. Additionally, the available experimental results are available only for specific tested GFRP bars and may not be applicable to the other GFRP reinforcements due to the change in fiber, matrix, fiber/matrix ratio and manufacturing process. [63]. Scholars have studied the change of stiffness and strength of GFRP bars at elevated temperature [63, 83]. In the recent modeling, the mathematical model provided

based on experimental studies of Blontrok and coworkers [72] was adopted in which

$$\frac{f_{GT}}{f_G} = k_f \quad \frac{E_{GT}}{E_G} = K_E.$$

$$K_f = \begin{cases} (1 - 0.0025T) & 0 \leq T < 400 \\ 0 & 400 \leq T \end{cases} \quad (4.5)$$

$$K_E = \begin{cases} 1 & 0 \leq T \leq 100 \\ 1.25 - 0.0025T & 100 \leq T \leq 300 \\ 2.0 - 0.005T & 300 \leq T \leq 400 \\ 0 & 400 \leq T \end{cases} \quad (4.6)$$

where f_{GT} is the GFRP strength at related temperature (T) in °C and f_G is the GFRP strength at room temperature. Similar notations are used for the elastic modulus (E) (Figure 4.24). It is assumed that the entire length of the embedded GFRP bar is affected by the increase of temperature which cause a significant change in both GFRP strength and stiffness. On the other hand, if the temperature of the anchorage portion of GFRP bar does not increase, the bar does not experience a dramatic change of mechanical properties.

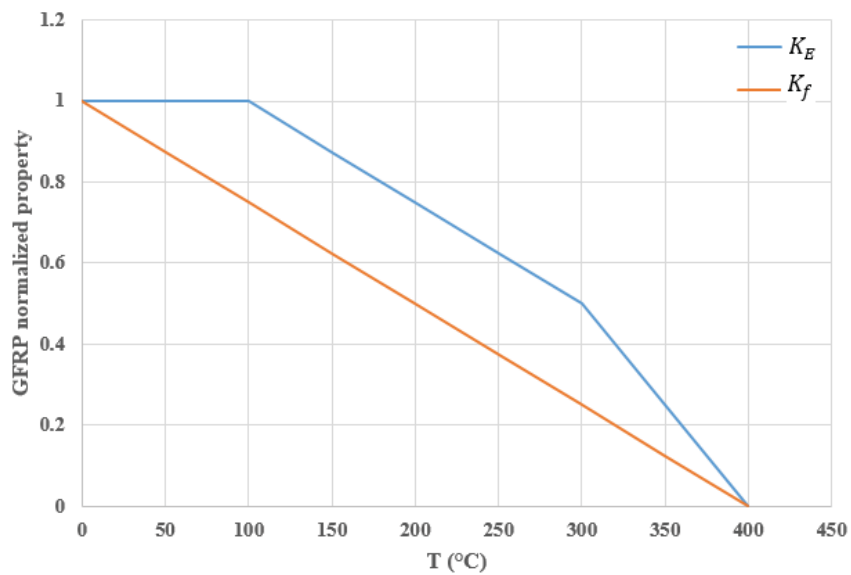


Figure 4.24: GFRP normalized properties at different temperature

The tensile strength of the GFRP bars reduces constantly with increase of the temperature while the modulus of elasticity stays constant before 100 °C and then decreases linearly. The reduction rate of elastic modulus increases after 400 °C.

Thermal conductivity of GFRP at different temperatures provided by Bai and coworkers [84] was implemented by neglecting the difference in the characteristics of the bars in Bai's study (Figure 4.25). The GFRP specific heat was considered constant as $C_G=0.9$ kJ/kgK.

The thermal conductivity was assumed constant before 200 °C and after 400 °C and decreased linearly between these two limits.

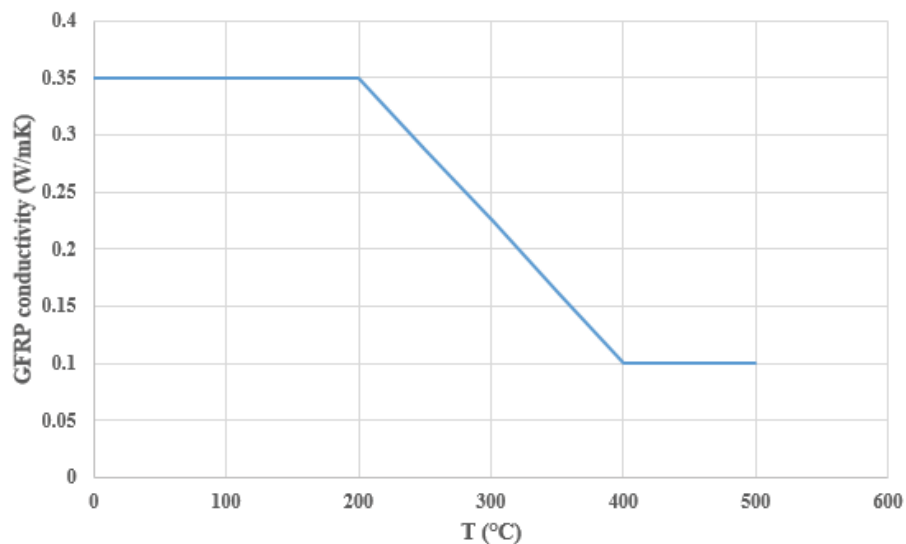


Figure 4.25: Change of GFRP conductivity with temperature

Result of the Thermomechanical Analysis

The coupled thermomechanical analysis was developed in Abaqus for the slab reinforced with GFRP-A bars. A tie constraint was used to apply the temperatures from concrete to the GFRP bars at the shared nodes. The analysis was divided into two parts. First, the mechanical service load (6 kN) was applied at the mid-span in three-point bending configuration (chapter 2) and next keeping the load constant, the thermal load was applied

to the structure. The sides of the slab were assumed adiabatic due to the presence of insulating materials in the gap between the slabs [69]. Due to the uncertainties of the thermal load of the furnace, the temperatures of the exposed and unexposed zones were used as the inputs.

First, only a thermal modeling was performed on the cross-section of the slab to obtain a proper distribution of the temperature. The maximum temperature of 300 °C was applied at the exposed face of the slab. The temperature distribution is provided in Figure 4.26. The temperature changed at different depths of GFRP due to the low thermal conductivity.

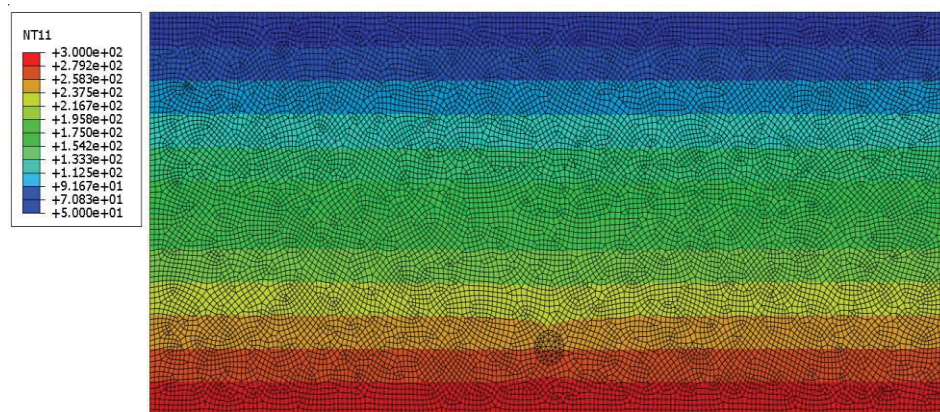


Figure 4.26: Temperature distribution in cross-section of GFRP-RC slab

Next, the coupled thermomechanical analysis was performed by considering the perfect bond between the concrete and GFRP reinforcement. Similar to chapter 2, only half of the slab was modeled due to symmetry condition. First the service load was applied at the mid-span. Next, the load was kept constant and the thermal load was applied. The maximum temperature of 300 °C was applied to the exposed surface. The temperature distribution along the slab is shown in Figure 4.27.

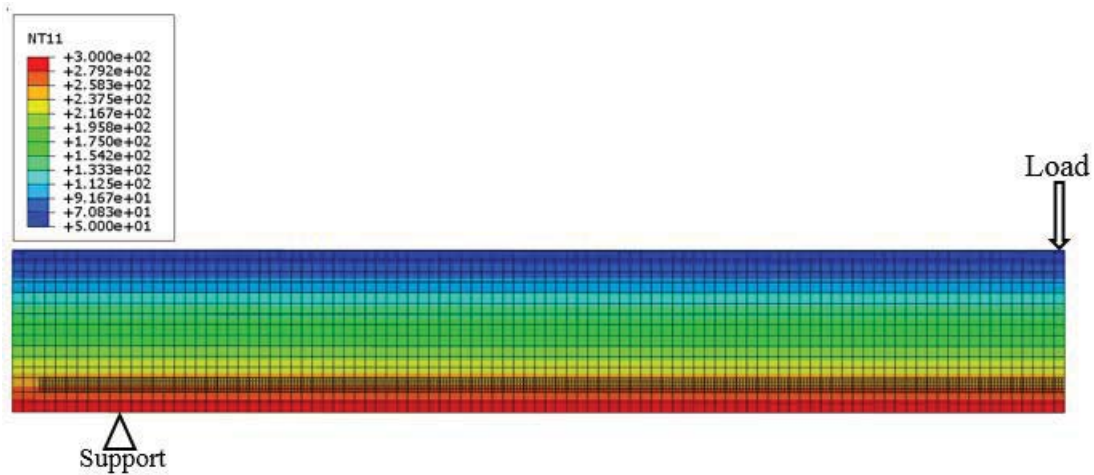


Figure 4.27: Temperature distribution along the fire exposed slab

Since the service load was not high enough to initiate cracking in concrete, the simulation was performed by applying a load of 24 kN at the mid-span to study the effect of fire exposure on cracking and deflection (Figure 4.28).

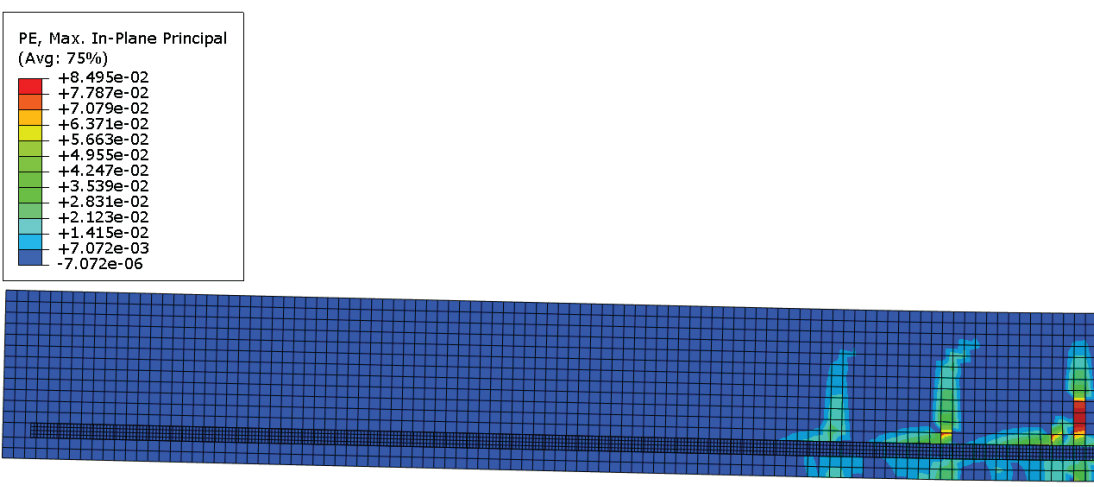


Figure 4.28: Cracking in the GFRP-RC slab due to applied load of 24 kN

The existing cracks propagated and new cracks were generated during the fire exposure. It also resulted to high deflection at the mid-span of the beam (Figure 4.29)

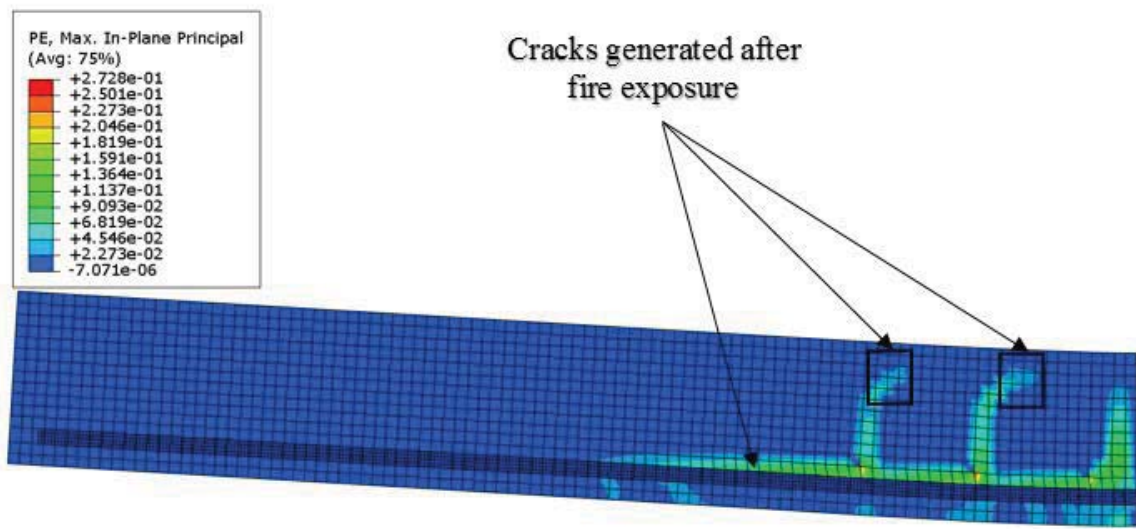


Figure 4.29: Cracks in GFRP-RC slab after the fire exposure

Figure 4.30 shows the load-deflection result of the FEM model at the mid-span of the slab². The structure experienced additional deflection due to fire exposure.

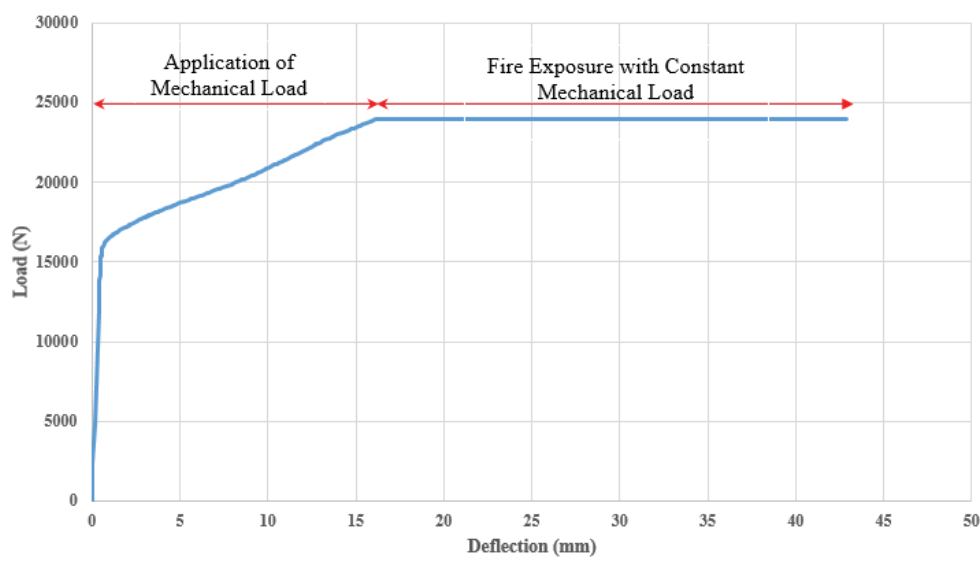


Figure 4.30: Load-deflection result at mid-span of the GFRP-RC slab after fire exposure

² Experimental data will be provided in the future studies to validate the developed FEM model.

Concluding Notes

The residual mechanical properties of GFRP bar segments extracted from the GFRP-RC slabs after 120-minute of standard furnace fire exposure per ASTM E119 was evaluated in this study. Two type of GFRP bars with different surface characteristics were investigated: one sand coated with a helical wrapped fiber; and the other with deformed ribbed surface. Mechanical tests and microstructural investigation were performed to evaluate critical factors governing the residual properties of the GFRP bars including i) transverse shear strength; ii) horizontal shear strength; iii) transition glass temperature, and iv) microstructural investigation using SEM. The results from the two-hour furnace fire exposed specimens were compared to the pristine bars (unexposed to fire). Thermomechanical FEM analysis was developed to provide the temperature distribution and to investigate the effect of fire on the structural response and concrete cracking. Based on the reported results, the following can be concluded:

- For a two-hour fire exposure of GFRP-RC slabs subjected to the design load, a 19 mm (0.75 in.) cover was adequate to provide the necessary fire protection for the reinforcement to avoid irreversible damage.
- The transverse shear strength of the fire exposed GFRP bars reduced but not significantly, and the residual shear strength was higher than the minimum required levels for design purposes.
- Horizontal shear strength and T_g of the fire exposed GFRP bars increased compared to the pristine bars indicating that the resin properties may have improved after the fire exposure.

- Microscopic examination using the SEM imaging did not show any microstructural degradation caused by the furnace fire within the GFRP bars or at the interfacial bond in the GFRP-concrete interface.
- FEM analysis provided the temperature distribution. The temperature varied within the GFRP bars due to low thermal conductivity.
- During the thermal load, additional deflection and propagation of cracks in the concrete was demonstrated using the thermomechanical analysis.

The results presented in this paper provide a general evidence that GFRP-RC elements, could be utilized in the structures with possible fire scenarios.

Future Research

Experimental tests need to be performed to investigate the GFRP bond to concrete at elevated temperatures. Future experimental fire tests and numerical modeling should address the effect of GFRP bond reduction at high temperatures and the anchorage zone (the unexposed zone of the structural member) on structural response during the fire exposure.

Chapter 5-Conclusions

GFRP bars are emerging as an efficient alternative for steel rebars due to the advantages such as corrosion resistance, light weight, high strength to weight ratio and magnetic transparency. Three different aspects of various types of GFRP bars were investigated in this study.

First, the bond properties of GFRP bars were determined through experimental studies and numerical modeling. Three different bars with different surface characteristics were investigated and the effect of this parameter was addressed in detail. In the second study, by employing SEM imaging, it was shown that each GFRP bars demonstrated unique patterns of the cracks/voids in their microstructure. The effect of microstructural patterns in the durability of GFRP bars was demonstrated. The following can be concluded for each study. In the final part of this dissertation, the residual mechanical properties of GFRP bars after exposure to two hours of standard furnace fire were investigated. Additionally, numerical models were developed to predict the temperature distribution in the fire exposed slabs and investigate the effect of the fire on deflection of the structural member and crack propagation in the concrete.

Bond of GFRP Bar to Concrete

Pull-out tests were performed on three different GFRP bars with different surface characteristics to determine the bond strength. The effect of the bar surface characteristic and embedment length on the bond-slip relationship was investigated. The GFRP bar with the highly deformed surface (GFRP-H) failed with sudden concrete splitting. The GFRP bar with the ribbed surface (GFRP-C) demonstrated the separation of the surface enhancement and concrete cracking for samples with the long and short embedment length,

respectively. The sand coated, fiber wrapped (GFRP-A) bars demonstrated the pull-through mode of failure since the cover was large enough to prevent the splitting of concrete. Increasing the embedment length led to reduction of the average bond strength due to generation of more non-uniform stress.

A parametric nodal bond-slip relationship consists of five parameters was proposed for the GFRP-A. A sensitivity analysis was performed on parameters of the bond law. The results of the simulations were compared to the experimental results to provide the parameters. The parametric bond law was employed in a finite element model which captured the concrete cracking and was capable of presenting different failure modes by explicitly modeling the bond action between concrete and reinforcement. The proposed explicit bond model can be applied to any arbitrary GFRP bar with various types of surface characteristics and diameter.

The proposed bond-slip model was implemented in a GFRP-RC slab reinforced with GFRP-A bars. The load-deflection results were compared to the experimental results. Considering the slippage between the reinforcement and concrete led to more realistic and precise predictions of the load-deflection results compared to the case which did not consider any slippage.

GFRP Microstructure

Scanning electron microscopy was performed on four different GFRP bars. Each GFRP bar demonstrated a unique signature of the existing defect/void pattern characterized by a combination of disconnected and continuous voids at different locations of the cross-section due to the different manufacturing process. GFRP microstructural pattern plays a

critical role in the mechanical properties and durability of GFRP bars while it may not be the only effective parameter.

GFRP-B showed the most voids/defects in the cross-section compared to the other GFRP bar types. It mostly included connected voids at the entire area. GFRP-C presented the lowest existing void/defects compared to the other GFRP bar types. There was a single void in the center of the bar and a defect at the edge. The results of this study can be used as a benchmark for microstructure of commercially available pristine GFRP bars and serve as a base for monitoring possible changes after conditioning or field use. GFRP-B and GFRP-C were exposed to accelerated conditioning in a high pH alkaline environment at 60 °C for 1000 hours. GFRP-C did not lose the horizontal shear strength (less than one 1%) while GFRP-B demonstrated 15% loss of this property.

GFRP bars with different microstructural patterns displayed differences in the penetration of the alkaline front. Extensive damage was observed at the vicinity of existing defects and voids.

GFRP Post-Fire Behavior

The residual mechanical properties of GFRP bar segments extracted from the GFRP-RC slabs after 120-minute of standard furnace fire exposure per ASTM E119 was evaluated in this study. Two type of GFRP rebars with different surface characteristics were investigated: one sand coated with a helical wrapped fiber; and the other with deformed ribbed surface. Mechanical tests and microstructural investigation were performed to evaluate critical factors governing the residual properties of the GFRP bars. The results were compared to the pristine bars (unexposed to fire). The results presented in this paper

provide a general evidence that GFRP-RC elements, could be utilized in the structures with possible fire scenarios.

For a two-hour fire exposure of GFRP-RC slabs subjected to the design load, a 19 mm (0.75 in.) cover was adequate to provide the necessary fire protection for the reinforcement to avoid irreversible damage. The transverse shear strength of the fire exposed GFRP bars reduced but not significantly, and the residual shear strength was higher than the minimum required levels for design purposes. Horizontal shear strength and T_g of the fire exposed GFRP bars increased compared to the pristine bars indicating that the resin properties may have improved after the fire exposure. Microscopic examination using the SEM imaging did not show any microstructural degradation within the GFRP bars or at the interfacial bond in the GFRP-concrete interface.

Thermomechanical FEM analysis was developed to provide the temperature distribution and to investigate the effect of fire on the structural response and concrete cracking. During the thermal load, additional deflection and propagation of cracks in the concrete was demonstrated using the thermomechanical analysis.

Bibliography

- [1] Nanni, A., De Luca, A., Jawaheri Zadeh, H., “Reinforced Concrete with FRP Bars: Mechanics and Design”, CRC Press, 2014
- [2] ACI 440.1R, “Guide for the Design and Construction of Structural Concrete Reinforced with FRP bars”, American Concrete Institute, Farmington Hills, MI, 2006
- [3] ACI 440.3R, “Guide Test Methods for Fiber-Reinforced Polymers (FRPs) for Reinforcing or Strengthening Concrete Structures”, American Concrete Institute, Farmington Hills, MI, 2012
- [4] ACI 440.8, “Specification for Carbon and Glass Fiber-Reinforced Polymer (FRP) Materials Made by Wet Layup for External Strengthening of Concrete and Masonry Structures”, American Concrete Institute, Farmington Hills, MI, 2013
- [5] ASTM D7205, “Standard Test Method for Tensile Properties of Fiber Reinforced Polymer Matrix Composite Bars.” ASTM International, West Conshohocken, PA, 2011
- [6] AC 454, “Acceptance Criteria for Fiber-Reinforced Polymers (FRP) Bars for Internal Reinforcement of Concrete Members”, International Code Council-Evaluation Services, 2015
- [7] Achillides, Z., Pilakoutas, K., “Bond Behavior of Fiber Reinforced Polymer Bars under Direct Pullout Conditions.” *Journal of Composite in Construction*, V 8:173-181, 2004
- [8] Aiello, M., Leone, M., Pecce, M., “Bond Performance of FRP Rebars-Reinforced Concrete”, *Journal of Materials in Civil Engineering*, V 19: 205-213, 2007
- [9] Islam, S., Afefy, H., Sennah, K., Azimi, H., “Bond Characteristics of Straight- and Headed-end, Ribbed-surface, GFRP Bars Embedded in High Strength Concrete”, *Journal of Constructions and Building Materials*, V 83: 283-298, 2015
- [10] Hao, Q., Wang, Y., He, Z., Qu, J., “Bond Strength of Glass Fiber Reinforced Polymer Ribbed Rebars in Normal Strength Concrete”, *Journal of Constructions and Building Materials*, V 23: 865-871, 2009
- [11] Chaallal, O., Benmokrane, B., “Pullout and Bond of Glass-Fiber Rods Embedded in Concrete and Cement Grout”, *Materials and Structures*, V 26:167-175, 1993
- [12] Okelo, R., Yuan, R., “Bond Strength of Fiber Reinforced Polymer Rebars in Normal Strength Concrete”, *Journal of Composites in Construction*, V 9: 203-213, 2005

- [13] Vilanova, I., Baena, M., Torres, L., Barris, C., “Experimental Study of Bond-slip of GFRP Bars in Concrete under Sustained Loads”, *Journal of Composite Part B*, V 74: 42-52.
- [14] Baena, M., Torres, L., Turon, A., Barris, C., “Experimental Study of Bond Behavior between Concrete and FRP Bars using a Pull-out Test”, *Journal of Composites: Part B*, V 40: 784-797
- [15] Hu, H., Lin, F., Jan, Y., “Nonlinear Finite Element Analysis of Reinforced Concrete Beams Strengthened by Fiber-Reinforced Plastics”, *Journal of Composite Structures*, V 63: 271-281, 2004
- [16] Nguyen, V., “Numerical Modeling of Reinforced Concrete Bridge Pier under Artificially Generated Earthquake Time-Histories”, Ph.D. Dissertation, the University of Birmingham, 2006
- [17] Birtel, V., Mark, P., “Parameterized Finite Modeling of RC Beam Shear Failure.” ABAQUS Users Conference, 2006
- [18] Pestic, N., Pilakoutas, K., “Tensile Stress-strain Relaxation as a Failure Precursor for FRP strengthened RC beams”, *Journal of Composite Structures*, V 125: 530-541, 2015
- [19] Ooi, E. T., Yang, Z. J., “Modelling Crack Propagation in Reinforced Concrete using a Hybrid Finite Element–scaled Boundary Finite Element Method.” *Engineering Fracture Mechanics*, No.78: 252–273, 2011
- [20] Chen, J.F., Chen, G.M., Teng, J.G., “Role of Bond modeling in Predicting the Behavior of RC Beams Shear-strengthened with FRP U-Jackets”, *Proceedings of the 9th International Symposium on Fiber Reinforced Polymer for Concrete Structures (FRPRCS9)*, 2009
- [21] Tao, Y., Chen, J. F., “Concrete Damage Plasticity Model for Modeling FRP-to-Concrete Bond Behavior.” *Journal of Composite Construction*, V 19: 04014026(1-13), 2015
- [22] den Uijl, A., “A Bond Model for Ribbed Bars Based on Concrete Confinement”, *Stevin Laboratory, Delft University of Technology*, V 41: 201-226, 1996
- [23] Rabczuk, T., Akkermann, J., Eibl, J., “A Numerical Model for Reinforced Concrete Structures” *International Journal of Solids and Structures*, V 42: 1327–1354, 2005
- [24] Ngo, D., Scordelis AC., “Finite Element Analysis of Reinforced Concrete Beams” *Journal of American Concrete Institute*, V 64:154–163, 1967
- [25] Rashid, YR. “Analysis of Prestressed Concrete Pressure Vessels. *Nuclear Engineering and Design*, V 7: 334–44, 1968

- [26] Hillerborg, A., Petersson, “Analysis of Crack Formation and Crack Growth in Concrete by Means of Fracture Mechanics and Finite Elements” *Cement and Concrete Research*, V 6: 773-782, 1976
- [27] Li, Y., Zimmerman, Th., “Numerical Evaluation of the Rotating Crack Model” *Computers and Structures*, V 69: 487-497, 1998
- [28] Pecce M, Manfredi G, Realfonzo R, Cosenza E. “Experimental and Analytical Evaluation of Bond Properties of GFRP Bars” *Journal of Materials in Civil Engineering*, V 13:282–90, 2001
- [29] Cosenza E, Manfredi G, Realfonzo R., “Analytical Modelling of Bond between FRP reinforcing Bars and Concrete”, *Proceedings of second international RILEM symposium (FRPRCS-2)*, London: E and FN Spon; 164–71, 1995
- [30] Claire, G., De Caso y Basalo, F. J. and Nanni, A., “Cross-Sectional Area of GFRP Bars for Concrete Reinforcement.” *ASTM International*, West Conshohocken, PA, 2015 (Under Review)
- [31] ASTM D792, “Standard Test Methods for Density and Specific Gravity (Relative Density) of Plastics by Displacement, Density, Relative Density, Specific Gravity.” *ASTM International*, West Conshohocken, PA, 2013
- [32] Lubliner, J., Oliver, J., Oller, S., and Onate, E., “A Plastic-Damage Model for Concrete.” *International Journal of Solids and Structures*, V 25: 299–326, 1989
- [33] Lee, J., and Fenves, G. L., “Plastic-Damage Model for Cyclic Loading of Concrete Structures”, *Journal of Engineering Mechanics*, V 124: 892–900, 1998
- [34] Saenz, L. P., “Discussion of Equation for the Stress-Strain Curve of Concrete-by Desayi, P. and Krishan, S.” *Journal of American Concrete Institute*, V 61:1229–1235, 1964
- [35] ASTM C39/C39M, “Standard Test Method for Compressive Strength of Cylindrical Concrete Specimens.” *ASTM International*, West Conshohocken, PA, 2014
- [36] ACI 318-14, “Building Code Requirements for Structural Concrete”, *American Concrete Institute*, Farmington Hills, MI, 2014
- [37] Hordijk, D.A., “Local Approach to Fatigue of Concrete”, Ph.D. Dissertation, Delft University of Technology, 1991
- [38] Telford, Th., “CEB-FIB Model Code”, 1990
- [39] Bazant, Z.P., Oh, B.H. “Crack Band Theory for Fracture of Concrete.” *Material of Structure*, V 16: 155–177, 1983
- [40] Bazant, Z.P., Planas, J. “Fracture and Size Effect in Concrete and Other Quasi-brittle Materials.” *CRC Press*, 1998.

- [41] Z.P. Bazant, “Concrete Fracture Models: Testing and Practice.” *Engineering Fracture Mechanics*, V 69: 165-205, 2002
- [42] Rots, J. G., “Computational Modeling of Concrete Fracture”, Ph.D. Dissertation, Delft University of Technology, 1988
- [43] ABAQUS 6.11 User manual, 2011
- [44] Cox, J.V. Herrmann, L.R. “Development of a Plasticity Bond Model for Steel Reinforcement”, *Mechanics of Cohesive-Frictional Materials*. V 3: 155–180, 1998
- [45] Li, C. Q., Yang, S. T., Saafi, M., “Numerical Simulation of Behavior of Reinforced Concrete Structures Considering Corrosion Effects on Bonding”, *Journal of Structural Engineering*, V 140: 04014092 (1-10), 2014
- [46] Tohidi, M., Yang, J., Baniotopoulos, C., “Numerical Evaluations of Codified Design Methods for Progressive Collapse Resistance of Precast Concrete Cross Wall Structures”, *Journal of Engineering Structures*. V 76: 177-186, 2014
- [47] Li, X., “Finite Element Modeling of Skewed Reinforced Concrete Bridges and the Bond-slip Relationship between Concrete and Reinforcement”, Master of Science Dissertation, Auburn University, 2007
- [48] Lundgren, K., Gylltoft, K., “A Model for the Bond between Concrete and Reinforcement”, *Magazine of Concrete Research*, V 52: 53-63, 2000
- [49] Kwak, H., and Hwang, J., “FE Model to Simulate Bond-Slip Behavior in Composite Concrete Beam Bridges.” *Computer in Structures*, V 88: 937–984, 2010
- [50] Maaddawy, T. A., Soudki, K. A., and Topper, T., “Analytical Model to Predict Nonlinear Flexural Behavior of Corroded Reinforced Concrete Beams.” *ACI Structural Journal*, V 102: 550–559, 2005
- [51] Guillermo, C., “Non-Traditional Shape GFRP Rebars for Concrete Reinforcement”, Ph.D. Dissertation, University of Miami, 2015
- [52] Pagani, R., “Valutazione Numerica e Sperimentale della Capacita Portante di Travi in Calcestruzzo Armato con Rinforzi Esterni in Tessuto di Carbonio”, Master of Science thesis, Politecnico di Milano, 2013
- [53] Frosch, R.J., “Another Look at Cracking and Crack Control in Reinforced Concrete”. *ACI Structural Journal*, V 96: 437-442, 1991
- [54] Mukherji, S., Arwika, S. J. “Performance of Glass Fiber-Reinforced Polymer Reinforcing Bars in Tropical Environments-Part II: Microstructural Test”, *ACI Structural Journal*, V 102: 816-822, 2005
- [55] Mufti, A., Banthia, N., Benmokrane, B., Boulfiza, M., Newhook, J. “Durability of GFRP Composite Rods”, *Concrete International*, V 29: 37-42, 2007

- [56] Micelli, F., Nanni, A. “Durability of FRP Rods for Concrete Structures”, *Journal of Construction and Building Materials*, V 18: 491-503, 2004
- [57] ASTM D4475, “Apparent Horizontal Shear Strength of Pultruded Reinforced Plastic Rods by the Short-Beam Method”, ASTM International West Conshohocken, PA, 2008
- [58] Buchanan, A. H., “Structural Design for Fire Safety”, John Wiley and Sons, Chichester, UK, 2002.
- [59] Kodur, V., “Properties of Concrete at Elevated Temperature”, Hindawi Publishing Corporation, Article ID 468510, 2014
- [60] Gewain, R., Iwankiw, N., Alfawakhiri, F., “Facts for Steel Buildings: Fire”, American Institute of Steel Construction, 2003
- [61] ASTM E119, “Standard Test Methods for Fire Tests of Building Construction and Materials.” ASTM International, West Conshohocken, PA, 2014
- [62] ASTM E1529-14a, “Standard Test Methods for Determining Effects of Large Hydrocarbon Pool Fires on Structural Members and Assemblies”, ASTM International, West Conshohocken, PA, 2014
- [63] Weber, A., “Fire-Resistance Tests on Composite Rebars.” In: *Proceedings of CICE2008*, Zurich, Switzerland, 2008
- [64] Bisby, L., Green, M., Kodur, V., “Response to Fire of Concrete Structures that Incorporate FRP”, *Structural Engineering in Materials*, V 7: 136-149, 2005
- [65] Nigro E., Cefarelli G., Bilotta A., Manfredi G. and Cosenza E., “Fire Resistance of Concrete Slabs Reinforced with FRP Bars. Part I: Experimental Investigations on the Mechanical Behavior” *Journal of Composites: Part B*, V 42: 1739-1750, 2011
- [66] Abbasi, A., Hogg, P., “Prediction of the Failure Time of Glass Fiber Reinforced Plastic Reinforced Concrete Beams under Fire Conditions”, *Journal of Composites for Construction*, V 9: 450-457, 2005
- [67] CSA S806-12, “Design and Construction of Building Structures with Fiber Reinforced Polymers”, 2012
- [68] Kodur, V.K.R., Baingo, D., “Fire Resistance of FRP-Reinforced Concrete Slabs.” Internal Report Institute for Research in Construction, National Research Council Canada; No. 178, 1998

- [69] Bisby, L.A., Kodur, V.K.R., “Evaluating the Fire Endurance of Concrete Slabs Reinforced with FRP Bars: Considerations for a holistic approach” *Composite: Part B*, V 38: 547-558, 2007
- [70] Nigro E., Cefarelli G., Bilotta A., Manfredi G. and Cosenza E., “Fire Resistance of Concrete Slabs Reinforced with FRP Bars. Part II: Experimental Results and Numerical Simulations on the Thermal Field.” *Journal of Composites: Part B*, V 42: 1751-1763, 2011
- [71] McIntyre, E., Bisby, L., Stafford, T., “Bond Strength of FRP Reinforcement in Concrete at Elevated Temperature”, *The 7th International Conference on FRP Composite in Civil Engineering, CICE, Vancouver, Canada, 2014*
- [72] H. Blontrock, L. Taerwe, and S. Matthys, “Properties of Fiber Reinforced Plastics at Elevated Temperatures with Regard to Fire Resistance of Reinforced Concrete Members”, *International Concrete Institute*, V 188: 43-45, 1999
- [73] Kodur, V.K.R, Agrawal, A., “Critical Factors Governing the Residual Response of Reinforced Concrete Beams Exposed to Fire”, *Fire Technologies*, V 52: 967-993, 2015
- [74] Abbasi, A., Hogg, P.J, “Fire Testing of Concrete Beams with Fiber Reinforced Plastic Rebar.” *Composites Part A*; V 37:1142–50, 2006
- [75] Cheng, F., Kodur, V., Wang, T., “Stress-Strain Curves for High Strength Concrete at Elevated Temperatures”, *Journal of Materials in Civil Engineering*, V 16: 84-90, 2004
- [76] Claire, G., De Caso y Basalo, F. J. and Nanni, A., 2015. “Post-Fire Residual Strength of GFRP Reinforced Concrete Slabs.” *Proceedings of the 7th Biennial Conference on Advanced Composites in Construction, ACIC 2015, Cambridge, UK, September 9-11, 2015*, 96-104.
- [77] ASTM D7617/D7617M, “Standard Test Method for Transverse Shear Strength of Fiber-reinforced Polymer Matrix Composite Bars.”, *ASTM International, West Conshohocken, PA, 2011*
- [78] ASTM E1640, “Standard Test Method for Assignment of the Glass Transition Temperature by Dynamic Mechanical Analysis”, *ASTM International, West Conshohocken, PA, 2013*
- [79] Palm, J., “Temperature Analysis Using Abaqus”, *Fire Technology*, V 30: 291-303, 1994

- [80] Chowdhury, E., Green, E., Bisby, L., Benichou, N., Kodur, V., “Thermal and Mechanical Characterization of Fiber Reinforced Polymers, Concrete, Steel, and Insulation Materials for Use in Numerical Fire Endurance Modeling”, National Research Council of Canada, NRCC-49684, 2007
- [81] Euro-code 2: Design of concrete structures, ENV EC2, 1992
- [82] Nadjai, A., Talamona, D., Ali, F., “Fire Performance of Concrete Beams Reinforced with FRP Bars”, Proceeding of the International Symposium of Bond Behavior of FRP in Structures, 2005
- [83] Wang, Y.C., Kodur, V., “Variation of Strength and Stiffness of Fiber Reinforced Polymer Reinforcing Bars with Temperature”, Cement & Concrete Composites, V 27: 864-874, 2005
- [84] Bai, Y., Vallee, T., Keller, T., “Modeling of Thermal Responses for FRP Composites under Elevated and High Temperatures”, Composite Science and Technology, V 68: 47-56, 2008